Advancements in Optical Readout Technologies

Test Mass Sensing and Laser-Frequency Stabilization Techniques for Optical Compact Interferometry

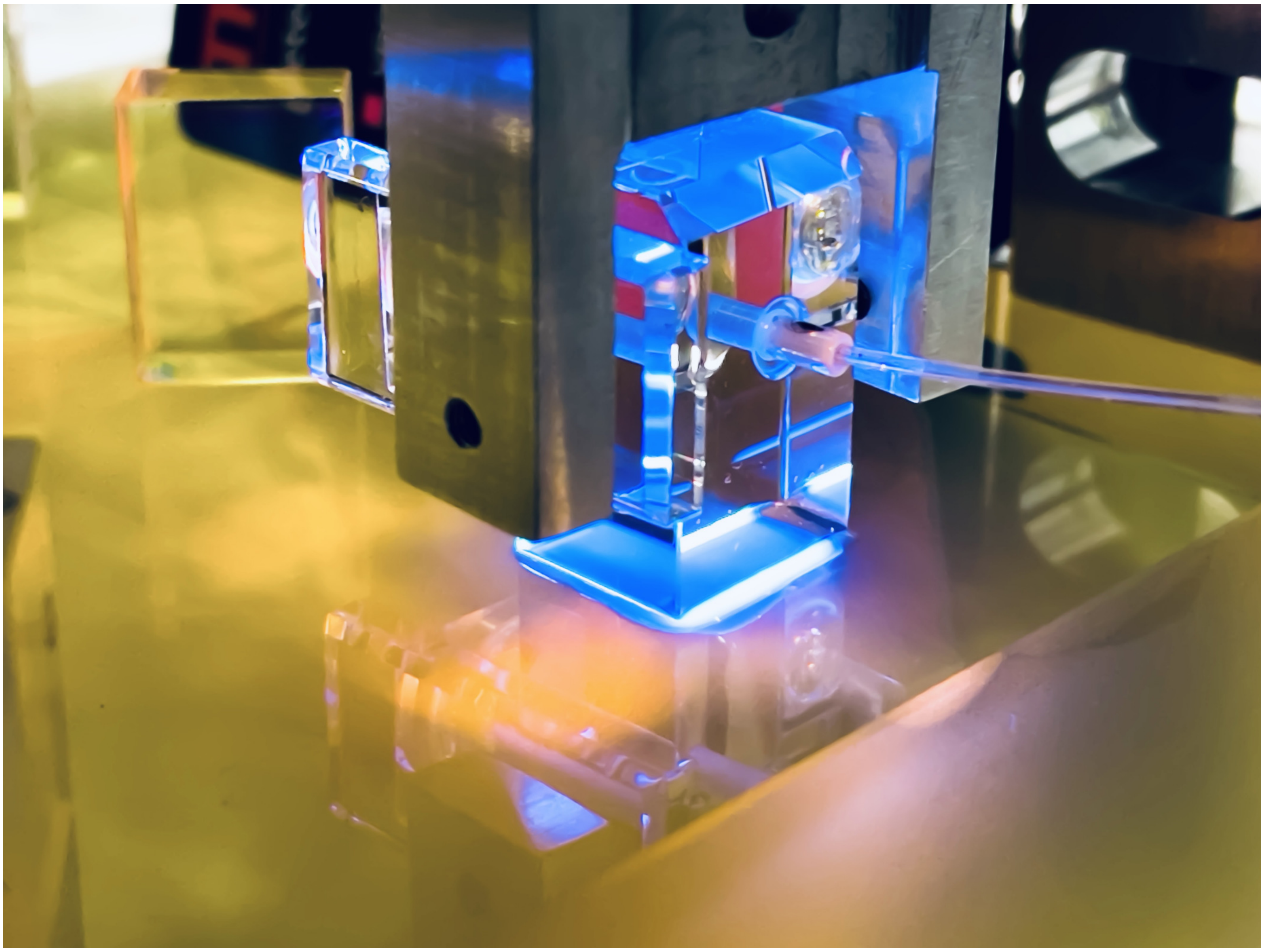

Victor Javier Huarcaya Azañon, M.Sc.
2023

Leibniz Universität Hannover

Albert Einstein Institute
Max-Planck-Institut für Gravitationsphysik und
Leibniz Universität Hannover

MAX-PLANCK-GESELLSCHAFT

Advancements in Optical Readout Technologies

Test Mass Sensing and Laser-Frequency Stabilization Techniques for Optical Compact Interferometry

Von der Fakultät für Mathematik und Physik
der Gottfried Wilhelm Leibniz Universität Hannover
zur Erlangung des akademischen Grades

Doktor der Naturwissenschaften
Dr. rer. nat.

genehmigte Dissertation von

Victor Javier Huarcaya Azañon, M.Sc.

2024

Referent: Apl. Prof. Dr. Gerhard Heinzel
Korreferent: Prof. Dr. Karsten Danzmann
Korreferent: Junior Dr. rer. nat. Katharina-Sophie Isleif
Tag der Promotion: December 1st, 2023

Esta Tesis está dedicada a la memoria de mi padre,
Victor Severino Huarcaya Cardenas (1946-2022)

y a la de mi tía abuela,
Francisca de Dios Forteza, (1927-2023)

Contents

Acknowledgements

The road to get the Ph.D. has been long... really long. Cavafy wrote in his poem *Ithaka*, *"As you set out for Ithaka, hope your road is a long one..."*. I couldn't be more grateful to be surrounded by the best in the long road.

Thank you, Professor Danzmann, for the amazing institute you have led. I hope to keep your science enthusiasm and motivation in my personal and professional career all my life.

Gerhard, I'm deeply grateful for your leadership in the Space Interferometry group and the incredible work environment you've fostered. Your openness in accepting me into the team years ago when I reached out for a Ph.D. position has been pivotal in my journey. Throughout my academic career, I've been in various places, but I must say, I've never encountered a supervisor quite like you. Your approach, granting me substantial freedom to steer my research, has been instrumental, and my achievements in research are largely due to the support and guidance from you.

Thank you, Prof. Dr. Rasel, for the chairmanship, and thank you, Univ. Prof. Dr. rer. nat. Katharina-Sophie Isleif, aka "Katha", for not only accepting to be part of the examiner committee but also for helping me at a distance all these years when I had doubts regarding DFM or the lab equipment. My work is based on her previous work, where she put the quality bar at high standards. I hope my work is worthy of her.

To Moritz Mehmet, thanks. Thanks for helping me in the lab all these years. Your willingness to always have your door open, whether I had questions or just needed to talk, has meant a lot to me. Your help has been essential for me to obtain this doctorate, and as I wrote you, thanks for even being picky with me because it has been a significant learning experience, and I've gained so much from your guidance.

Thanks to Prof. Dr. Jaume Carot, chancellor of the University of the Balearic Islands, for being not only the best teacher I had during my undergrads but also for his friendship during all these years.

Thanks to Vitus Händchen and Gerald Bergmann for showing me how to work and behave in the lab and to Stefano Gozzo for proofreading some parts of this thesis.

Thanks to all my colleagues here at the Space Interferometry group who helped me not only in the lab but also with the paperwork, lab issues, and even the coffee time: Oli, Jens, Stefan and Melanie, Michael, Yongho, Alvise, Alicia, Sergio, Christoph, Gudrun, Iouri, Henry, Kohei, Jonathan, Malte, Marie, Vitali, Rodrigo, Lea, Daniel and Martin.

To Dr. Alexander Wanner and the Leibniz Universität Hannover for funding my travel to Wuhan, China. There, I had a great time and thanks to the great people I met: Dr. Prof. Ze-Bing Zhou, Dr. Yanzheng Bai, Prof. Mei Jianwei, Dr. Yan Hao, and the rest of the wonderful people in the Huazhong University of Science and Technology and from the MOE Key Laboratory of Fundamental Physical Quantities Measurements.

To the rest of my colleagues at the Albert Einstein Institute: Thanks to Kirsten Labove for helping me with all the bureaucratic stuff many times and for her friendship. Thanks to the IT team for solving all the issues I have had during my Ph.D., to Andreas and Phillip from the Electrical Workshop for helping me with all the damm electronics, Udo, and Phillip and Jan from the Mechanical Workshop for providing me with all the mechanical parts I needed over all these years. Also, thanks to Birgit Ohlendorf for helping me with great professionalism in all the Ph.D. bureaucratic matters.

To the Vynil Club team: Rahul, Jasper, Tom, Xisco, Pep, Gema Simo, Celia, Tere, Miguel... Thanks for providing some ”sanity” with the Vinyl Club parties during the Pandemic years.

A German Fernandez Barranco y Miriam Cabero Müller: No tengo palabras para expresar mi gratitud por contestar ese mail que recibisteis de un desconocido cuando os pregunto acerca del doctorado en el AEI. Sin vosotros no hubiera empezado esta tesis... es más, gracias a ese pequeño gesto, habéis cambiado mi vida.

A Pablo Martinez Cano, gracias por estar ahi cuando te necesito, sea para el café o para los diseños CAD que siempre te pido que me hagas, y a Jordina, por poner

siempre una sonrisa en el pasillo. A Tom Gajecki, que tanto en lo bueno, como en lo malo, he conocido a un amigo para toda la vida.

A Francisco Jimenez Forteza, gracias por ser un buen amigo. Espero que la amistad perdure incluso en rocas perdidas del Mediterráneo y que nos podamos ver ahí (o en otros sitios)...

A J.J. Esteban and Miguel Dovale. Qué puedo decir, chicos? Vosotros habéis sido mi pilar en el doctorado. Si he conseguido excelentes resultados en mi trabajo ha sido porque me he subido sobre vuestros hombros. Gracias por ser unos compañeros excepcionales y amigos invaluables. Sin vosotros, no hubiera llegado a donde estoy ahora mismo.

Por último, quiero agradecer por todo a mi familia, en especial a mi padre, que ojalá hubiera estado aquí para verme y a mi madre, Amparo Azañon de Dios. Ambos me han enseñado el significado de la palabra paciencia y perseverar. Sin esto, no hubiera llegado a donde estoy. A mis hermanos, Christian y Alberto por ser los mejores hermanos que uno pueda tener. Por último, a mis suegros, Tatiana y Alexander, por darme el mejor regalo que un hombre puede tener... Parafraseando a Carl Sagan, *En la vastedad del espacio y la inmensidad del tiempo, es para mí una alegría compartir un planeta y una época con mi esposa*, Yulia Morhunova Zhmak.

List of Figures

List of Tables

Abstract

Precision measurement of freely floating test masses across multiple degrees of freedom is a critical requirement for gravitational space missions or gravitational table-top experiments. Traditional methods like capacitive sensing or laser interferometry have demonstrated certain limitations in terms of precision and sensing in several degrees of freedom, respectively. This thesis presents recent advancements aimed at addressing these limitations. Optical levers, combined with a modulation/demodulation technique, have been developed to achieve an angular resolution of below 400 nrad $\mathrm{Hz}^{-1/2}$ at frequencies between 10 mHz and 1 Hz (which is better than a conventional autocollimator in 1.5 orders of magnitude) across five degrees of freedom, offering a potential alternative to the constraints of capacitive sensing. This method's capability to potentially sense all six degrees of freedom suggests it could be a viable alternative to more complex laser interferometric setups. Simultaneously, the development of new interferometric topologies like the self-referenced single-element dual-interferometer (SEDI) has been explored. Utilizing sinusoidal phase modulation homodyne interferometry, this approach reduces the complexity of the optical setup while maintaining sub-picometer precision in a compact design using a custom-designed prism. Such a design is advantageous for applications with stringent size and weight requirements. Laser frequency stabilization, essential for low-frequency noise in ultra low frequencies, has been addressed through two distinct techniques. The first employs an unequal-arm Mach-Zehnder interferometer, achieving a fractional instability below 4×10^{-13} at averaging times from 0.1 to 100 seconds. The second method uses the SEDI prism in a compact setup to stabilize the laser frequency, achieving a fractional frequency instability below 4×10^{-12} at averaging times from 0.1 to 1000 seconds. In summary, these advancements provide enhanced precision and reduced complexity for future gravity missions, also offering improved tools and methodologies for future research endeavors.

Keywords: Optical Readout, Frequency Stabilization, Compact Interferometry

Kurzfassung

Die präzise Messung von frei schwebenden Testmassen über mehrere Freiheitsgrade ist eine entscheidende Voraussetzung für Weltraummissionen oder Labor-Experimente zur Erforschung der Gravitation. Herkömmliche Methoden wie die kapazitive Messung oder die Laserinterferometrie haben gewisse Einschränkungen in Bezug auf Präzision und Freiheitsgrade gezeigt. In dieser Arbeit werden die jüngsten Fortschritte vorgestellt, die darauf abzielen, diese Einschränkungen zu überwinden. Optische Hebel, kombiniert mit einer Modulations-/Demodulationstechnik, wurden entwickelt, um eine Winkelauflösung von unter 400 nrad $\mathrm{Hz}^{-1/2}$ bei Frequenzen zwischen 10 mHz und 1 Hz (der um 1.5 Größenordnungen besser ist als ein herkömmlicher Autokollimator) über fünf Freiheitsgrade zu erreichen, was eine potenzielle Alternative zu den Beschränkungen der kapazitiven Abtastung darstellt. Die Möglichkeit, potenziell alle sechs Freiheitsgrade zu erfassen, deutet darauf hin, dass diese Methode eine brauchbare Alternative zu komplexeren laserinterferometrischen Anordnungen sein könnte. Gleichzeitig wurde die Entwicklung neuer interferometrischer Topologien wie des selbstreferenzierten Einzelelement Doppelinterferometers (SEDI) erforscht. Durch die Verwendung von Homodyner Interferometrie und Phasenmodulation reduziert dieser Ansatz die Komplexität des optischen Aufbaus bei gleichbleibender Sub-Pikometer-Präzision in einem kompakten Design unter Verwendung eines speziell entwickelten Prismas. Ein solches Design ist vorteilhaft für Anwendungen mit strengen Anforderungen an Größe und Gewicht. Die Frequenzstabilisierung des Lasers, die für das Rauschen bei niedrigen Frequenzen unerlässlich ist, wurde mit zwei verschiedenen Techniken angegangen. Bei der ersten wird ein Mach-Zehnder-Interferometer mit ungleichen Armen verwendet, das bei Mittelungszeiten von 0.1 bis 100 Sekunden eine fraktionierte Instabilität unter 4×10^{-13} erreicht. Bei der zweiten Methode wird das SEDI-Prisma in einem kompakten Aufbau zur Stabilisierung der Laserfrequenz verwendet, wobei eine fraktionierte Frequenzinstabilität besser das bei Mittelungszeiten von 0.1 bis 1000 Sekunden eine fraktionierte Instabilität unter 4×10^{-12} erreicht. Zusammenfassend lässt sich sagen, dass diese Fortschritte eine höhere Präzision und eine geringere Komplexität für künftige Schwerkraftmissionen bieten, sowie verbesserte Werkzeuge und Methoden für künftige Missionen mit Laserinterferometern.

Keywords: Optische Auslesung, Laserfrequenzstabilisierung, Kompaktinterferometrie

Part I

Introduction

Chapter 1

Overview

This thesis is divided into three parts, which are the basis of my entire doctorate:

- Part I: Introduction
- Part II: Optical Test Mass Readout
- Part III: Compact Interferometers

Chapter 2 is the introduction, which includes an overview of gravitational space missions that motivate the thesis's outline.

Part II covers Chapter 3, which is an extension of the paper *"Five degrees of freedom test mass readout via optical levers"*, published in December 2019, where it reports on the realization of a test mass sensing system using a modulation/demodulation technique in combination with four optical levers detected by quadrant photodiodes.

Part III covers the compact interferometry part. Chapter 4 briefly summarizes laser interferometry for space applications, introducing the technique "Deep Frequency Modulation" or DFM. Chapter 5 is an extension of the paper "2×10^{-13} *fractional laser frequency stability with a 7 cm unequal-arm Mach-Zehnder interferometer"*, published in August 2023, which reports on a compact laser-frequency stabilization technique based on an unequal-arm Mach-Zehnder interferometer (MZI), including a detailed description of an experimental setup for future DFM experiments. Chapter 6 is a short summary of the paper *"Single-Element Dual-Interferometer for Precision Inertial Sensing"* (SEDI sensor), published in September 2020, which introduces the design and construction of a novel sensor topology, including the preliminary results using DFM and the same laser-frequency stabilization technique described in Chapter 5. Also included are the first results of the laser-frequency stabilization using the SEDI given by the paper *"Single-Element Dual-Interferometer for Precision Inertial Sensing: Sub-Picometer Structural Stability and Performance as a Reference for Laser Frequency Stabilization"*, published in December 2023.

Part IV includes the remaining chapters of this thesis. Chapter 7 describes the future work involving the optical lever, MZI, and SEDI, while Chapter 8 provides a summary of the thesis. Lastly, appendices A.1 and B.2 contain the **Tcl** code for the Hexapod motion described in section 3.2, whereas appendices C.3 and D.4 contain the Matlab code for the test mass sensing system described in Chapter 3 and pictures of the SEDI prism, respectively.

Chapter 2

Gravitational Space Missions

2.1 Introduction

Four fundamental interactions are known to exist: gravity, electromagnetism, weak and strong interaction. Although gravity is one humanity has known of for thousands of years, it is perhaps the least fully understood (at least at the quantum level) of the forces today. Gravity force has an infinite range: planets orbiting around the sun, star systems orbiting the galaxy, and intergalactic dynamics point to the fact that at cosmological scales, it is the dominant interaction. Despite its far-reaching effects, gravity is the weakest of the four fundamental forces by many orders of magnitude. For instance, the electromagnetic force between two electrons is about 10^{36} times stronger than the gravitational force between them. This weakness makes studying gravity in a laboratory extremely difficult [1]. For example, the gravitational constant, denoted by G in Newton's law of universal gravitation, is known to have a lesser degree of precision than other fundamental constants. Its exact value, which currently is $G = 6.674184 \times 10^{11}\ \mathrm{m^3 kg^{-1} s^{-2}}$ is challenging to measure with high precision, leading to uncertainties in our understanding of gravity [2].

Still, despite its ubiquitous presence and observable effects, gravity's inherent nature and precise workings have yet to be entirely understood for several reasons. For example, one of the most challenging puzzles in theoretical physics is harmonizing general relativity, which describes gravity, with quantum mechanics, explaining the other three fundamental forces. Quantum mechanics deals with the universe at the tiniest scales, while general relativity deals with the universe at the larger ones. Currently, there is no entirely accepted quantum theory of gravity [3], which would be necessary to understand gravity at the smallest scales, such as near a black hole's singularity [4]. Another problem involving observations of galaxy rotation curves, gravitational lensing, and the universe's large-scale structure suggests that a significant amount of undetected matter, known as dark matter, influences gravitational dynamics. Additionally, the observed accelerated expansion of the universe implies the existence of a mysterious dark energy that counteracts gravity. These two phenomena account for about 95% of the universe's total mass-energy content, yet still it is needed a clear understanding of their nature [5].

Despite these challenges, work is continually being done in the laboratories to understand more about gravity. For example, torsion balances are being used to measure with less uncertainty the value of G [6] or to test future gravitational sensors [7]; on the ground, building giant interferometers like Virgo, GEO600, KAGRA (Kamioka Gravitational Wave Detector), or LIGO (Laser Interferometry Gravitational-waves Observatory) [8], who announced the first direct observation of gravitational waves detected on 14 September 2015 [9]; or even in space, with missions like GOCE (Gravity Field and steady-state Ocean Circulation Explorer, 2009–2013), GRACE (Gravity Recovery and Climate Experiment, 2002–2017), its follow-on mission GRACE-FO, and the future gravitational wave space detector LISA (Laser Interferometer Space Antenna) and its technology demonstrator LISA pathfinder. As a result, gravity research can significantly advance knowledge of fundamental physics.

2.2 Space Missions

Gravitational space missions are a cornerstone of our quest to comprehend the universe and our home planet: The Earth. Also, it offers significant benefits, like advancing our understanding of the universe, aiding in developing new technologies and contributing to climate studies. Unlike ground-based experiments, where the primary noise source in the interferometric detectors at low frequency is gravity gradient noise (caused primarily by variations in the density of the Earth and movement of masses on or near the Earth's surface), experiments conducted under free fall conditions improve the sensitivity and accuracy of the measurement devices. Effectively simulating a state of weightlessness, several notable advantages are associated when conducting experiments under such conditions:

- Enhanced sensitivity: in a microgravity environment, the sensitivity of numerous measuring devices is amplified due to the elimination of gravitational interference. This increased sensitivity can enable the detection and measurement of phenomena that would be indiscernible under the influence of Earth's gravity (i.e., protein crystallization [10]). Also, gravitational forces often introduce systematic errors into measurements, effectively eliminated in a state of weightlessness, thus enhancing the accuracy of the data collected (i.e., gravitational waves in space).

- Access to novel phenomena: free fall conditions can expose and make accessible certain physical phenomena that are masked or dominated by gravity in standard conditions. This can be particularly useful in fundamental physics research, where investigating phenomena unaffected by gravity can lead to insights into the fundamental laws of nature (i.e., how Bose-Einstein condensates behave in microgravity [11]).
- Reduced mechanical stress: in a state of weightlessness, the mechanical stress on structures and materials is reduced, which can benefit specific experiments, particularly in material sciences (i.e., solidification of metal alloys in microgravity [12]).
- Improved fluid behavior: in microgravity conditions, the behavior of fluids is governed primarily by surface tension and capillary effects, allowing for the study of fluid dynamics without the complicating factor of gravity (i.e., effects of gravity in droplets [13]).

More advantages and disadvantages can be found in [14]. However, the venture into space is not merely an ambition for exploration but a crucial step towards achieving superior accuracy and precision in experimental measurements than those conducted on terrestrial platforms. Space-based experiments offer a unique environment that mitigates the challenges associated with terrestrial constraints, thereby allowing for advancements in accuracy that are unattainable within the limitations of ground-based experiments.

This thesis briefly describes the most representative gravitational space missions where the Max Planck Institute for Gravitational Physics (Albert Einstein Institute - AEI) has participated in their development. Although the AEI was not involved in the GOCE mission, it is also mentioned since it will help to understand further sections of this thesis. Also, the description of the following missions is not intended to be very detailed/thorough but instead serves as a summary of the respective missions' characteristics. Each section will include references to provide the reader with a deeper understanding of these missions.

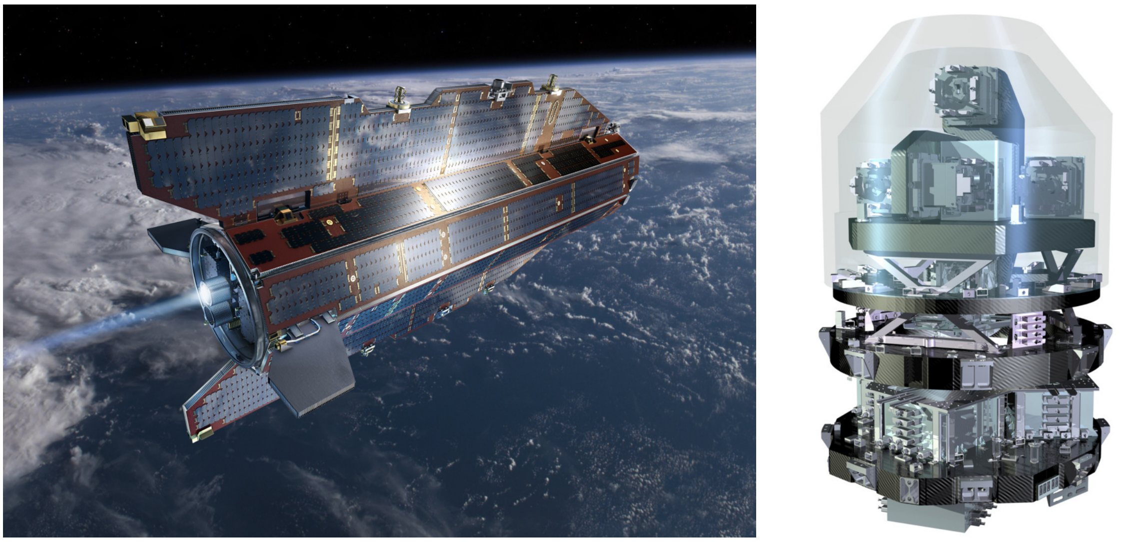

(a) GOCE spacecraft

(b) Electrostatic Gravity Gradiometer

Figure 2.1: (a) Featuring a streamlined, aerodynamic structure that has earned the nickname *'Ferrari of space'*, GOCE has mapped variations in Earth's gravity with extreme detail. (b) GOCE gradiometer comprises three sets of identical, highly sensitive accelerometers, each set positioned on three mutually perpendicular "arms" (as depicted in the upper section of the image). The system also includes additional components related to the control and read-out electronics of the gradiometer, the structure, and the thermal control elements. The three arms are arranged orthogonally: one aligns with the satellite's path, another points towards Earth's center, and the third stands at right angles to the other two. Credits: ESA/AOES Medialab

2.2.1 GOCE

Launched in March 2009, ESA's (European Space Agency) Gravity field and steady-state Ocean Circulation Explorer (GOCE) mission (spacecraft artist's view shown in Fig.2.1a) was the first Earth Explorer mission in orbit [15]. The mission ended in November 2013 when the satellite re-entered the Earth's atmosphere. GOCE was the first of ESA's Living Planet Programme [16] satellites intended to map the Earth's gravity field in great detail. The mission aimed to improve our knowledge and understanding of the Earth's interior and climate change. The data from the mission has been used to create a high-resolution map of the boundary between Earth's crust and mantle - known as the Moho discontinuity. The data collected by GOCE [17] has been used in a variety of applications, including:

- Geodesy and geophysics: the data has helped to determine the geoid with unprecedented accuracy, providing a global reference for measuring precise surface heights. Still, the data from the mission continues to be used in scientific research.

- Oceanography: by combining the geoid with sea surface height measurements, scientists can derive the ocean surface circulation patterns and the heat transport within the oceans, a significant factor in climate change.
- Solid Earth physics: the data has facilitated improved our knowledge of Earth's interior, such as the lithosphere, upper mantle, and the boundary between the crust and mantle.
- Climate change study: the data has been employed to understand better sea-level changes and ocean circulation patterns, critical components of the Earth's climate system.
- Space science: the data has been used to improve the accuracy of the tracking data for other Earth observation satellites.

The satellite's primary payload was the Electrostatic Gravity Gradiometer [18], shown in Fig.2.1b. This instrument comprised three pairs of capacitive accelerometers, organized in a three-dimensional configuration, that detected minuscule changes in Earth's 'gravitational tug' as the satellite moved along its orbit. Due to their distinct locations within the gravitational field, each accelerometer uniquely experienced Earth's gravitational acceleration. The tri-axial arrangement of the gradiometer enabled the simultaneous measurement of the five independent elements of the gravity gradient tensor.

The mission concluded in 2013, having charted the fluctuations in Earth's gravity with extraordinary precision [19]. The information gathered by the satellite was subsequently utilized to generate the first high-resolution global map of the boundary separating Earth's crust and mantle. Among other findings, the satellite picked up gravity anomalies from the colossal earthquake that struck Japan on March 11, 2011 [20].

2.2.2 GRACE & GRACE-FO

The Gravity Recovery and Climate Experiment (GRACE) and its follow-on mission, GRACE Follow-On (GRACE-FO), shown in Fig.2.2, are pivotal missions in the field of Earth observation, which have significantly advanced our understanding of Earth's gravity field and climate. These missions are joint ventures of NASA,

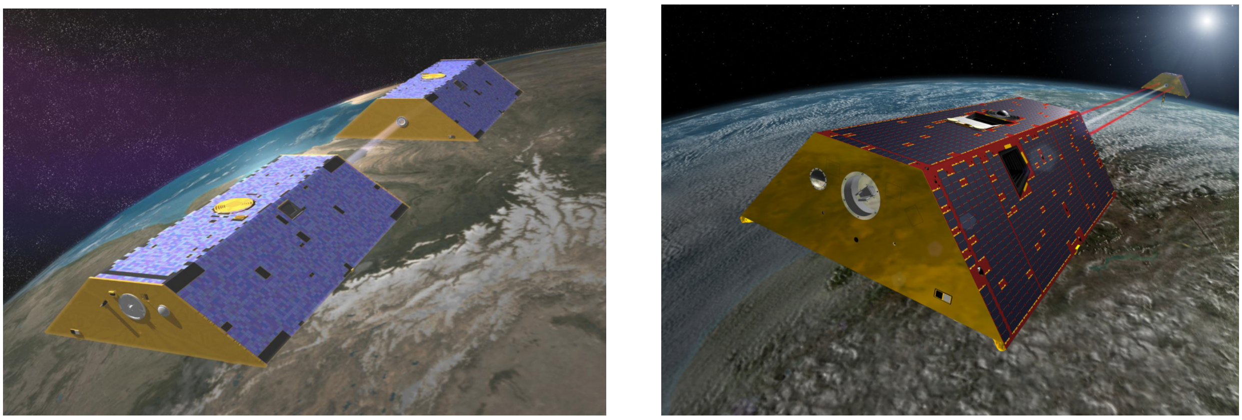

(a) GRACE. Credits: DLR **(b)** GRACE-FO. Credits: NASA/JPL-Caltech

Figure 2.2: The Gravity Recovery and Climate Experiment (GRACE) and its successor, GRACE Follow-On (GRACE-FO), are joint missions between NASA, the German Aerospace Center (DLR), and the German Research Centre for Geosciences (GFZ) aimed at precisely measuring variations in Earth's gravity field. These missions employ a pair of identical spacecraft flying in tandem to detect changes in Earth's gravitational pull, allowing scientists to monitor shifts in water and ice distribution and contributing to our understanding of climate change impacts. The GRACE and GRACE-FO missions have been instrumental in advancing Earth system science by offering insights into ocean currents, sea level changes, and processes within Earth's mantle.

the Deutsches Zentrum für Luft-und Raumfahrt (the German Aerospace Center or DLR), and the Deutsches GeoForschungsZentrum (German Research Centre for Geosciences or GFZ).

Launched in March 2002, the GRACE mission, shown in Fig.2.2a, consisted of two identical spacecraft flying about 220 km apart in a polar orbit 500 km above Earth [21]. The primary instrument on each spacecraft was a highly sensitive K-band microwave ranging system that could measure changes in the distance between the two spacecraft within a few micrometers. This allowed the detection of minute variations in the Earth's gravitational field as the two spacecraft moved over slightly stronger or weaker gravity areas. The GRACE mission provided a wealth of data over its 15-year lifespan. It made detailed measurements of Earth's gravity field, significantly improving our understanding of Earth's geophysical processes. This includes insights into the mass balance of Earth's polar ice sheets, aquifer water storage, and the solid Earth's response to post-glacial rebound.

The GRACE-FO mission [22], launched in May 2018, continues the work of the original GRACE mission. In addition to the microwave ranging system, GRACE-FO includes a new experimental instrument, the Laser Ranging Interferometer (LRI) [23]. The LRI is designed to measure the distance between the two spacecraft with even greater precision than the microwave system, potentially leading to improved gravity field measurements. The system also enables the measurement of the angle between the two spacecraft and their separation through differential wavefront sensing (DWS) [24]. After one year of operations, the first laser interferometer between two satellites exceeded all expectations, measuring about 200 times more precisely than the established microwave technology and thereby performed a factor of 20 better than the mission requirement specified [25].

GRACE and GRACE-FO employ test mass sensing in the accelerometers (ACC) onboard. These ACCs are used to measure non-gravitational accelerations (like imbalanced thruster firings, and non-gravitational environmental effects, such as atmospheric drag and solar and Earth radiation pressures) on the spacecraft, distinguishing these effects on the spacecraft's center of mass from those caused by gravitational accelerations, which constitute the measurements of interest. The data from the GRACE and GRACE-FO missions have had wide-ranging impacts. They have been used to monitor changes in ice sheets and glaciers [26], track water storage in underground aquifers [27], and even study sea level changes [28]. This information is crucial for understanding and predicting the impacts of climate change, managing water resources, and understanding natural hazards like earthquakes and volcanic activities. GRACE and GRACE-FO missions represent significant advancements in Earth observation. By providing detailed measurements of Earth's gravity field, these missions have enhanced our understanding of various geophysical processes and the impacts of climate change [29]; also, the first laser interferometer between two satellites is a successful step towards the space-based gravitational-wave observatory LISA.

2.2.3 LISA Pathfinder

LISA Pathfinder is a pioneering mission by the ESA designed to demonstrate some of the technology necessary for detecting gravitational waves in space [30]. Launched in December 2015, the spacecraft, shown in Fig.2.3a was a precursor to the LISA mission, which aims to directly observe gravitational waves of low frequency that are inaccessible to ground-based observatories. The core component of the LISA Pathfinder mission was the LISA Technology Package (LTP), shown in Fig.2.3b, which was designed to test and validate the technologies and techniques that will be used in the future LISA mission. The LTP includes the concept of free-falling test masses in space [31], a crucial requirement for detecting gravitational waves where these test masses will be isolated from external disturbances. The spacecraft housed two identical gold-platinum cubes of about 2 kg, acting as

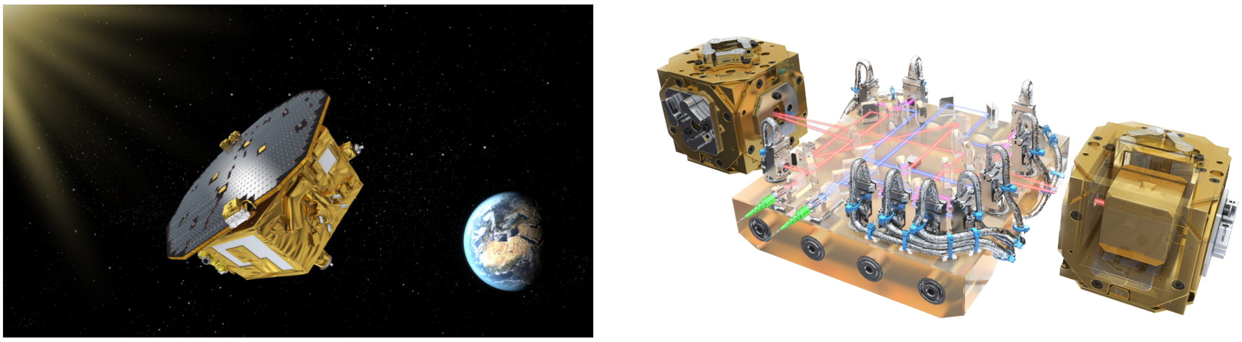

(a) Artistic view of LISA Pathfinder in space. Credits: ESA - C.Carrerau

(b) Artist's impression of the LISA Technology Package core assembly. Credits: ESA/ATG medialab

Figure 2.3: Artistic view of LISA Pathfinder in space and the LISA Technology Package core assembly. The mission, launched by the European Space Agency in 2015, was designed as a proof-of-concept for the technology necessary to detect gravitational waves from space, particularly testing the concept of free-fall precision. The heart of the LISA Pathfinder was the LISA Technology Package (LTP), which comprised two test masses housed in independent vacuum enclosures and an optical metrology system to monitor their relative positions. The successful operation of the LTP confirmed the possibility of placing objects in near-perfect gravitational free-fall, a critical step towards the future Laser Interferometer Space Antenna (LISA) mission for observing gravitational waves.

test masses, separated by a distance of about 38 cm. These test masses were in a nearly perfect gravitational free-fall, and their relative motion was measured by a laser interferometer [32, 33]. The mission successfully demonstrated that the relative acceleration of the test masses could be measured with a precision one order of magnitude better than initially required [34, 35]. This unprecedented accuracy was achieved by isolating the test masses from non-gravitational forces to a degree never before accomplished, thereby paving the way for the future LISA mission.

The LISA Pathfinder mission concluded in July 2017, having significantly exceeded its performance goals [36] and successfully proven that laser interferometric readout can be used to achieve much higher readout sensitivity. The success of the LISA Pathfinder has provided invaluable data and confidence in the technologies and methods used in the LISA mission, bringing us a step closer to detecting and understanding the gravitational universe.

2.2.4 LISA

The Laser Interferometer Space Antenna (LISA), as seen represented in Fig.2.4, is a planned mission by the European Space Agency (ESA) in collaboration with NASA, aiming to detect and measure gravitational waves-subtle ripples in the fab-

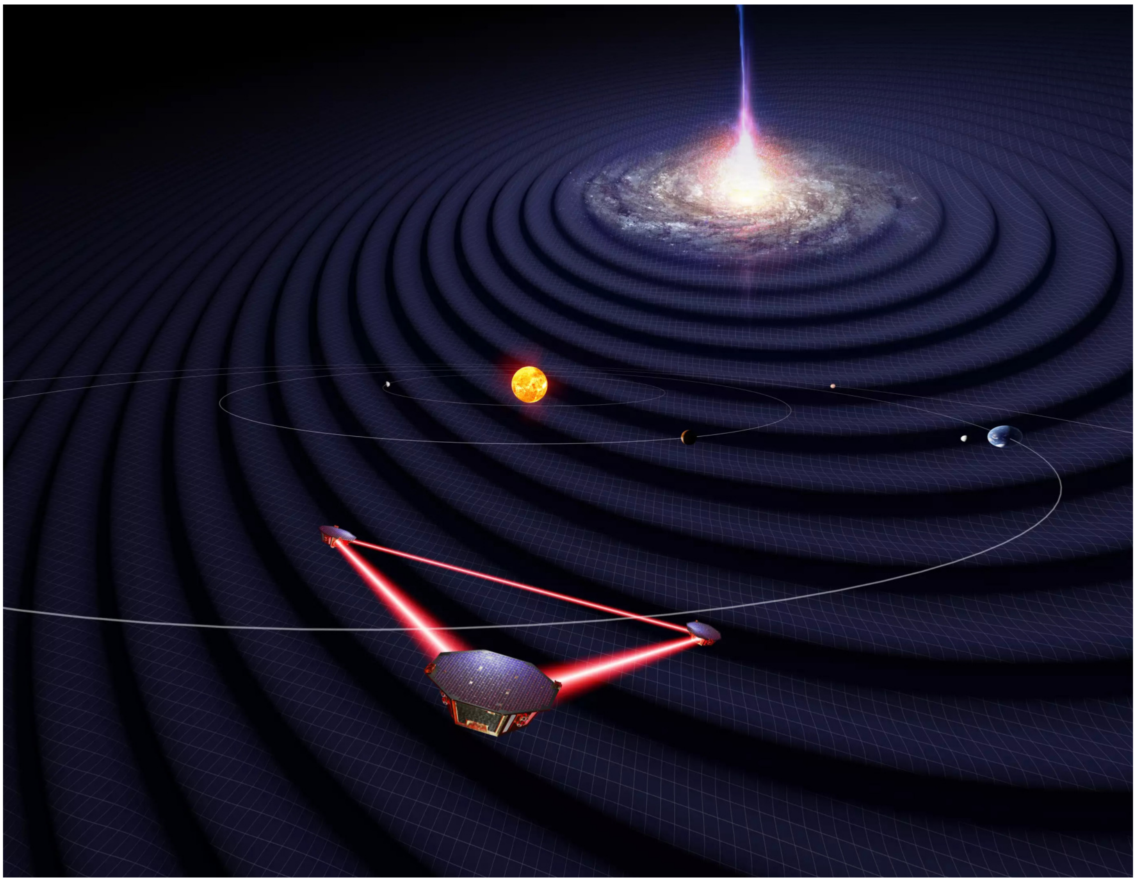

Figure 2.4: Artist's impression of the LISA mission satellites in the solar system observing gravitational waves from a distant galaxy. Credits: University of Florida / Simon Barke (CC BY 4.0)

ric of space-time from astronomical sources. LISA represents a significant milestone in gravitational wave astronomy, as it will be the first space-based gravitational wave detector.

Gravitational waves, first predicted by Albert Einstein's theory of general relativity, are generated by the acceleration of massive objects in the universe. These waves travel at the speed of light, carrying information about their violent origins and the nature of gravity that traditional astronomical tools cannot obtain. Detecting these waves provides a unique observational window into the universe, allowing the study of otherwise inaccessible phenomena.

Expected to be launched in 2034, the LISA mission will consist of a constellation of three spacecraft arranged in a near-equilateral triangle formation, separating 2.5 million kilometers each following heliocentric orbits (and out of the ecliptic). The three spacecraft will be connected by laser interferometry to measure the minute distance changes between them caused by passing gravitational waves.

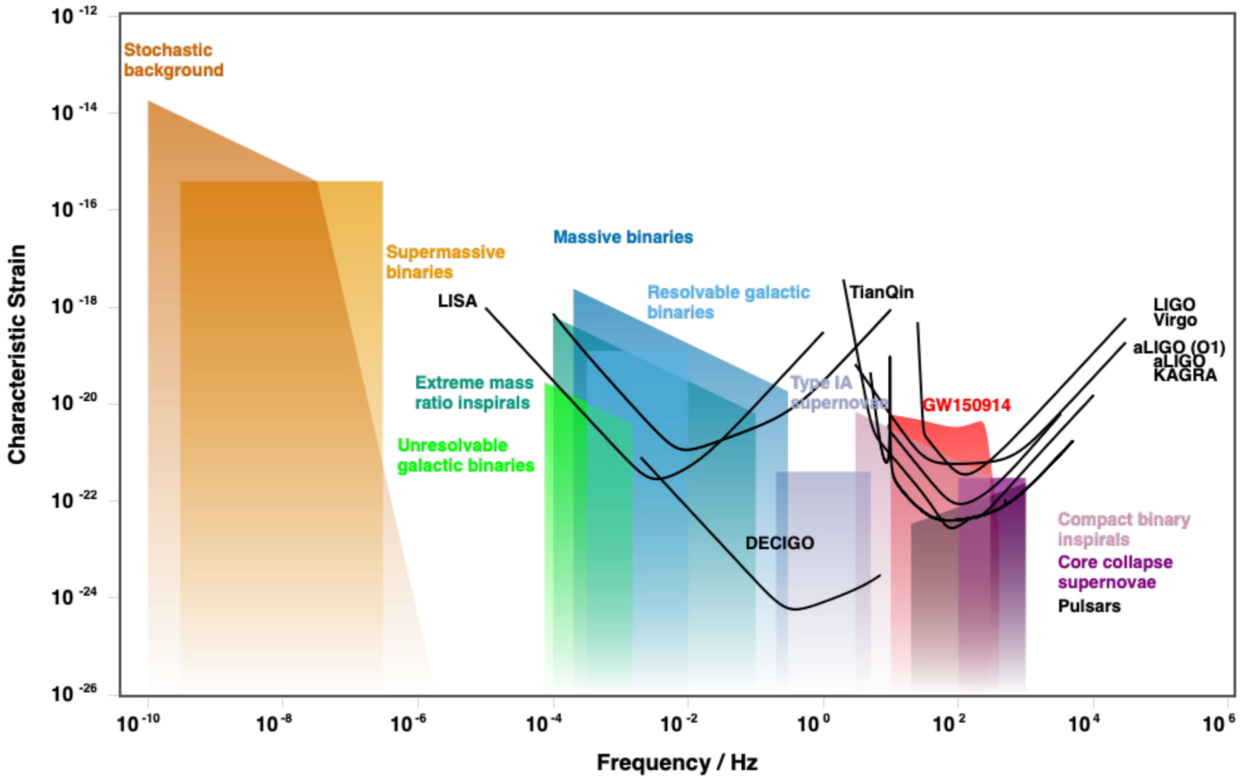

Figure 2.5: Plot of characteristic strain against frequency for various detectors and sources. Credits: http://gwplotter.com

The primary sources of gravitational waves that LISA aims to detect include binary systems of massive black holes, extreme mass ratio inspirals (small objects spiraling into massive black holes), and possibly even relics of gravitational waves from the early universe. The frequency range that LISA is sensitive to (0.1 mHz to 1 Hz) is much lower than that of ground-based detectors like LIGO, making LISA complementary to these detectors, as seen in Fig.2.5.

The successful operation of LISA requires several technological innovations already demonstrated in LISA Pathfinder. These include drag-free control, which allows the spacecraft to follow a test mass in free-fall, with no forces acting on it other than gravity, and precise laser interferometry to measure the distance between the test masses to a precision of a few $\mathrm{pm}/\sqrt{\mathrm{Hz}}$ [33].

The LISA mission will represent a significant step forward in our ability to detect and study gravitational waves, and it is expected to open a new window into the universe, providing a unique tool for testing the theory of general relativity and exploring the nature of the most violent and energetic processes in the cosmos.

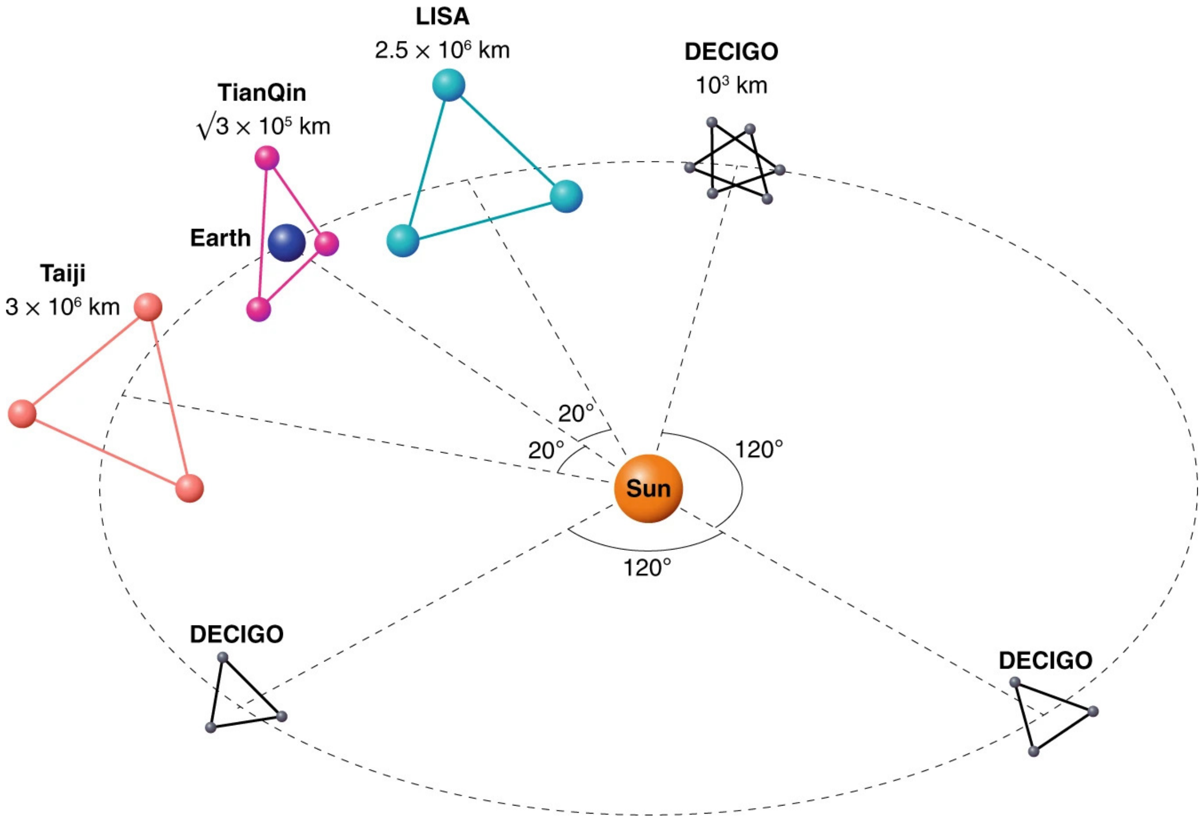

Figure 2.6: Schematic of different space-based gravitational waves detector constellations. Credits:[37]

2.2.5 Other gravitational waves detectors in space projects

Currently, gravitational waves detectors in space are an active research area in the USA or Europe, China, and Japan [37]. Fig.2.6 shows a schematic of different Space-based gravitational waves detector constellations. In China, the TianQin mission is a proposed space-based gravitational wave observatory led by Sun Yat-sen University to detect low-frequency (0.1 mHz - 1 Hz) gravitational waves. Planned to consist of three spacecraft in an equilateral triangular constellation orbiting around the Earth (where the distance between each pair of spacecraft is approximately 1.7×10^5 km), it will employ laser interferometry to measure the minute changes in distances between the spacecraft caused by passing gravitational waves. The mission, anticipated to launch around in the 2030 decade, is expected to contribute significantly to our understanding of the universe by observing phenomena like the mergers of supermassive black holes [38].

Another ambitious endeavor to detect gravitational waves in space is the Taiji project, proposed by the Chinese Academy of Sciences (CAS) [39]. The Taiji project's design proposes the deployment of three spacecraft arranged in an equilateral triangle. The detector will operate in the millihertz frequency band, complementing the LISA mission, which operates in a similar frequency band. By targeting this frequency band, Taiji and LISA will be able to detect gravitational waves emitted by supermassive black hole binaries, extreme mass ratio inspirals, and other cosmological sources that ground-based detectors like LIGO cannot observe. Cooperation between the Taiji and LISA missions could significantly benefit the field of gravitational wave astronomy. Joint observations could improve source localization, allowing astronomers to pinpoint the origin of gravitational waves with greater precision. The Taiji mission is in the design and research stage, intending to launch the spacecraft in the 2030s. As the project progresses, it is expected to contribute significantly to gravitational wave astronomy, fundamental physics, and cosmology.

Japan has been involved in gravitational wave research through the KAGRA project, a ground-based interferometer in the Kamioka mine. In addition, Japan has also proposed the DECIGO mission (DECI-Hertz interferometer Gravitational wave Observatory). DECIGO is a space-based gravitational wave observatory that aims to detect and observe gravitational waves in the deci-hertz frequency band. This mission is designed to fill the observational gap between ground-based detectors. By studying these gravitational waves, DECIGO seeks to probe the early universe, including the inflation era, and improve our understanding of black holes and neutron stars [40].

2.3 Gravitational Reference Sensor

Determining and tracking the position of, or the distance between freely floating, macroscopic reference objects, typically test masses (TMs), is the underlying concept for precision inertial sensing and gravity-related satellite missions introduced in 2.1. A Gravitational Reference Sensor (GRS) is a type of inertial sensor designed to measure and monitor the relative motion of free-falling test masses in a nearly perfect gravitational environment, which also plays a crucial role in drag-free control systems [41]. The GRS comprises a free-floating dense metallic TM shielded by a housing structure, as shown in Fig.2.7. This housing protects the TM from external forces that could be produced by the spacecraft or the space environment. The position of the TM relative to the housing, which is affixed to the spacecraft, is measured using sensors. The spacecraft's thrusters are then instructed to maintain the spacecraft's center aligned with the TM. As a result, both the TM and the spacecraft are in a near-flawless free-fall orbiting the sun (only for

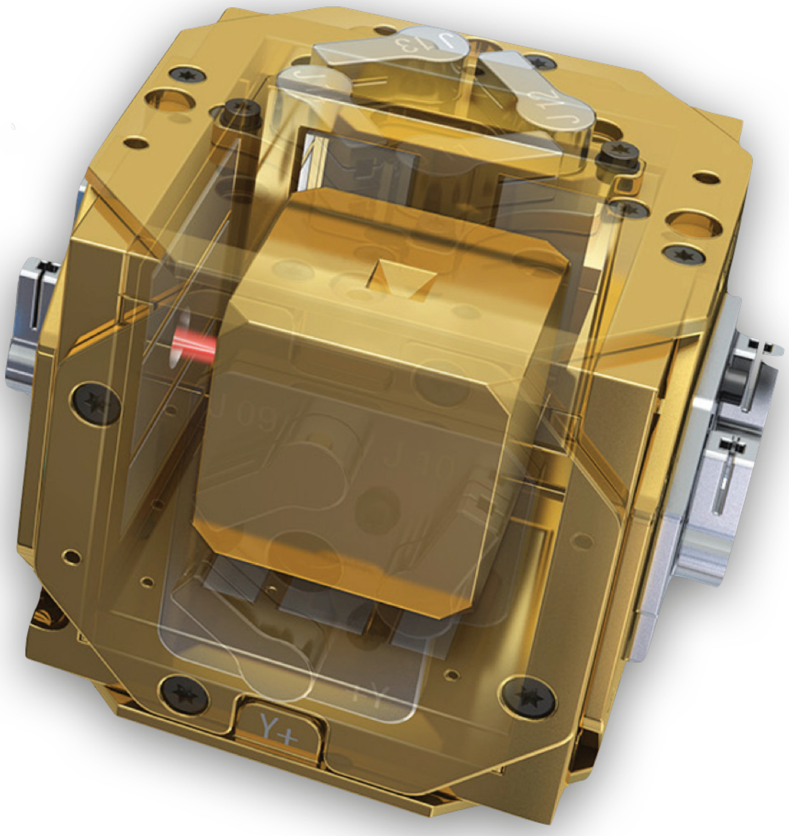

Figure 2.7: Single representation of the core assembly of the LISA Technology Package already described in Fig.2.3b. The original assembly features two gold cubes housed within a vacuum container, depicted here with the launch lock mechanism. These cubes are integral to the LISA Pathfinder mission, as each container holds a gold-platinum test mass. The LISA Pathfinder's objective is to observe these two cubes as they transition into a state of free-fall motion, utilizing a high-precision laser interferometer. Situated between the two masses is the optical bench interferometer. This device, constructed from a 20 cm by 20 cm block of Zerodur ceramic glass, has 22 mirrors and beam splitters affixed to its surface. These components are designed to direct laser beams, enabling scientists to accurately measure the cubes' motion, position, and orientation without physical contact. Therefore, the LISA Pathfinder is leading the inaugural high-precision laser interferometric tracking of orbiting bodies in space. Credits: ESA/ATG medialab

LISA). By measuring the spacecraft's orbit or the difference between the orbits of two drag-free spacecraft, it can gain insights into the spatial and temporal changes in the gravitational field.

Capacitive sensing is an established technique for measuring TM motion in high-precision space-borne experiments like LISA or LISA Pathfinder [42]. The electrodes for capacitive sensing are placed within the electrode housing. Since the TM is composed of a gold-platinum alloy, it effectively provides the other electrode for the capacitive sensing system. The setup comprising 18 electrodes (12 for sensing and 6 for injection) will facilitate six degrees of freedom, including three translational and three rotational, in both detection and control processes. Additionally, the system will incorporate UV light injectors into its charge management strategy. This charge management mechanism offers a contactless way of discharging the test masses. It achieves this by illuminating the inner surfaces of the GRS electrode housing and the test mass with light. Utilizing the photoelectric effect, it then enables electron transfer between the intended surfaces, effectively regulating the charge of the test mass [43]. The effective management of charge is critical for the smooth functioning of LISA. This is because the charge accumulation on the TM can heighten electrostatic stiffness and interact with errant magnetic fields, thereby inducing extra force noise on the TMs. In previous experiments with LISA Pathfinder, UV light injection was carried out using mercury lamps. Nevertheless, it is expected that LISA will shift towards using UV LEDs for charge management. This transition from mercury lamps to UV LEDs offers several benefits, including a decrease in mass, a smaller size, quicker response, and superior power efficiency.

GRS capacitive sensing provides an independent science readout of the TM position, which can be relevant, especially at low frequencies, where structural deformation of the system can dominate the white readout noise. The GRS is a crucial component of the LISA mission, providing a near-perfect gravitational free-fall environment for the test masses. The design and construction of the GRS involve intricate engineering and precise control systems to maintain the test masses in their ideal state. The performance of the GRS is critical to the mission's success, as any disturbances could potentially affect the accuracy of the gravitational wave measurements [44]. This performance is determined by the level of residual TM acceleration measured in units of $\mathrm{ms^{-2}\,Hz^{-1/2}}$ over a relevant frequency band. An increase in the mass of the test mass, coupled with an expansion in the gaps between the test mass and its housing (a measure that assists in mitigating undesirable surface interactions) and a slower thermal, gravitational, and electromagnetic environment within the spacecraft, collectively contribute to a decrease in acceleration noise levels. Nonetheless, these modifications, specifically the enlargement of gaps and the augmentation of the test mass, may inversely affect the sensitivity of capacitive sensors and the capacity to actuate the test mass.

The development and testing of the GRS have presented numerous challenges, including the need to minimize non-gravitational forces on the test masses, such as those caused by residual gas molecules, electrostatic forces, or even micrometeoroid events [45]. The successful deployment and operation of the GRS in missions like LISA Pathfinder have demonstrated the feasibility of using these sensors to detect and measure gravitational waves in space [46]. These achievements have validated the technology and paved the way for future missions to explore the universe through gravitational wave astronomy.

2.4 Testing free fall on ground

To test GRS on the ground, it is clear it has to be an apparatus made to mimic a free fall TM and able to measure the displacement of the TM in all six degrees of freedom (DoFs) with high sensitivity at low frequencies. Also, to test sub-$\mathrm{ms}^{-2}\,\mathrm{Hz}^{-1/2}$ inertial instruments at low frequencies (in this thesis, low frequencies are considered/referring to frequency regimes below 1Hz) is challenging. For that, torsion pendulums have been used to measure and test several aspects of precision inertial sensors.

One of the most known uses is in the experiment by Cavendish in the 18th century to measure the gravitational constant. Another notable experiment is the Eöt-Wash experiment by the University of Washington, which utilizes a torsion balance to test the equivalence principle with high precision [47]. This experiment has confirmed the principle to a high degree of accuracy.

Ground-based testing of the LISA Pathfinder gravitational sensors was performed in a torsion balance facility. This facility could measure weak forces exerted by a capacitive position sensor on a lightweight LISA TM suspended from a thin torsion fiber. In addition, it measures the residual spring-like coupling between the test mass and the sensor and the characterization of the stray forces relevant to LISA drag-free control. This residual acceleration noise on the test masses, which limits the sensitivity of LISA-like missions below a few mHz, uses the following requirement [48] given by

$$s_a^{1/2} < 3 \times 10^{-15} \left(1 + \left(\frac{f}{3\mathrm{mHz}} \right)^2 \right)^{1/2} \frac{\mathrm{m}}{\mathrm{s}^2\,\sqrt{\mathrm{Hz}}} \tag{2.1}$$

Currently, some universities are hosting a torsion balance for GRS and inertial sensing purposes. Huazhong University of Science and Technology (Wuhan, China) built some time ago a torsion balance for GRS purposes [49, 50]. In contrast, the University of Washington (USA) torsion balance is used to test thermal models of the LISA GRS [51]. Trento University (Italy) used a torsion bal-

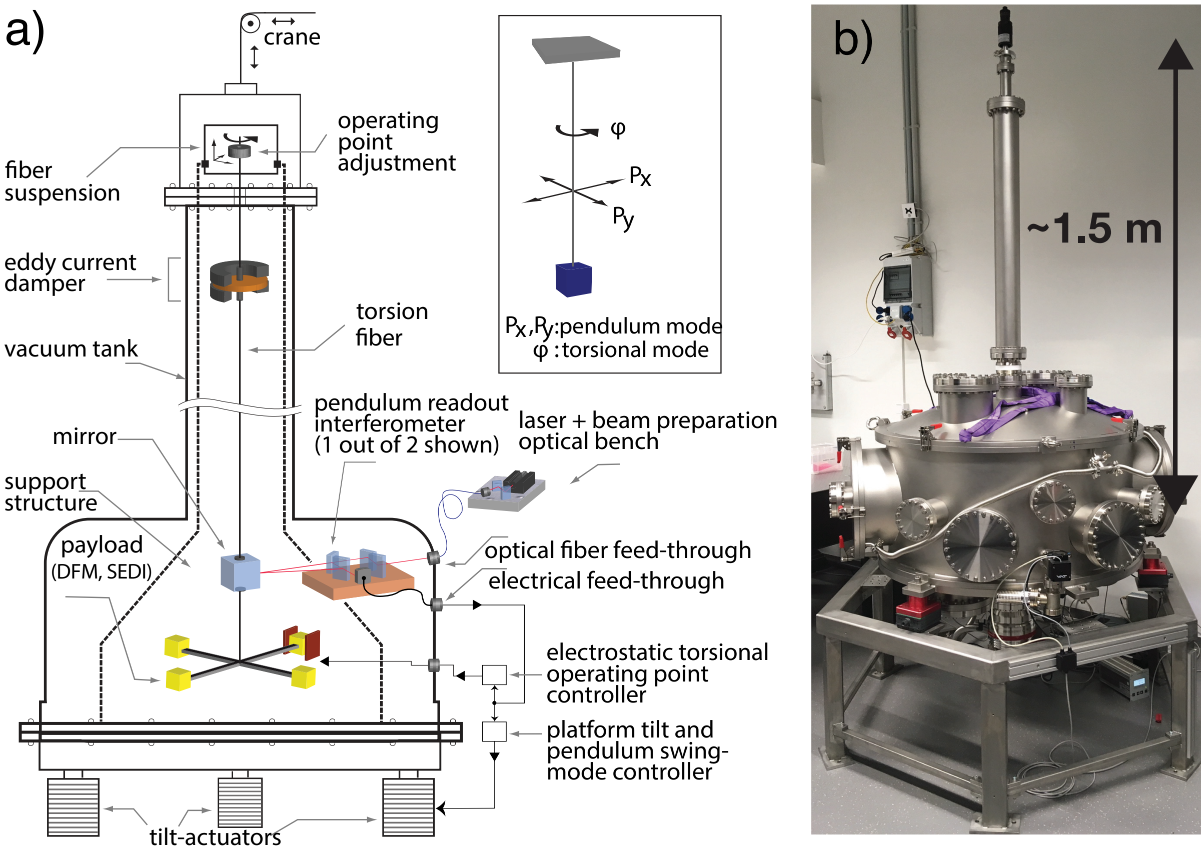

Figure 2.8: HITec Vacuum Chamber currently under construction. (a) shows a schematic drawing of the planned torsion balance setup with the planned payload, such as SEDI or DFM experiments. (b) shows a photograph of the vacuum tank designed to house a 1.5 m fiber. Made of stainless steel, it has a 600-liter volume weighing 700 kg. Credits: M. Mehmet

ance for many years to test the LISA and LISA Pathfinder GRS [52, 53], where their proposed torsion pendulum is limited by the intrinsic thermal noise at $\approx 3\times10^{-13}\,\mathrm{N\,Hz^{-1/2}}$ at 1 mHz [7, 54]. Alternatively, the University of Florida (USA) also developed a torsion balance to test new technologies for the LISA GRS. The performance of their pendulum, as determined by the measured residual torque noise and expressed in terms of equivalent force acting on a single test mass, is roughly $2\times10^{-13}\,\mathrm{N\,Hz^{-1/2}}$ around 2 mHz, which is about a factor of 20 above the thermal noise limit of the fiber [55].

It is worth noting that torsion pendulum experiments are very sensitive and require isolation from outside influences, like seismic vibrations, temperature fluctuations, and electromagnetic disturbances. Furthermore, these experiments demand precise measurements, often at the level of nanometers, requiring state-of-the-art instrumentation and technology. These experiments' continued testing and improvement will provide even stricter constraints on potential violations of the equivalence principle and our understanding of gravity. As such, torsion pendulum experiments remain a critical tool in the quest to probe and test the fundamental principles of physics.

At Leibniz Universität Hannover and the Max-Planck Institute for Gravitational Physics (Albert Einstein Institute), located in Hannover, Germany, a Torsion Balance (HITec Torsion Balance) is currently being established, as shown in Fig. 2.8. This initiative aims to create an exceptionally versatile, low-noise testing facility to evaluate innovative, high-precision optical inertial sensor units. The payload dynamics of the system are measured with capacitive sensors, which regulate the dynamics of low-frequency payloads and optical levers, achieving a sensitivity of $2.2 \times 10^{-11}\,\mathrm{m\,Hz^{-1/2}}$. Given its heightened sensitivity to ground motion, the HITec Torsion Balance emerges as a low-noise potential platform for the investigation of multi-degree-of-freedom ground motion sensing and also to test low-noise payloads such as compact interferometers (see Chapter 5) or novel interferometers like the ”Single Element Dual Interferometer” or SEDI (see Chapter 6), using Deep Frequency Modulation interferometry (see section 4.3), key points of this PhD thesis.

Part II

Optical Test Mass Readout

Chapter 3

Five DoFs optical test mass readout via optical levers

3.1 Introduction

In section 2.3, it was stated that the fundamental principle for precision inertial sensing and gravity-related satellite missions involves identifying and continuously monitoring the position or inter-object distance of freely floating macroscopic reference objects in several degrees of freedom (DoFs), typically referred to as test masses (or TMs). Missions like GRACE, GRACE-FO, and GOCE have used capacitive suspension for their accelerometers and gradiometer, respectively, where the science signal is derived from the feedback signal, which keeps the TM centered within the inertial sensor using capacitive coupling with its specifically designed housing, establishing the capacitive sensing as a trusted technique for the measurement of TM motion in high-precision space-borne experiments. Not only do these missions use capacitive sensing, but also LISA Pathfinder and LISA [31, 57, 58] used and will use capacitive sensing for the TM readout in all degrees of freedom.

The basic principle of a capacitive sensor operation for a single translational DoF, represented in Fig. 3.1, involves a pair of conductive plates or sensing electrodes, C1 and C2, and a TM. An oscillating injection voltage V_{inj} is used to polarize the TM, the impedance of which toward ground varies depending on its position. This variation is due to the changing capacitances C1 and C2, which adjust as the TM moves closer to one electrode or the other. When the TM is centered,

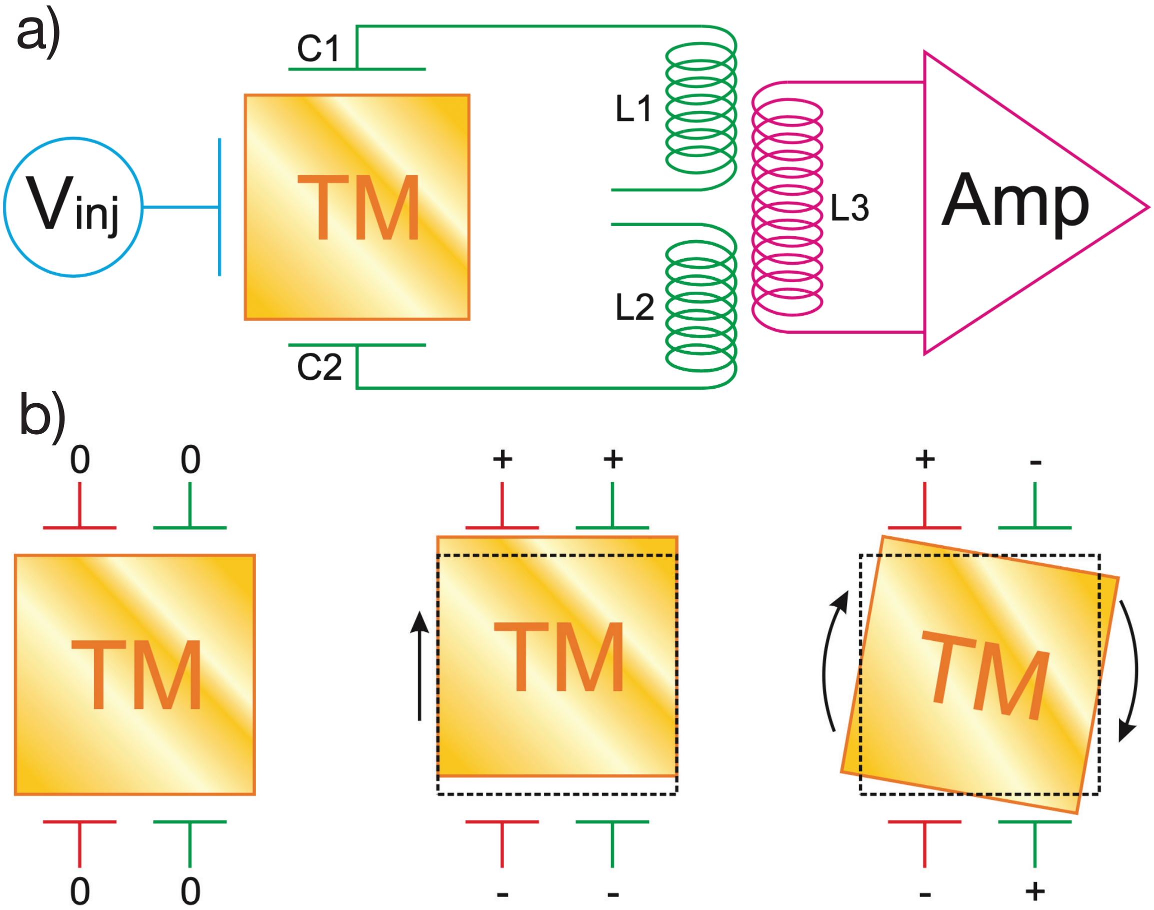

Figure 3.1: (a) A simple sketch that shows the operation of capacitive sensing along a translational DoF. An oscillatory voltage, V_{inj}, is employed to polarize the TM, whose impedance towards the ground depends on its position through the capacitances C1 and C2. These capacitances vary as the TM approaches one electrode or the other. The currents coursing through the two inductances, L1 and L2, which are equivalent when the TM is centered, diverge as it moves. Consequently, the magnetic fields they instigate in the overlapping inductances L1 and L2 no longer cancel each other, thereby inducing a current in L3 that is appropriately amplified. (b) A schematic representation of the sensing bridge arrangement on a pair of faces distinguishes a translational and a rotational DoF. Electrodes that are part of the same capacitive bridge share the same color, and the symbol adjacent to them denotes their capacitance fluctuation in response to the considered TM motion. It is observable that when the TM undergoes translation, the imbalance in capacitance exhibits the same sign across the two bridges. Conversely, if the TM experiences rotation, the imbalance manifests inversely across the two bridges. This facilitates the discrimination of the two DoFs. Image credits: [56]

the currents flowing in the two inductances L1 and L2 are equal, but these currents become unequal as the TM moves. Consequently, the magnetic fields induced in the overlapping inductances L1 and L2 no longer cancel out. This results in an induced current in L3, which is then suitably amplified.

Despite being the usual solution for satellite drag-free control, the main disadvantage of capacitive readout systems is the need for a tiny free gap between the two plates and then between the test mass and spacecraft. The standard gap value is usually less than 1 mm, whereas a gap exceeding a few mm is generally incompatible with the requisite sensitivity. The narrow free gap exhibits a high sensitivity to any net charge accumulation, such as that caused by cosmic rays, on either the test mass or the spacecraft. This severely constrains the maximum permissible rate of charge deposition and requires regular discharging through UV flash lamps [59]. Also, it is well known that test mass charging was a significant source of excess force and force noise in LISA Pathfinder [35]. Having small gaps also introduces problems, such as the patch field effect [60], which is caused by the spatial (and temporal) variation of the work function, which contributes to stray DC electrostatic fields. These fields couple with the time-varying charge of the surrounding electrode housing (and vice versa), introducing both forcing and sensing noise.

In order to find an alternative to capacitive readout, LISA Pathfinder has successfully proven that implementing laser interferometric readout, as it is represented in Fig. 3.2, can be used to achieve much higher readout sensitivity [33]. However, the interferometric system implemented in the LISA Pathfinder mission was limited to sensing one translational and two rotational degrees of freedom, and simple upscaling of this technology to achieve readout in 6-DoFs would be challenging in terms of optical complexity and payload dimensions.

In the context of the development process for the GRS intended for the LISA-Pathfinder mission, it has been shown that optical lever arms are a viable option when trying to overcome the limitations due to a capacitive readout scheme [61]. Measurements using a torsion pendulum resulted in a sensitivity of approximately $20\,\mathrm{nrad}/\sqrt{\mathrm{Hz}}$ at frequencies above $10\,\mathrm{mHz}$ obtained with a readout system based on a single optical lever sensed by a quadrant photodiode (QPD), which was about a factor of ten better than the reference sensitivity of the GRS [62]. The system was relatively simple and reliable but allowed for exceeding the sensitivity of the capacitive sensor in both translational and rotational DoFs in a wide range of frequencies and improving the sensitivity of the GRS [63, 64]. Optical levers have been widely used for several applications in different science branches, for example, for atomic force microscopy [65], to perform precision angle measurements in combination with interferometry [66], or for adhesion force studies [67]. Albeit not being sensitive enough to achieve laser interferometry precision, its simple optical setup and adaptability to pre-defined geometries make the optical lever a compelling approach, especially when aiming for an application where ultra-high

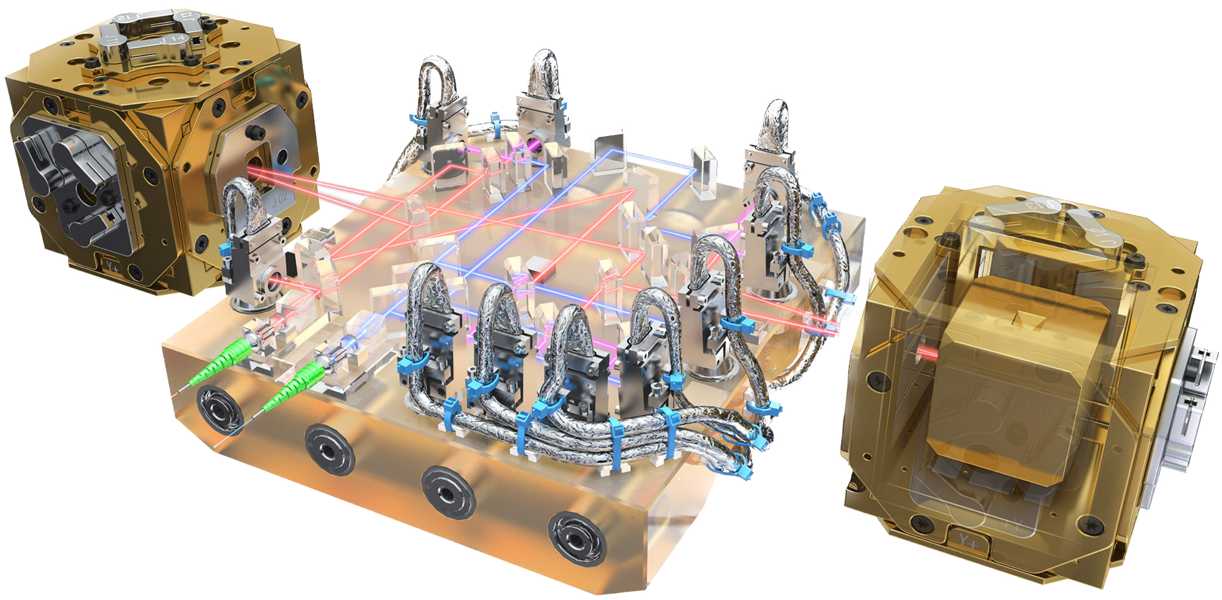

Figure 3.2: Artist's representation of the LISA Technology Package (LTP) onboard the LISA Pathfinder, where it is shown the two proof masses, 46-mm cubes made from a gold-platinum alloy, each enclosed in separate vacuum cans. These cubes function dually as mirrors for the laser interferometer, depicted by the red light paths, and as inertial references for the spacecraft's drag-free control system. Credits: ESA

precision is not required.

This chapter will extend what was published in [68]: the design and test of a readout scheme based on four optical lever arms generated from simple laser diodes reflected off a cubic TM and detected by four QPDs where the spatial arrangement of the setup allows for simultaneous sensing of five DoFs of the TM.

3.2 Simulating the TM motion with a hexapod

During the construction of the experiment, the HITec torsion balance was not yet built; therefore, using a hexapod was the only alternative to simulate TM motion. In short, a hexapod is a mechanical device that moves and positions objects in 6-DoFs. The six degrees of freedom include linear movements along the x, y, and z axes (longitudinal, transverse, and vertical) and rotational movements around these axes, typically termed pitch (rotation around the x axis), roll (rotation around the y axis), and yaw (rotation around the z axis). Hexapods can provide highly accurate and repeatable movements, which makes them ideal for precision applications. The use of parallel kinematics (where all actuators operate simultaneously) allows

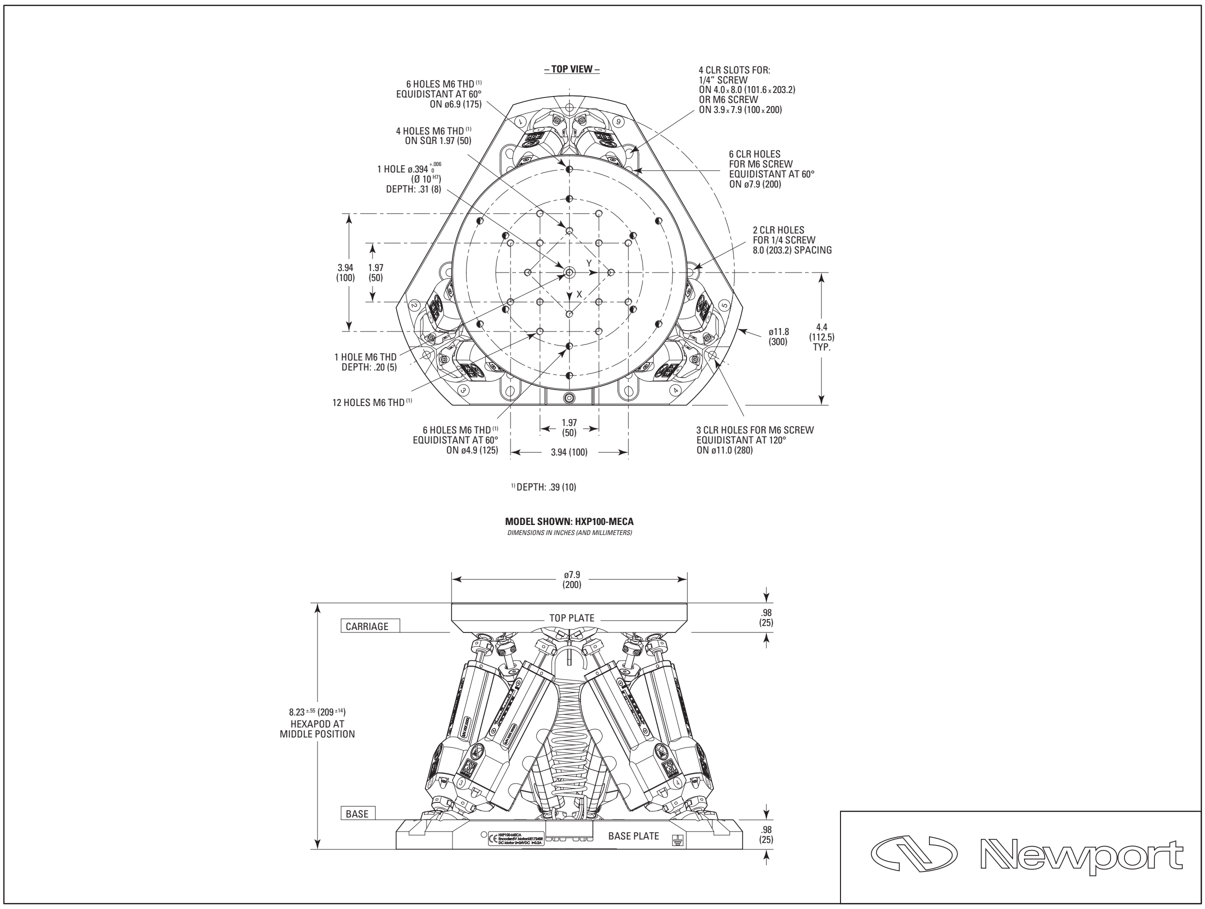

Figure 3.3: The HXP100-MECA 6-Axis Hexapod is a parallel kinematic motion device that provides six degrees of freedom: x, y, z, pitch, roll, and yaw. The HXP100-MECA has a 20 kg load capacity which was more than enough for the experimental purpose. Credits: Newport

them to achieve high stiffness and stability, enabling them to handle relatively large loads. Using six independent actuators also allows for a large workspace and flexible movements.

The hexapod used in the experiment was the model HXP100-MECA from Newport [69], represented in Fig. 3.3, where attached to the top of the hexapod is an aluminium cube with four gold-coated mirrors serving as a mock-up TM. The hexapod serves as an actuation system for arbitrary movements via its manufacturer-supplied computer interface, which is connected via LAN, allowing the user to define a virtual pivot point in space for all rotations. Lastly, several **Tcl** (Tool Command Language) scripts were written to move the hexapod along different DoFs, simulating a TM motion. Appendix A.1 and B.2 contain the **Tcl** code for the hexapod random motion and for the rotation along the z-axis, respectively.

The analysis presented in this Chapter focuses on the two translational DoFs (TM motion along x and y-axis) and the rotational DoF around the z-axis (θ). To first order, these DoFs contain the information of a TM suspended from a fiber as can be realized in a laboratory setup, for example, in the torsion balance facility. In this case, the science signal would be contained in θ while the residual pendulum swing modes could be extracted from the x and y signals. These, in turn, can be used to derive a suitable control signal for stabilizing the experimental platform of the torsion pendulum to provide seismic noise isolation. Conversely, the simultaneous measurement of the remaining rotational DoFs, ϕ and ψ (commonly referred to as the pitch and roll angles), will provide information on the associated residual cross-couplings for all measurements.

3.3 Experimental Setup

The optical setup is schematically shown in Fig. 3.4. Four standard laser diodes (Thorlabs CPS635R) with an output power of approximately 1 mW at 635 nm in a collimated beam of 2.9 mm diameter are reflected off four to the mock-up TM attached to the hexapod. Each reflected beam is detected by a silicon QPD with a total active area of 95 mm^2, split into four quadrants A, B, C, and D. The laser diodes and QPDs are rigidly mounted on a dedicated breadboard, which features a center hole to fit the hexapod and TM and was elevated to match the plane of the laser beams with the height of the TM. In this configuration, any movement of the TM, except for a translation along the z-axis, results in a simultaneous displacement of the light spot either on two opposing or all QPDs.

3.3.1 USB-interfaced electronics

A USB-interfaced electronics board was developed to drive the laser diodes and to readout the QPDs via a hybrid analog and digital modulation-demodulation scheme, used to avoid cross-talk between the individual laser beams and the effects of ambient light, as can be seen from Fig. 3.5. Each laser is intensity modulated at a frequency adjustable via an onboard field-programmable gate array (FPGA), and the frequencies were set to 21, 22, 23, and 24 kHz for LD1 to LD4, respectively. Sixteen trans-impedance amplifiers convert the resulting photo-currents of the quadrants into voltages, where the horizontal and vertical differential voltages for each photodetector are obtained by summing and subtracting circuits which

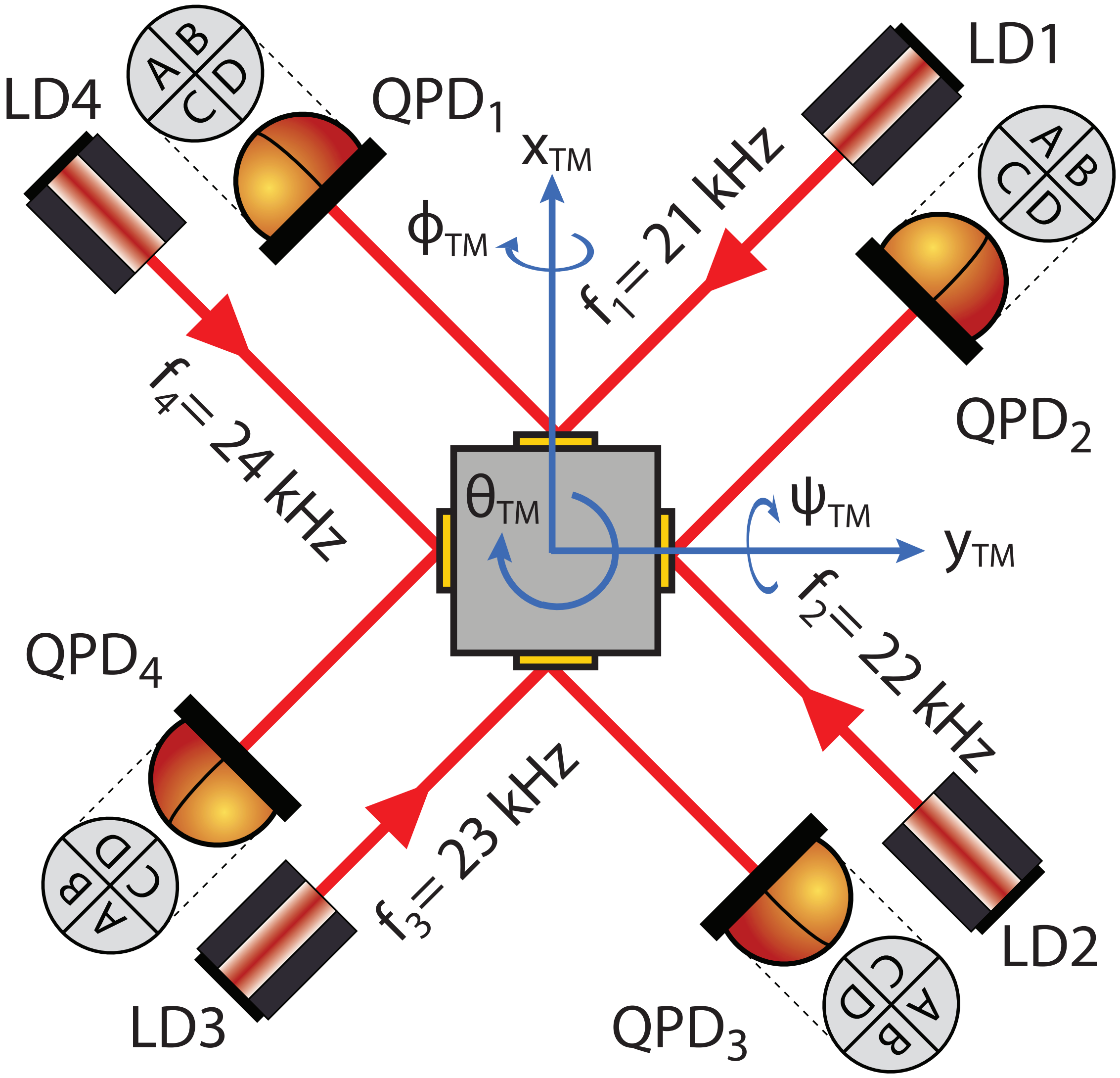

Figure 3.4: Optical configuration of the experimental setup. Four laser beams from simple laser diodes (LD) are reflected off the test mass mirrors and detected by four quadrant photodetectors (QPDs) with their active area divided into the quadrants A-B-C-D. The lasers are intensity modulated with different modulation frequencies f_1 to f_4.

generate $\Delta V_h \propto (A + C) - (B + D)$ and $\Delta V_v \propto (A + B) - (C + D)$, where they are demodulated by a multiplication with electrical copies of the respective modulation frequency; therefore, eight analog-to-digital converters are used to digitize the differential signals. The FPGA is then used to multiply these signals with an electrical copy (local oscillator) of their corresponding modulation frequency to obtain the measurement signals for each QPD. By using different frequencies and matching local oscillators for each of the four lasers and the respective QPD channel, the measurement signal of one optical lever arm is insensitive to stray light or residual reflections from the other three, as well as ambient light.

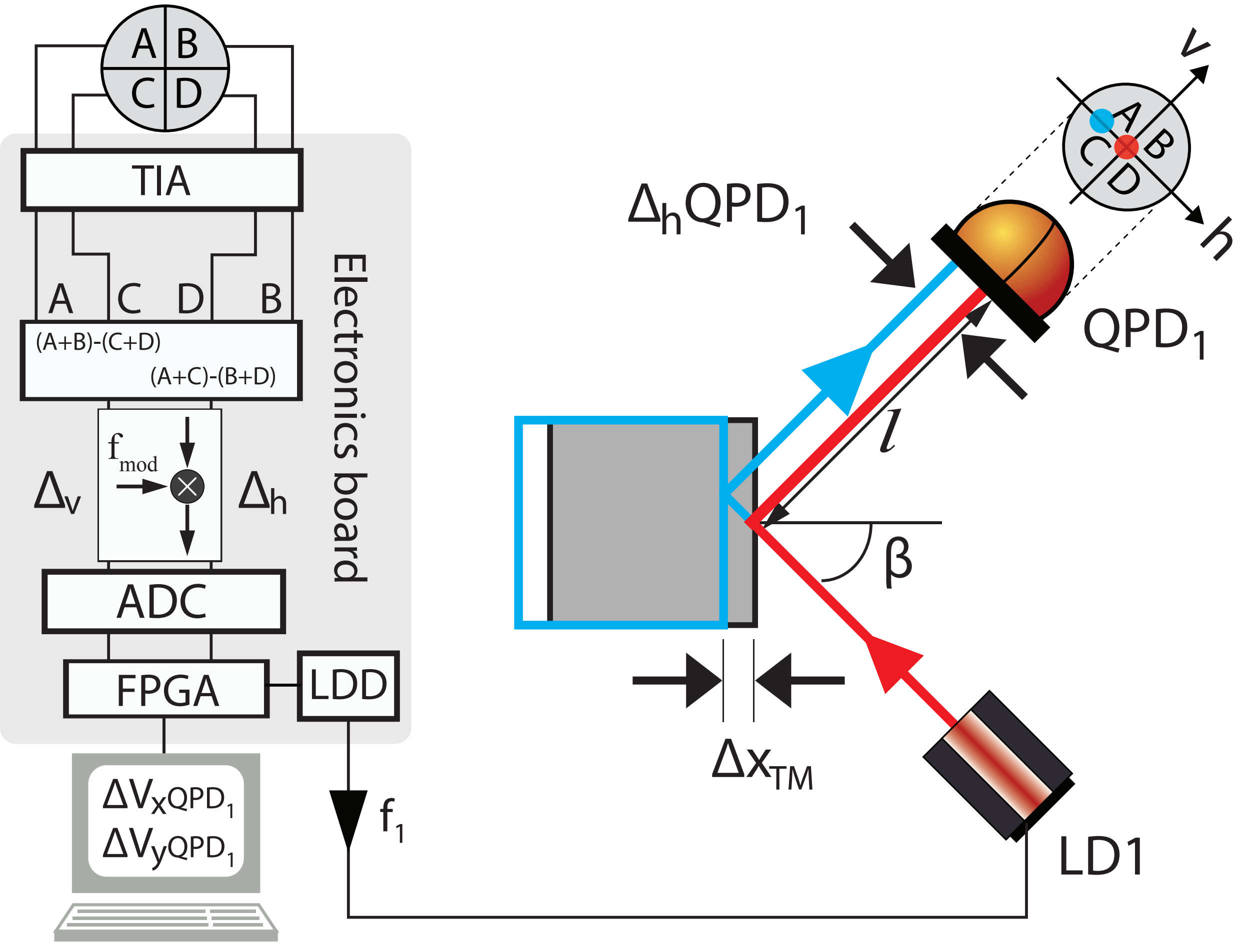

Figure 3.5: Geometry of a single optical lever and QPD with corresponding signal processing. A field programmable gate array (FPGA) is used for signal generation and data analysis. This board serves as the laser diode driver (LDD), supplying the modulation frequencies and as the data acquisition system for the QPD signals. For signal analysis, the board comprises a trans-impedance amplifier (TIA) stage followed by amplifier stages to obtain the horizontal and vertical differential voltages Δ_h and Δ_v, where they are demodulated by multiplication with electrical copies at the respective modulation frequency. These digital signals are mixed down and low-pass filtered in the FPGA, where the output signals are sent to a computer via USB for real-time data display, storage, and post-processing. In this setup, the total optical lever length l (from QPD to TM mirror) is 225 mm, and the angle of incidence $\beta = 45°$.

The output of the FPGA is a time series of the vertical and horizontal signals $\Delta V_{\mathrm{QPD}_{i,v}}$ and $\Delta V_{\mathrm{QPD}_{i,h}}$ $(i = 1, ..., 4)$, respectively, measured with a sampling rate of 1059 Hz and stored as a multi-column ASCII file which contains the information on the TM motion in five degrees of freedom: the translations along the x- and y-axis and the rotation around the z-axis given by θ, plus the rotation on the translational axes given by ϕ and ψ.

3.3.2 TM displacement mathematical description

As can be seen from Fig. 3.4, displacing the TM along the x-axis (Δx_{TM}), assuming perfect alignment, does not result in any displacement of the spot on QPD_2 and QPD_4, but yields a displacement $\Delta_h\mathrm{QPD}$ with opposite sign on the two detectors QPD_1 and QPD_3 that depends on the angle of incidence β ($0 < \beta < \pi/2$), and is given by

$$\Delta_h\mathrm{QPD}_{1,3}(\Delta x_{\mathrm{TM}}) = \pm 2\sin\beta \cdot \Delta x_{\mathrm{TM}}\,. \tag{3.1}$$

The displacement due to a TM rotation $\Delta\theta_{\mathrm{TM}}$ in the x-y-plane is a common mode on all detectors and depends on the optical lever length, l, measured from the TM mirror to the QPD:

$$\Delta_h\mathrm{QPD}_{1,2,3,4}(\Delta\theta_{\mathrm{TM}}) = 2l \cdot \Delta\theta_{\mathrm{TM}}\,, \tag{3.2}$$

where it is assumed equal lengths for all four optical levers. From Eq. 3.1 and Eq. 3.2 is evident that both motions contribute to the same differential signal, and therefore the total displacement for a TM motion along the x-axis is given by

$$\Delta_h\mathrm{QPD}_{1,3} = \pm 2\sin\beta \cdot \Delta x_{\mathrm{TM}} + 2l \cdot \Delta\theta_{\mathrm{TM}}\,, \tag{3.3}$$

and due to symmetry, QPD_1 and QPD_3 provide a similar expression for the TM motion along the y-axis,

$$\Delta_h\mathrm{QPD}_{2,4} = \pm 2\sin\beta \cdot \Delta y_{\mathrm{TM}} + 2l \cdot \Delta\theta_{\mathrm{TM}}\,. \tag{3.4}$$

The vertical displacements due to the pure rotation of the TM around the two remaining angular degrees of freedom ψ (rotation about x-axis) or ϕ (rotation about y-axis) contribute to the signals on two opposing sensors only. Since the laser is not perpendicular to the plane of rotation for these DoFs, the length of the optical lever scales with the cosine of the angle of incidence, yielding

$$\Delta_v\mathrm{QPD}_{1,3}(\Delta\psi_{\mathrm{TM}}) = \pm 2l\cos\beta \cdot \Delta\psi_{\mathrm{TM}}\,, \tag{3.5}$$

and likewise

$$\Delta_v \mathrm{QPD}_{2,4}(\Delta\phi_{\mathrm{TM}}) = \pm 2l\cos\beta \cdot \Delta\phi_{\mathrm{TM}}\,. \tag{3.6}$$

Consequently, the output voltages that are generated by the measurement device for any movement of the laser beams across the four QPDs can be described with the following matrix equation:

$$\underbrace{\begin{pmatrix} \Delta V_{\mathrm{QPD}1,v} \\ \Delta V_{\mathrm{QPD}1,h} \\ \Delta V_{\mathrm{QPD}2,v} \\ \Delta V_{\mathrm{QPD}2,h} \\ \Delta V_{\mathrm{QPD}3,v} \\ \Delta V_{\mathrm{QPD}3,h} \\ \Delta V_{\mathrm{QPD}4,v} \\ \Delta V_{\mathrm{QPD}4,h} \end{pmatrix}}_{\mathbf{\Delta V}} = \mathbf{C}\cdot \underbrace{\begin{pmatrix} 0 & 0 & 0 & 2l\cos\beta & 0 \\ 2\sin\beta & 0 & 2l & 0 & 0 \\ 0 & 0 & 0 & 0 & 2l\cos\beta \\ 0 & 2\sin\beta & 2l & 0 & 0 \\ 0 & 0 & 0 & -2l\cos\beta & 0 \\ -2\sin\beta & 0 & 2l & 0 & 0 \\ 0 & 0 & 0 & 0 & -2l\cos\beta \\ 0 & -2\sin\beta & 2l & 0 & 0 \end{pmatrix}}_{\mathbf{A}} \cdot \underbrace{\begin{pmatrix} \Delta x_{\mathrm{TM}} \\ \Delta y_{\mathrm{TM}} \\ \Delta\theta_{\mathrm{TM}} \\ \Delta\psi_{\mathrm{TM}} \\ \Delta\phi_{\mathrm{TM}} \end{pmatrix}}_{\mathbf{B}}, \tag{3.7}$$

where $\mathbf{\Delta V}$ comprises the vertical and horizontal output voltage signals, $\mathbf{A}$ is the 5×8 matrix that describes the geometric relationship between the five degrees of freedom of the TM and the eight displacement signals. The entries of $\mathbf{B}$ are the 5-DoFs of the TM. $\mathbf{C}$ is a diagonal matrix that contains eight calibration factors which comprise four factors ($\mathbf{C}_{i,h}$) for horizontal and four factors ($\mathbf{C}_{i,v}$) for vertical movement of the beam across the active area of the photodetector, respectively, where $i = (1, ..., 4)$ belong to the respective QPDs used in the setup, $l = 0.225\,\mathrm{m}$ is the optical lever length and $\beta = 45°$ is the angle of incidence.

To derive the TM readout from the raw data given by $\mathbf{\Delta V}$, it computed the inverse matrix $(\mathbf{C}\cdot\mathbf{A})^{-1}$ that links the output signals from the QPDs to the TM displacement. Since $\mathbf{C}\cdot\mathbf{A}$ is not a square matrix, it was computed $(\mathbf{C}\cdot\mathbf{A})^{-1}$ by using the left pseudo-inverse matrix $(\mathbf{C}\cdot\mathbf{A})^{-1}_{\mathrm{left}} = \left((\mathbf{C}\cdot\mathbf{A})^T(\mathbf{C}\cdot\mathbf{A})\right)^{-1}(\mathbf{C}\cdot\mathbf{A})^T$. Consequently, the readout of the TM for 5-DoFs can be finally computed as

$$\mathbf{B} = (\mathbf{C}\cdot\mathbf{A})^{-1}_{\mathrm{left}} \cdot \mathbf{\Delta V}\,. \tag{3.8}$$

3.3.3 Calibration factors

The calibration factors in the matrix **C**, as seen in the equation Eq. 3.7, depend on the shape of the laser beams hitting the sensitive area of the QPDs and the electronic gains of the amplification stages used to convert the incident light into differential voltages. **C** is diagonal due to the independence of each QPD, and since the lasers are different for each QPD, the values $\mathbf{C}_{i,h/v}$ will differ from one to another. To determine the calibration factors and the performance of the optical lever for arbitrary configurations, a numerical simulation was developed to predict the system's response to the motion of the TM. The model's input was the intensity matrices extracted from images of the laser intensity distributions. These were taken with a CMOS beam analyzer camera placed in the respective positions of the four QPDs. For example, the simulated differential power signal on QPD_2 due to the TM moving along the x-axis is plotted in Fig. 3.6. The inset shows the corresponding camera image of the beam impinging onto QPD_2.

From the analytical model given by Eq. 3.8, it can deduce how a change of the geometry and the beam shape will affect the measurements; for example, a smaller laser spot will reduce the dynamical range, while the slope and hence the sensitivity will increase equally for sensing Δx_{TM}, Δy_{TM} and $\Delta\theta_{\mathrm{TM}}$. From the model, the values of the calibrations factors $\mathbf{C}_{i,h/v}$ can be obtained by estimating the linear slope for $\Delta x \approx 0$ due to a horizontal beam displacement. To verify the results, a direct calibration for each QPD was performed. To this end, the response to horizontal beam displacement was measured by mounting each QPD on a micrometer translation stage. The voltage signal was recorded as a function of the displacement perpendicular to the incident laser beam. Subsequently, the slopes or calibration factors, $C_{i,h}$, were obtained by linear regression.

The good agreement between simulation and the directly measured calibrations factors allows the prediction of the corresponding factors for a vertical beam displacement, which are required for extraction of the rotation angles ψ_{TM} and ϕ_{TM}. The QPDs readout voltages can be normalized with respect to the maximum voltage found by pointing the laser spot onto one-half of the respective QPD. This voltage is then used as a dividing factor for all measurements. As long as the laser spot is inside the QPD, the normalized readout values $\Delta \mathrm{V}_{\mathrm{N,QPD}_i}$ are between [-1, 1]. A complete model for the vertical and horizontal QPD signals was obtained by assuming linearity and small displacements. The results of both experimental and computational values and their deviation are shown in Table 3.1.

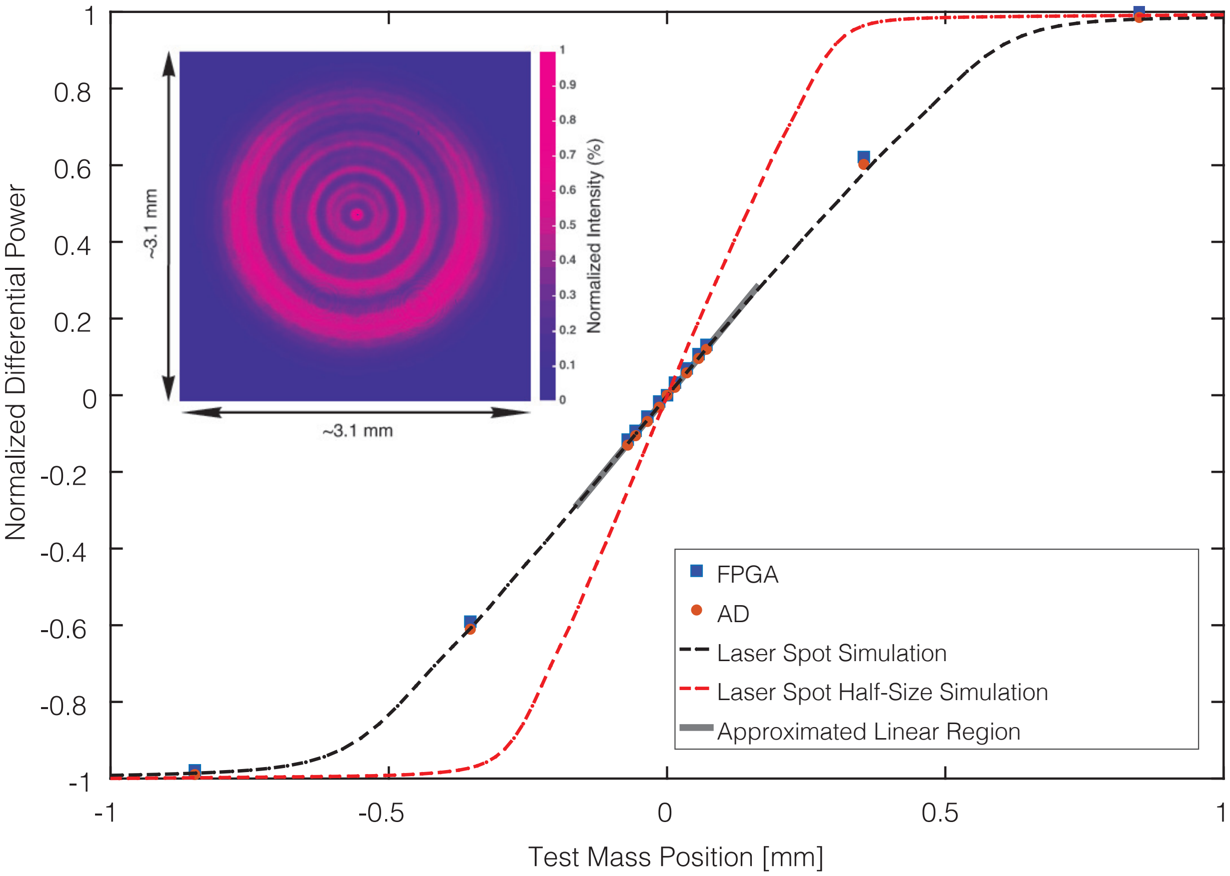

Figure 3.6: Differential output signal from QPD_2 due to TM motion along x-axis. The dashed black line is a simulation with the numerical model based on the intensity image of the beam impinging on QPD_2. The corresponding camera image is shown in the inset. The circular ring pattern is caused by diffraction at the laser diode apertures. From an estimate of the linear region (thick gray line), the calibration factor can be deduced via the optical lever's geometrical properties. The dashed red line shows a simulation of the system response for a laser spot with half the diameter. The blue squares and red dots are signals measured with the experimental system and an independent conventional analog readout circuit.

Cal. Factors	QPD_1 [m^{-1}]	QPD_2 [m^{-1}]	QPD_3 [m^{-1}]	QPD_4 [m^{-1}]
Exp. $\mathbf{C}_{i,h}$	943.4	878.1	874.4	858.2
Simulation $\mathbf{C}_{i,h}$	983.3	894.4	878.1	873.6
Deviation [%]	4.2	1.8	0.4	1.8
Simulation $\mathbf{C}_{i,v}$	1052.4	1025.4	1059	1141.3

Table 3.1: Normalised calibration factors $\mathbf{C}_{i,h,v}$. Values $\mathbf{C}_{i,h}$ were measured for each QPD and compared to the corresponding values obtained from the simulation. The average deviation is around 2 %. Since the standard deviation was below 1%, it was omitted in this table. The factors for vertical beam displacement $\mathbf{C}_{i,v}$ were derived from the simulation only.

3.4 Test Mass motion sensing

The hexapod was used to test the system response to a dynamic TM motion as an actuation stage. Different control programs written in **Tcl** were developed that allow the motion of the TM in x, y, and θ. Independent measurements were taken for the three types of hexapod motion. The resulting time series for the derived TM motion in five DoFs are plotted in Fig. 3.7 and Fig. 3.8. The longitudinal displacements along x and y are given in μm, and the rotation around θ is given in mrad.

3.4.1 TM displacement for x, y, and θ

Fig. 3.7 shows how the hexapod performed a motion from 0 to -300 μm and to +300 μm, respectively, for the two translational degrees of freedom. For the angular displacement, i.e., rotation around its vertical symmetry axis, the hexapod was programmed to perform a quasi-sinusoidal motion with an amplitude of ± 1.05 mrad, and period of $\sim$ 12.6 min. Appendix C.3 contains the Matlab code for the TM motion in five DoFs.

As expected, the derived signals for the associated intended motion (blue traces) are the most dominant for each column. For perfect symmetry, all remaining signals should be zero. However, due to imperfections of the setup, cross-couplings (red traces) to the other degrees of freedom were found for every motion. For example, the cross-couplings between x- and y motion can be explained by an angular mismatch of the TM coordinate system with respect to the hexapod basis. A deviation of only 5 μrad accounts for the observed coupling coefficient of 1/200 (3 μm cross-coupling due to 600 μm TM translation). The coupling of translation into the rotational degrees of freedom can be caused by non-parallel mirror surfaces, likely due to the limited accuracy of the mechanical construction. The cross-couplings for a hexapod rotation (right column) can result from a tilt and displacement mismatch between the z-axis of TM and hexapod. Furthermore, the cross-couplings also show a non-negligible hysteresis of the hexapod, as the start and stop positions for every motion were programmed to be the same. Still, the corresponding signals do not always match.

The three main degrees of freedom analyzed above were chosen because these describe the motion of a TM suspended from a thin fiber, as is the case in a torsion balance, and the first application of the HITec torsion balance will be to sense the corresponding motion to control and stabilize its operating point. Sensing the

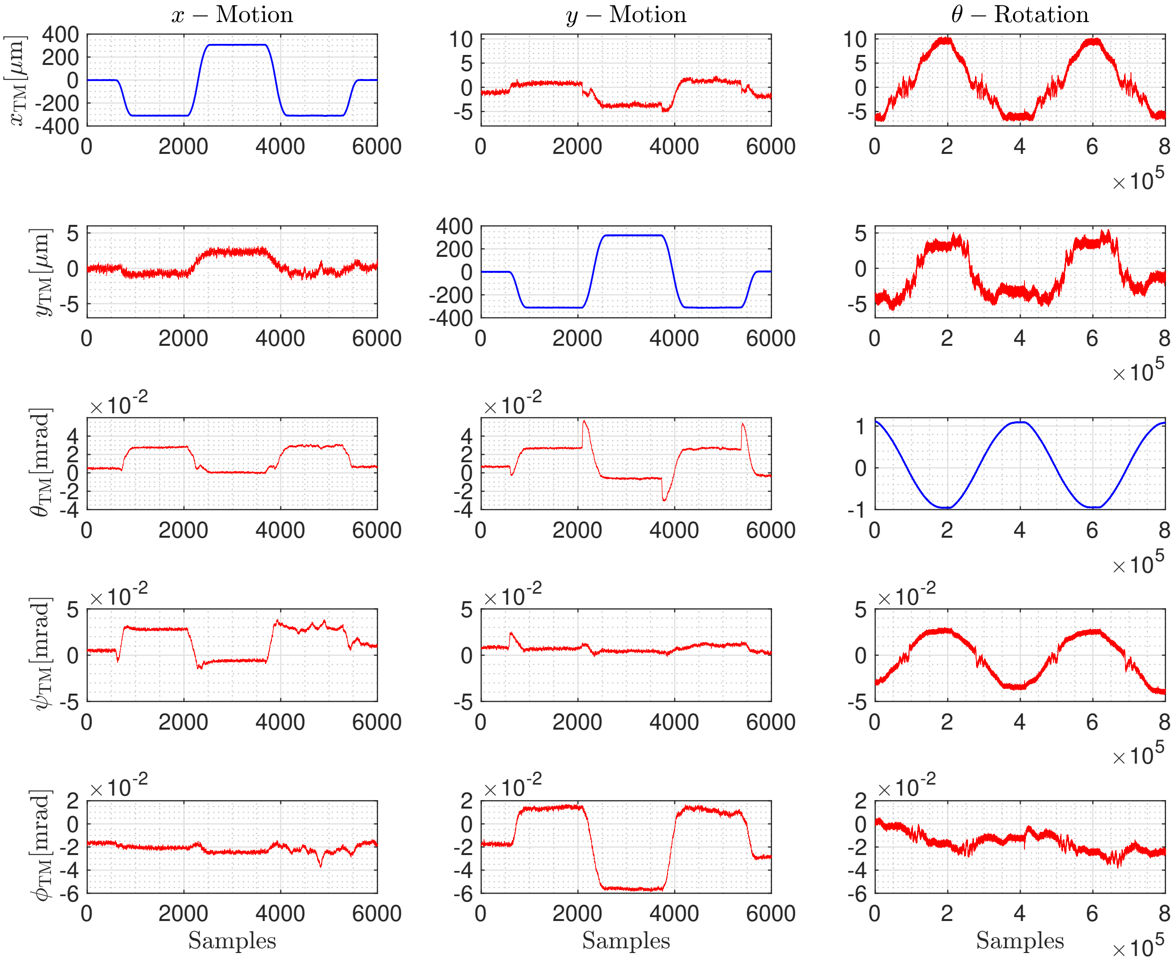

Figure 3.7: Analysis of five degrees of freedom of the TM. The signals in $x_{\rm TM}$, $y_{\rm TM}$, $\theta_{\rm TM}$, $\psi_{\rm TM}$, and $\phi_{\rm TM}$ as measured by the optical lever are plotted as a time series recorded with a sampling rate of 1059 Hz. Left column: data for x-motion of the hexapod. Center column: data for y-motion of the hexapod. The range of motion was $\mp 300\ \mu$m, where the TM translation was programmed to start from zero and return to zero after passing the minimum (maximum) twice (once). Right column: readout data for a test mass rotation around its vertical symmetry axis. A quasi-sinusoidal motion of two cycles with an amplitude of $\sim\ \pm 1.05$ mrad and period of $\sim$ 12.6 min. was applied to the hexapod. While the intended motions (blue traces) are the most prominent signal, the analysis also reveals cross-couplings in the other degrees of freedom (red traces).

associated pendulum swing modes requires knowledge about the TM translation while the science signal is contained in the rotation. By disentangling rotation from translation, it is planned to extract a suitable feedback signal to counteract the unwanted swing modes that are excited, for example, by the seismic coupling into the measurement band. The signals for the remaining two degrees of freedom, $\psi_{\rm TM}$ and $\phi_{\rm TM}$, will aid in mitigating cross-couplings and misalignments in a future setup. Later on, these signals will be helpful to study the behavior of the torsion balance under operation.

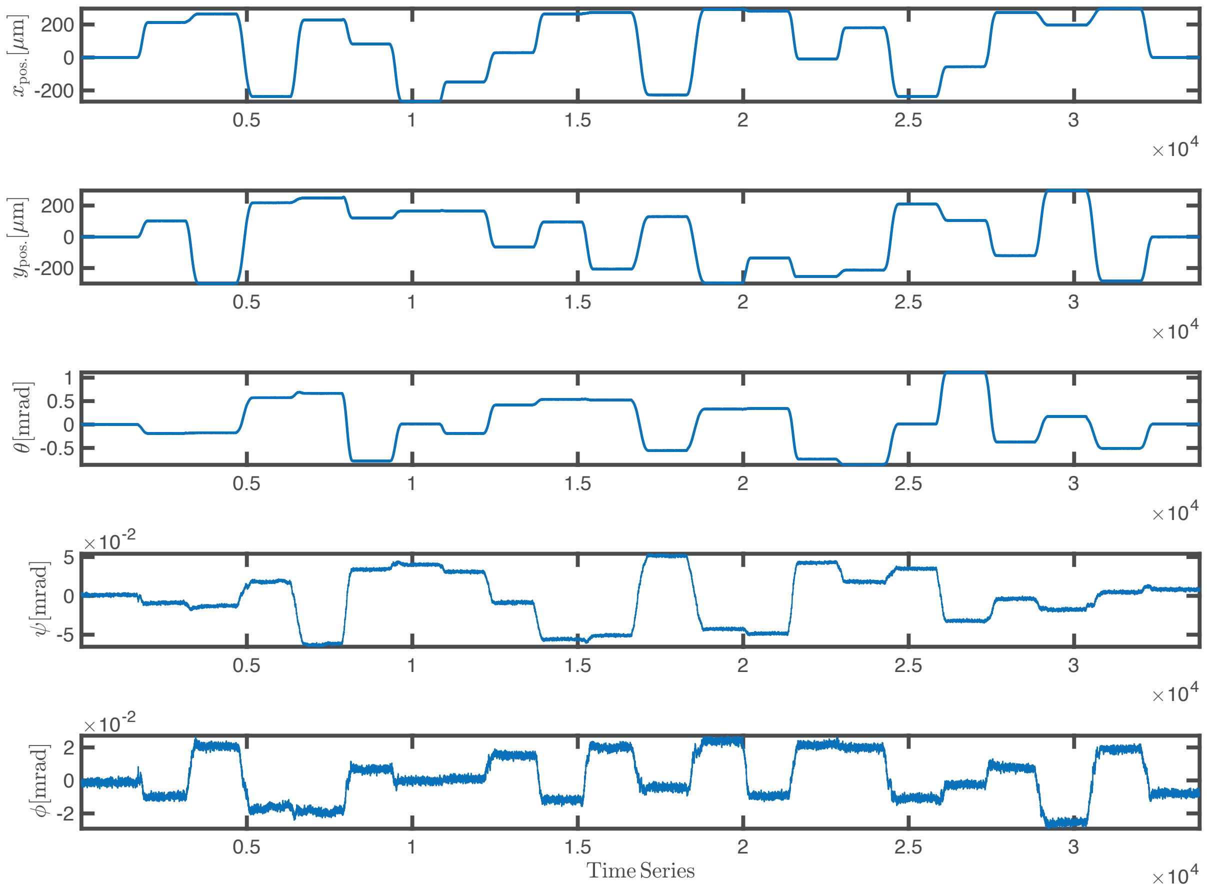

Figure 3.8: Time series of the TM random walk for x, y, and θ where it can be observed the cross-couplings in ψ and ϕ.

3.4.2 TM random walk for x, y, and θ

In the context of TM displacement, a random walk is a stochastic or random process that describes a path consisting of a succession of random steps. To test the hexapod performance and confirm the cross-couplings deviation in ψ and ϕ, a **Tcl** script was written to perform a random walk in three DoF: x, y, and θ. Fig. 3.8 shows the resulting time series for the input three DoF and the cross-couplings in ψ and ϕ, confirming a deviation of maximum 5×10^{-2} mrad for displacements of $200\,\mu$m, and rotations of 1 mrad.

3.5 Performance and sensitivity

To investigate the performance of the system, a simultaneous measurement of the TM motion θ_{TM} and ϕ_{TM}, with the optical levers and a commercial autocolli-

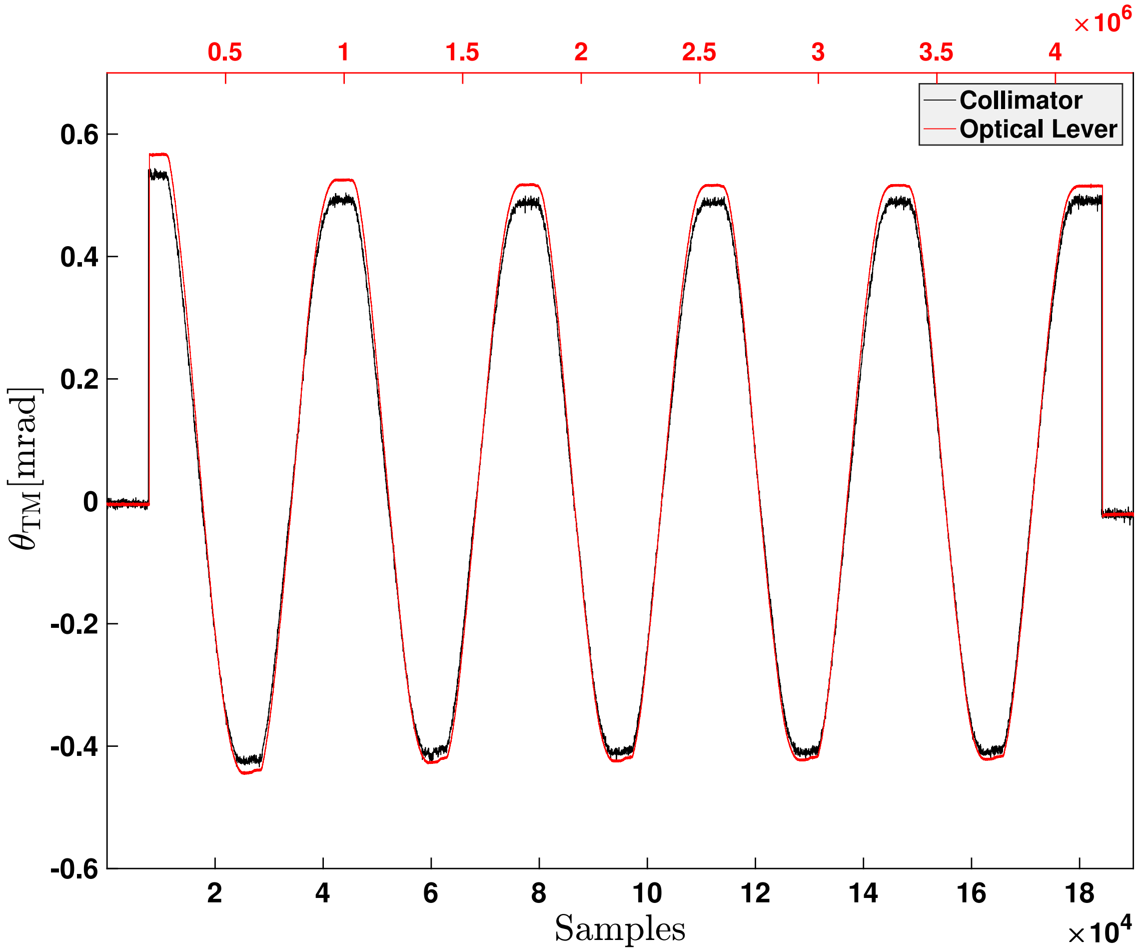

Figure 3.9: Readout of the angle θ measured simultaneously with the optical lever and autocollimator. Five cycles of a sinusoidal motion with an amplitude of ±0.5 mrad and a period of ~ 12.5 min. were performed.

mator (Trioptics TA 100-38), was conducted. The autocollimator measures small angular displacements by measuring the angle between its own transmitted and received collimated beam of light and is a standard tool to determine small angular displacements, for example, to align components in an optical setup and to detect small rotations of a reflecting surface such as a laser mirror. These devices are typically used to sense the rotation in torsion pendulum experiments [70].

Five cycles of a sinusoidal TM motion with an amplitude of ~ 0.5 mrad and period of ~ 12.6 min. were performed in each of the measurements. The sampling frequency of the acquisition was 1059 Hz for the optical lever and 44.5 Hz for the autocollimator acquisition. The readout of the TM rotation angle θ_{TM}, which is the nominal motion in this measurement, is plotted in Fig. 3.9. The difference in amplitude is probably caused by the misalignments present in the setup. Nevertheless, it was observed a good agreement between both data sets with a maximum

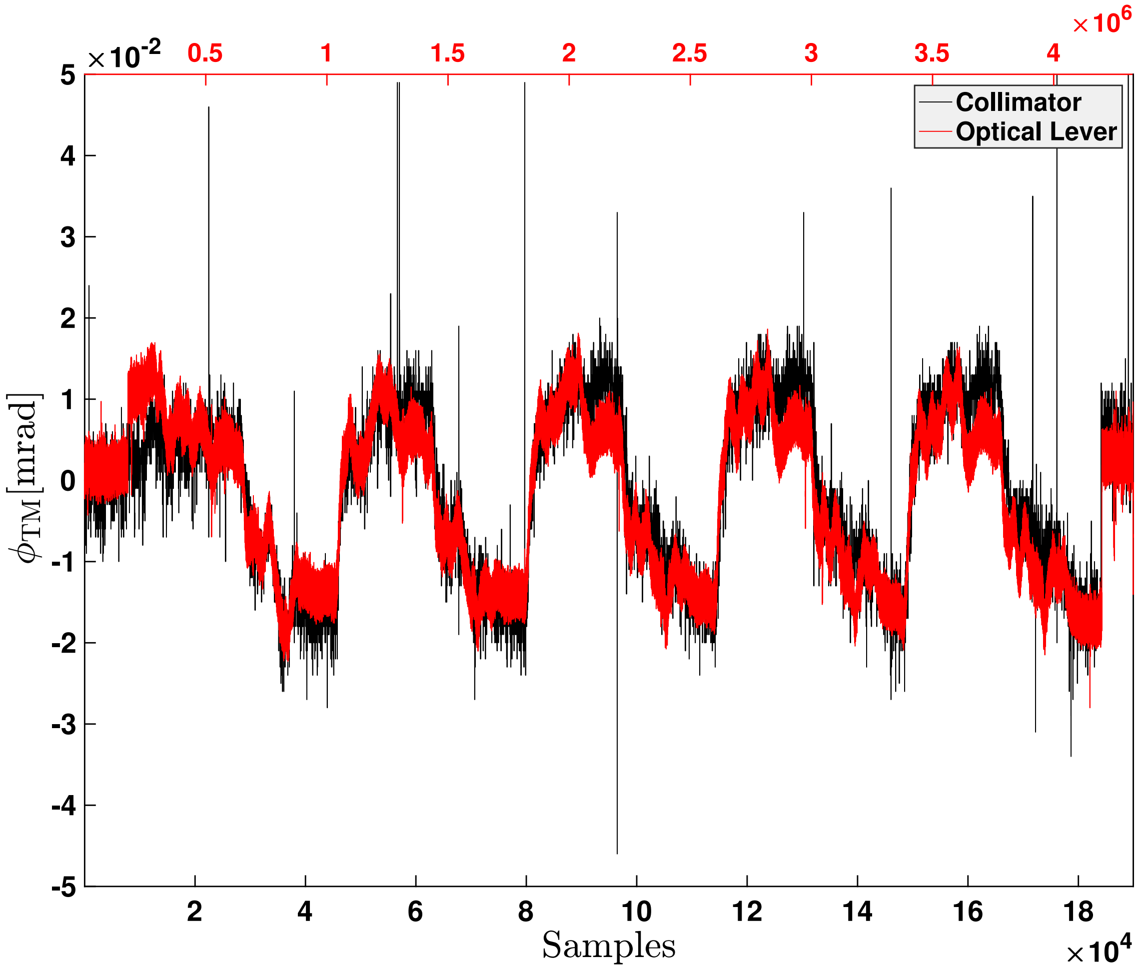

Figure 3.10: Simultaneous readout of the associated cross-coupling into the angle ϕ. As in the previous figure, five cycles of a sinusoidal motion with an amplitude of ±0.5 mrad, and a period of ~ 12.5 min. were performed. The sharp peaks were caused by electronic pick-up.

deviation of 5×10^{-2} mrad.

The associated cross-coupling into ϕ_{TM} is shown in Fig. 3.10. A discrepancy between the two measurement methods of $1\,\mu$rad was found. This is close to the resolution limit of the autocollimator, which, according to the technical data provided by the manufacturer, has a resolution of around $0.5\,\mu$rad, and accuracy of $12.5\,\mu$rad [71]. The sharp peaks in the collimator data are measurement artifacts, probably caused by electronic pick-up.

Fig. 3.11 and Fig. 3.12 display spectral densities of the angular sensitivity obtained from the measured times series via a Fourier transform algorithm [72, 73]. In Fig. 3.11, trace (a) was plotted as the spectral density of the electronic dark noise of the apparatus measured while in operation but with all laser diodes blocked such that no light was reaching the photodetectors. This trace lies at a level of around

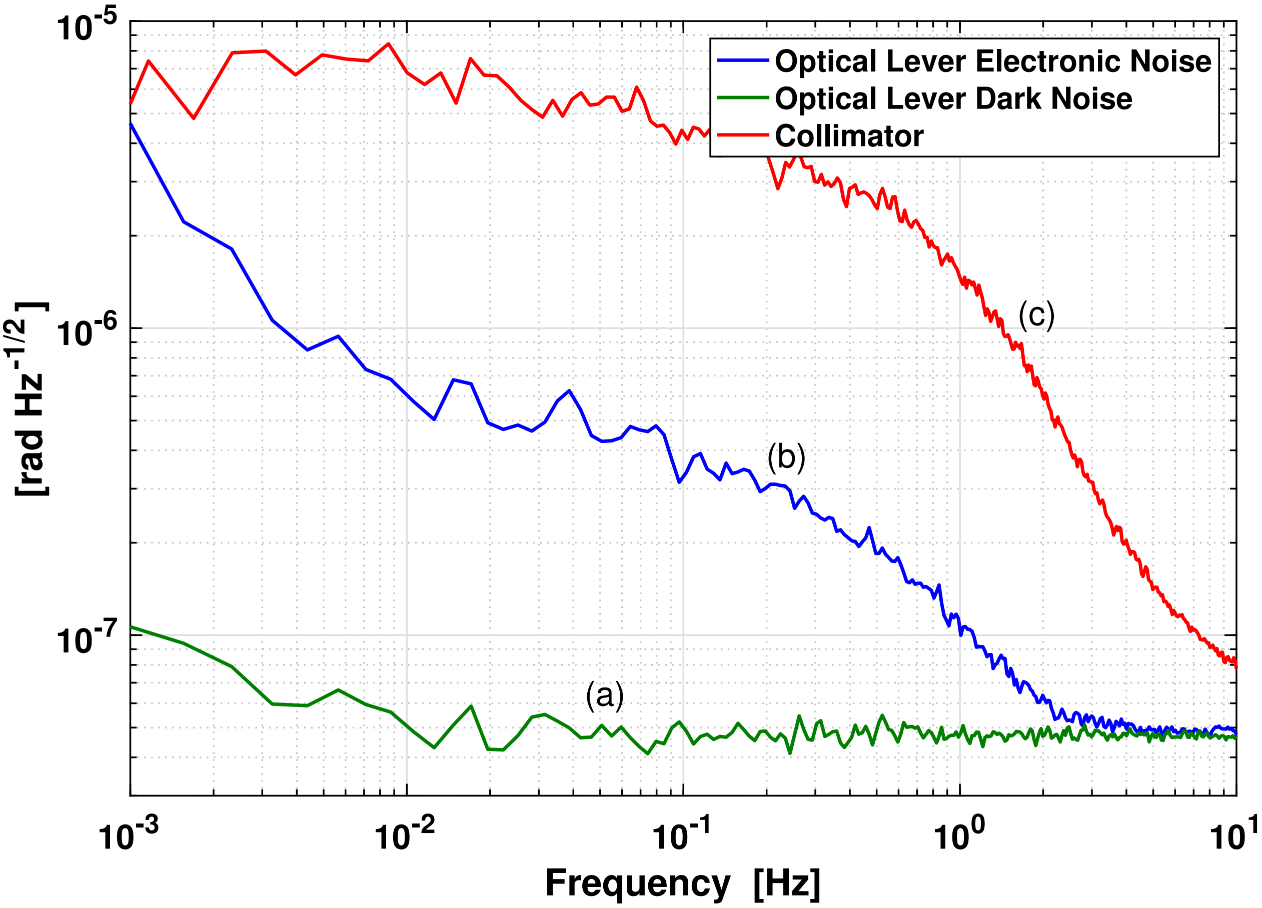

Figure 3.11: Electronic dark noise of the optical lever and steady-state performances of autocollimator and optical lever measurements. Trace (a) shows the electronic dark noise of the optical lever system. The steady-state performance of the optical lever and the autocollimator is shown in traces (b) and (c).

50 nrad/$\sqrt{\text{Hz}}$, which, for the given setup, sets a lower limit to the achievable sensitivity level. Trace (b) is the noise performance with all four optical levers active but without any intentional movement of the hexapod (only one QPD trace is shown in the plot for clarity), and trace (c) shows the equivalent measurement done with the autocollimator. These steady-state sensitivities are about 3.3×10^{-7} rad/$\sqrt{\text{Hz}}$ at 100 mHz for the optical lever and 4.2×10^{-6} rad/$\sqrt{\text{Hz}}$ for the autocollimator, respectively. In the frequency band from 10 mHz to approximately 2 Hz, the minimum resolvable rotational motion obtained with the optical lever system is about one order of magnitude below the autocollimator sensitivity.

Considering the Eq. 3.2, the same analysis as for trace (a) and (b) was performed for the translational degrees of freedom, which yielded a steady state sensitivity of approximately 200 nm/$\sqrt{\text{Hz}}$ at 100 mHz with the electronic dark noise limit at the level of approximately 20 nm/$\sqrt{\text{Hz}}$ (plot not shown). To estimate and

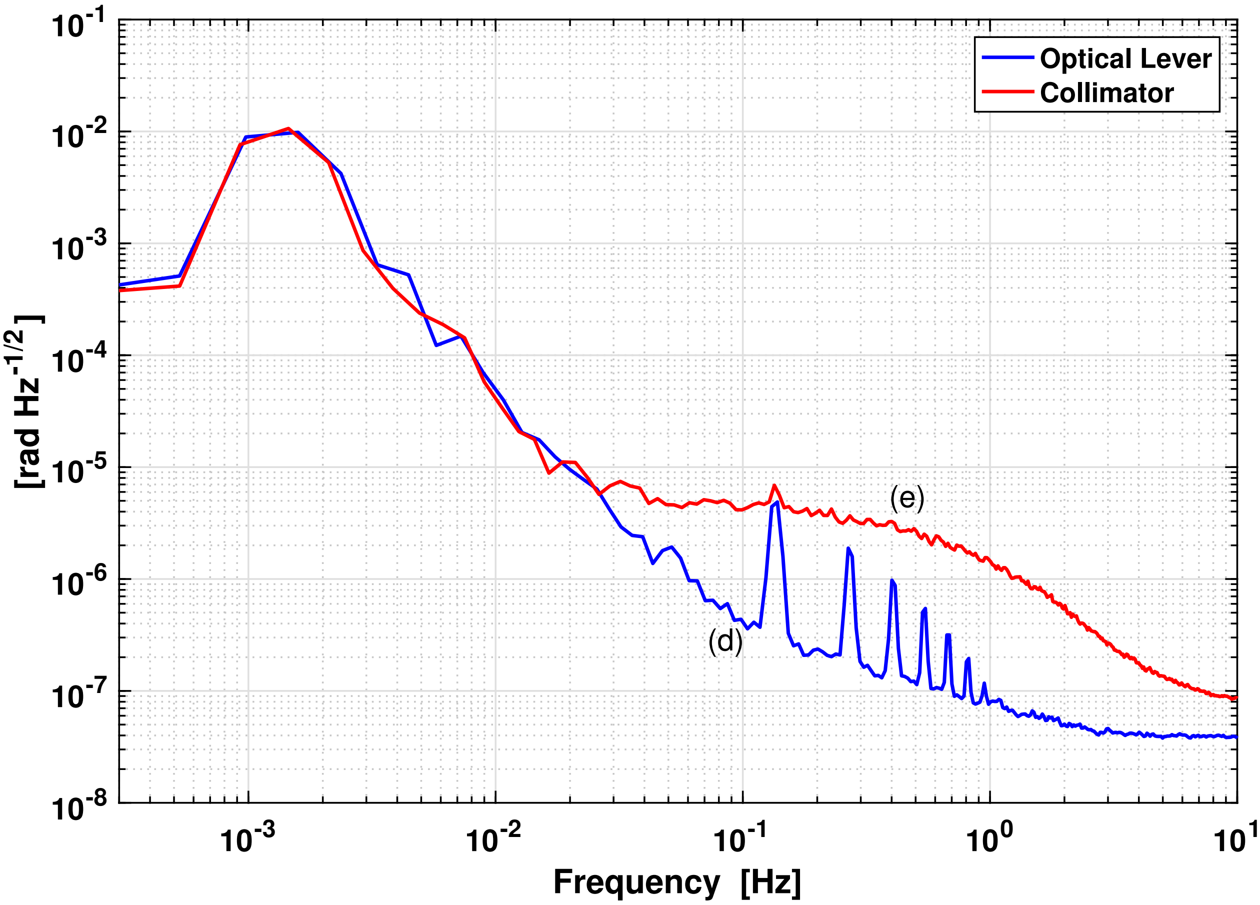

Figure 3.12: Measured angular noise of the optical lever and autocollimator for continuous rotation of the TM around the vertical symmetry axis. The comparison between the optical lever and autocollimator angular signal derived from five cycles of a sinusoidal motion with an amplitude of ±0.5 mrad and period of ~ 12.6min.

compare the two independent measurement methods, the same rotational hexapod motion was used for the time series presented in Fig. 3.9. The noise performances obtained with this sinusoidal motion are shown in Fig. 3.12. Both the optical lever and the autocollimator measurements plotted in traces (d) and (e) yield the same signal signature correctly, recovering the driving frequency of 1.3 mHz. However, at frequencies above approximately 60 mHz, the lower noise floor of the optical lever system allows for a significantly better performance than the autocollimator. This even enables the recovery of the harmonic peaks due to the discontinuous nature of the hexapod motion.

The entire setup had neither seismic nor acoustic isolation, and the tests were performed without considering beam jitters, current noise, and other external noise sources such as mechanical vibrations, air currents, or temperature variations causing thermal drifts. Although the next iteration of this optical sensor will add an extra degree of freedom (with the 6-DoF TM readout, described in section 7.1), the performance of the optical lever is still far from meeting the LISA requirement of $1\,\mathrm{pm}/\sqrt{\mathrm{Hz}}$ at mHz range using laser interferometry. This topic, among others, will be discussed in the next part of this thesis.

Part III

Compact Interferometers

Chapter 4

Laser interferometry for space applications

4.1 Introduction

In chapter 3, it was seen the five-DoFs optical lever readout system reached a steady state sensitivity of approximately 200 nm/$\sqrt{\text{Hz}}$ at 100 mHz for the translational degrees of freedom, which is quite far of the 1 pm/$\sqrt{\text{Hz}}$ requirement at low frequencies that LISA or other gravitational space missions aim. While the use of optical levers for space applications must be discarded due to the low resolution at low frequencies, laser interferometry is the technique of choice for precise monitoring of relative displacements and tilts in space-based and ground-based gravitational wave detectors [9, 74, 75], gravimetric space mission for geodesy [25, 29] and tests of fundamental physics [76].

One of the main limiting factors for the sensitivity of laser interferometers is laser frequency noise coupling into path length noise according to:

$$\delta l = \frac{\delta f}{f_0} \Delta L, \tag{4.1}$$

where ΔL is the optical path length difference of the interferometer, f_0 is the average frequency and δl and δf are the path length noise and frequency noise respectively. The LISA mission design imposes very tight requirements on the frequency stability of the laser sources employed in the spacecraft due to the picometer-noise requirement on the estimate of the relative displacement of its 2.5 million kilometers long arms. The use of Time Delay Interferometry [77] relaxes the frequency stability requirements that are eventually set to [78]:

$$\tilde{\nu} = 300 \, \frac{\mathrm{Hz}}{\sqrt{\mathrm{Hz}}} \, u(f) \tag{4.2}$$

where $u(f)$ is the noise shape function given by:

$$u(f) = \sqrt{1 + \left(\frac{3\,\mathrm{mHz}}{f}\right)^4} \tag{4.3}$$

which is used frequently to scale the sensitivity requirements for inertial sensing of freely floating test masses in space. It describes a mixture of *white noise* with a flat power spectrum at frequencies larger than 3 mHz, and *random run* noise with f^{-4} power spectrum at lower frequencies, where it is expected that the acceleration noise of the test mass becomes dominant.

In ground-based gravitational wave detectors, such as LIGO and VIRGO, homodyne interferometry provides the readout of the relative displacement of test mass mirrors. While in ground-based interferometers, phase locking techniques are employed to stabilize the optical path length difference of the interferometer to fractions of a wavelength, this cannot be done in a space-based gravitational wave detector. The relative position of the three spacecraft in the LISA mission is affected by external gravity gradients, leading to relative motion between the three spacecraft and consequent Doppler shift of the laser beam frequencies exchanged between them. Hence, using homodyne interferometry for space missions is not an option, and space-based detectors employ heterodyne interferometry to measure the distance between free-floating test masses over a long baseline.

4.1.1 Heterodyne interferometry

In heterodyne interferometers, electric fields due to the frequency shift between two interfering beams are represented by the relations

$$E_1(t) = a_1 \cos(\omega_1 t + \varphi_1) \tag{4.4}$$

$$E_2(t) = a_2 \cos(\omega_2 t + \varphi_2), \tag{4.5}$$

where a_1 and a_2 are the amplitudes, ω_1 and ω_2 are the angular frequencies, and φ_1 and φ_2 are the phases of the two waves. The spatial superposition of two light beams is given by $E_{tot}(t) = E_1(t) + E_2(t)$ and the intensity $I(t)$ measured by the photodiode is proportional to:

$$\begin{aligned} I(t) &= [E_1(t) + E_2(t)]^2 \\ &= E_1^2 + E_2^2 + 2E_1E_2 \\ &= a_1^2 \cos^2(\omega_1 t + \varphi_1) + a_2^2 \cos^2(\omega_2 t + \varphi_2) \\ &+ 2a_1a_2 \cos(\omega_1 t + \varphi_1) \cos(\omega_2 t + \varphi_2). \end{aligned} \tag{4.6}$$

Using the following identities $\cos^2 x = \frac{1}{2}(1 + \cos(2x))$ and $2\cos\alpha\cos\beta = \cos(\alpha + \beta) + \cos(\alpha - \beta)$ for the last two terms, Eq. 4.6 leads to

$$\begin{aligned} I(t) = &\frac{a_1^2}{2}[1 + \cos(2\omega_1 t + 2\varphi_1)] + \frac{a_2^2}{2}[1 + \cos(2\omega_2 t + 2\varphi_2)] \\ &+ a_1a_2[\cos((\omega_1 + \omega_2)t + (\varphi_1 + \varphi_2))] \\ &+ a_1a_2[\cos((\omega_1 - \omega_2)t + (\varphi_1 - \varphi_2))] \\ &= \frac{a_1^2}{2} + \frac{a_2^2}{2} + \frac{1}{2}[a_1^2 \cos(2\omega_1 t + 2\varphi_1) + a_2^2 \cos(2\omega_2 t + 2\varphi_2)] \\ &+ a_1a_2[\cos((\omega_1 + \omega_2)t + (\varphi_1 + \varphi_2))] \\ &+ a_1a_2[\cos((\omega_1 - \omega_2)t + (\varphi_1 - \varphi_2))]. \end{aligned} \tag{4.7}$$

Since photodetectors cannot respond to signals at frequencies of $2\omega_1$, $2\omega_2$ and $\omega_1 + \omega_2$, these terms can be neglected and Eq. 4.7 then becomes

$$I(t) = I_1 + I_2 + 2(I_1I_2)^{1/2} \cos[(\omega_1 - \omega_2)t + (\varphi_1 - \varphi_2)], \tag{4.8}$$

where $I_1 = \frac{1}{2}a_1^2$ and $I_2 = \frac{1}{2}a_2^2$. The output from the detector, therefore, contains an AC component at the difference frequency $(\omega_1 - \omega_2)$, whose phase is $(\varphi_1 - \varphi_2)$.

Therefore, it is shown that the intensity in the photodiode varies over time. In contrast, if the frequencies are the same (homodyne case), it can get a constant intensity in the form of:

$$I \propto A_v \left[1 + \cos(\varphi_1 - \varphi_2)\right], \tag{4.9}$$

where A_v is just an amplitude constant. According to Eq. 4.8, the photodiode output power contains the phase information, but also the heterodyne frequency $\omega_1 - \omega_2 = \omega_h$. An IQ-demodulation is used to extract the phase of the beat note, where a trans-impedance amplifier (TIA) converts the photocurrent into a voltage as

$$v(t) = A_v \left[\cos\left(\omega_h t + \varphi_h(t)\right)\right], \tag{4.10}$$

with the amplitude A_v and $\varphi_h = (\varphi_1 - \varphi_2)$. Eq. 4.10 is similar to Eq. 4.8, and only the AC signal is considered for simplification since the DC part does not contain any phase information. The quadratures for the in-phase component and complex amplitude component can be determined by multiplying the signal with cosine and sine at the desired frequency ω (which is normally ω_h) from which the phase needs to be extracted,

$$\begin{aligned} I &= v(t) \cdot \cos(\omega t) \approx \frac{1}{2} A_v \cos(\varphi_h(t)), \\ Q &= v(t) \cdot \sin(\omega t) \approx \frac{1}{2} A_v \sin(\varphi_h(t)). \end{aligned} \tag{4.11}$$

where a demodulation frequency of $\omega = \omega_h$ and a low-pass filter for frequencies above $2\omega_h$ are assumed. The interference signal amplitude and phase are then recovered by

$$\begin{aligned} A_v &= 2\sqrt{I^2 + Q^2}, \\ \varphi_h(t) &= \arctan\left(\frac{Q}{I}\right). \end{aligned} \tag{4.12}$$

4.2 Compact interferometers

To comply with LISA mission requirements [36], heterodyne interferometry needs to provide sub-picometer test-mass displacement and sub-nanoradian tilt-sensing sensitivities in the frequency range between 0.1 mHz and 1 Hz while operating over a multi-fringe dynamic range. LISA will not be the only experiment taking advantage of the outstanding sensitivity of heterodyne interferometry. Other experiments will benefit from the technique, such as torsion balances [79], ground-based gravitational waves detectors like LIGO [80] or ultralow-mass bosonic dark matter searches [81]. However, the accessibility and usability of such interferometric sensors are restricted by their optical complexity. The necessity for a detailed design, the creation of highly stable optical benches with numerous components, and multiple fiber connections significantly complicate their application. These complexities increase the instrument's size, weight, construction effort, and production time, significantly limiting its current deployment range. Therefore, alternative interferometer techniques with simpler or more compact designs and fewer components may offer a wider range of use.

Compact interferometers have to provide operation across a broad range of frequencies while maintaining high resolution. This level of performance is necessary to successfully perform frequency stabilization in large-scale instruments such as future space-based gravitational missions (although, in this case, laser frequency noise is typically controlled using optical cavities). A compact optical design is always the aim in space-based interferometers where the optical setup monitoring several degrees of freedom of the free-floating test masses has to be equipped in a spacecraft. For this reason, in recent years, it sparked the interest in researching for alternative interferometric techniques to minimize the complexity of the optical setup. One of the pioneer techniques aiming for this goal is Deep Phase Modulation (DPM) interferometry [82]. In DPM, a strong sinusoidal phase-modulated beam is injected in an unequal arm-length interferometer, creating a beat note comb with an amplitude exceeding one interference fringe. The interferometric phase is extracted by calculating the I-Q demodulation amplitudes of the digitized readout voltage time series at integer multiples of the modulation frequency and applying a non-linear fit algorithm on this set of coefficients. This significantly streamlines the intricate light preparation methods used in instances like LISA Pathfinder to produce AC readout signals within the kHz range. Digitally enhanced interferometry [83] is another scheme that combines multiple optical signals via a single path for optical and analog detection, paving the way for entirely new interferometer configurations. Applying phase-modulated pseudo-random noise (PRN)

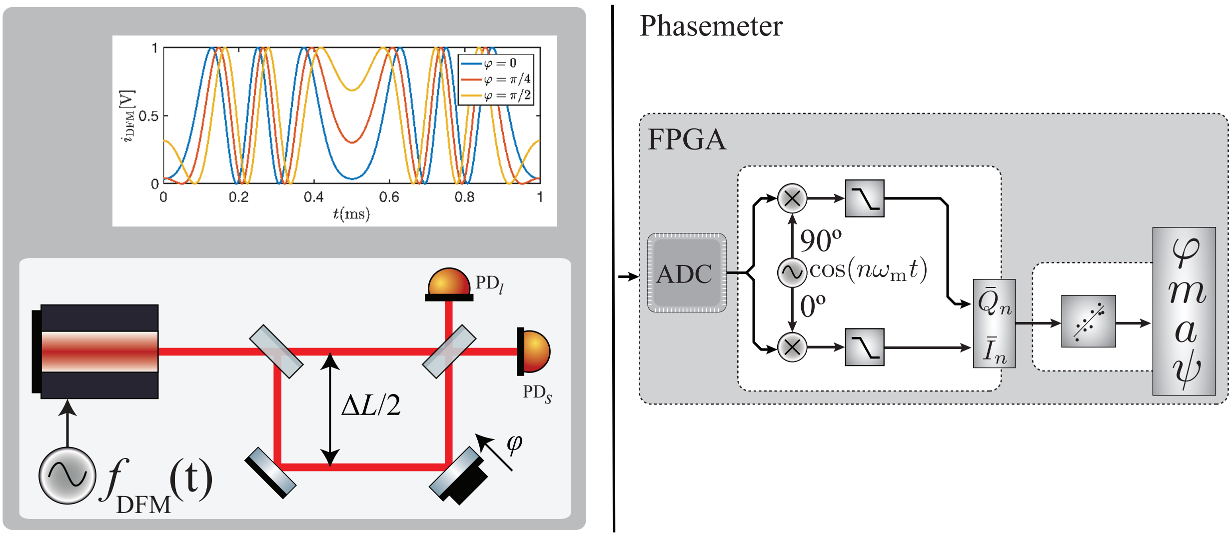

Figure 4.1: Left: Scheme of a DFMI optical setup combining a frequency-modulated laser source and an unequal arm-length interferometer, along an example DFM interferogram. Right: Scheme of the DFM readout implemented in an FPGA: the digitized and buffered voltage time series is digitally demodulated and low pass filtered; the I-Q demodulation coefficients for the first n harmonics of the modulation frequency are fed into a non-linear fit algorithm that provides an estimate of four fit parameters linked to the physical observables of interest in the system. Credits: O. Gerberding

codes onto the laser light makes this possible. The minimum delay and the difference in arm length between two distinguishable signals are determined by the PRN chip rate, leading to performance levels in the order of $10\,\mathrm{pm}/\sqrt{\mathrm{Hz}}$ at low frequencies [84].

The following Section will focus on the Deep Frequency Modulation Interferometry technique (DFMI) [85, 86]. In contrast to traditional heterodyne systems or homodyne quadrature interferometry, DFMI needs fewer optical elements. This requirement facilitates the creation of more compact configurations operating over a multi-fringe range. The functionality of DFM is already demonstrated, showing a displacement-sensing performance on the $1\,\mathrm{pm}/\sqrt{\mathrm{Hz}}$ at Hz level [87] being an attractive alternative to heterodyne interferometry. References [88] and [85] present a detailed outline of the DFMI framework, which is summarized in Sec.4.3.

4.3 Deep Frequency Modulation Interferometry

DFMI aims at minimizing the complexity of the experimental system by imposing only two requirements on the optical setup: the laser source must be frequency tunable, and the frequency-modulated beam has to be injected in an unequal arm-length interferometer to convert frequency modulation into phase modulation (just like DPM) at the output port, as shown in Fig. 4.1. The laser frequency is sinusoidally modulated according to the equation:

$$f_{\text{DFM}}(t) = \Delta f \cdot \cos(2\pi f_{\text{m}} t + \psi_{\text{m}}), \tag{4.13}$$

where f_0 is the average laser frequency, Δf is the amplitude of frequency modulation, f_{m} and ψ_{m} the modulation frequency and modulation phase respectively. The two beams traveling along the short and long arm of the unequal arm-length interferometer are interfered at the output beam splitter and directed towards the readout photodiode. The electric field that reaches the photodiode from the short arm can be expressed in the plane wave approximation as

$$E_s = \frac{1}{2} E_{\text{in}} \sin\left(\omega_0 t + \frac{\Delta f}{f_m} \sin\left[\omega_m t + \psi_m\right] + C\right), \tag{4.14}$$

where $\omega_0 = 2\pi f_0$ and C is the constant phase therm. On the other hand, the electric field that reaches the photodiode from the long arm PD$_l$ (which is delayed by $\tau = \Delta L/c$, where c is the speed of light) is given by

$$E_l = \frac{1}{2} E_{\text{in}} \sin\left(\omega_0 (t-\tau) + \frac{\Delta f}{f_m} \sin\left[\omega_m (t-\tau) + \psi_m\right] + C - \varphi\right) \tag{4.15}$$

where the phase signal φ is the signal of interest, proportional to relative variations of the optical path length difference in the interferometer. Using Eq. 4.6, the effective optical power $P_{\text{out}} \propto (E_s + E_l)^2$ is given by

$$P_{\text{out}} = \frac{P_{\text{in}}}{2} + \frac{P_{\text{in}}}{2} \cos\left(\omega_0 \tau + \varphi + \frac{\Delta f}{f_m} \left(\sin\left[\omega_m t + \psi_m\right] - \sin\left[\omega_m (t-\tau) + \psi_m\right]\right)\right) \tag{4.16}$$

where $P_{\text{in}} \propto E_{\text{in}}^2$ is the input power and terms of the order $2\omega_0$ has been neglected. Eq. 4.16 contains a phase offset $\omega_0 \tau$, which can be neglected in the following expressions and the phase signal φ. Using trigonometric identities, Eq. 4.16 can be expanded as

$$P_{\text{out}} = \frac{P_{\text{in}}}{2} + \frac{P_{\text{in}}}{2}\cos\biggl(\omega_0\tau + \varphi + \frac{\Delta f}{f_m}\left(\sin\left[\omega_m t + \psi_m\right]\right. \\ \left. - \sin\left[\omega_m t + \psi_m\right]\cos\left[\omega_m t + \psi_m\right]\sin[\omega_m\tau]\right)\biggr) \tag{4.17}$$

Assuming that $\omega_m\tau \ll 1$, the output power can be simplified to

$$P_{\text{out}} = \frac{P_{\text{in}}}{2} + \frac{P_{\text{in}}}{2}\cos\left(\varphi + m\cos[\omega_m t + \psi_m]\right), \tag{4.18}$$

where $m = 2\pi\Delta f\tau$ is the modulation depth, which linearly depends on the arm length delay τ and the frequency modulation amplitude Δf. This allows the demodulation of the signal by applying the deep phase modulation (DPM) readout algorithm written by Gerhard Heinzel, which uses the complex signal amplitudes determined by multiple single-bin Fourier transforms. The DPM fit algorithm is also applicable to DFM [86] and was successfully demonstrated for effective modulation depths on the order of $m \approx 9$ [82]. The photocurrent output, given by Eq. 4.18, is converted into voltage via TIA, which provides the output signal $v(t)$ of a phase-modulated self-homodyning interferometer,

$$v(t) = A\left[1 + \kappa\cos\left(\varphi + m\cos\left(\omega_m t + \psi_m\right)\right)\right], \tag{4.19}$$

where A is the signal amplitude that combines constant factors such as optical power and the photodiode efficiency, and κ is the contrast.

Fig. 4.2 shows how a signal given by Eq. 4.19 looks in the time and the frequency domain for different phase offsets φ. Using a Bessel function approach, Eq. 4.19 is expanded into its higher components

$$\begin{aligned} v(t) &= A\left[1 + \kappa J_0(m)\cos(\varphi)\right] + \sum_{n=1}^{N=\infty} a_n(m,\varphi)\cos\left(n\left[\omega_m t + \psi_m\right]\right) \\ &= v_{\text{DC}}(\varphi) + v_{\text{AC}}\left(n, m, \varphi, \omega_m, \psi_m\right) \end{aligned} \tag{4.20}$$

where

$$a_n(m,\varphi) = CJ_n(m)\cos\left(\varphi + n\frac{\pi}{2}\right), \tag{4.21}$$

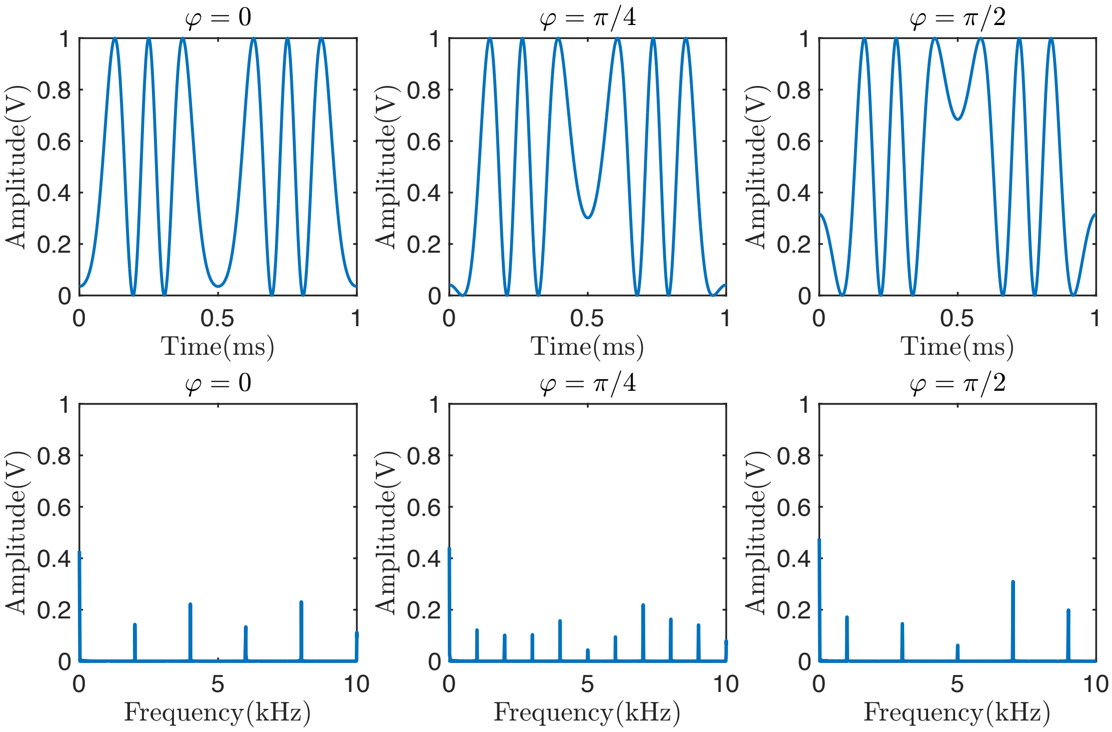

Figure 4.2: DFM signals in the time and the frequency domain for different phase offsets φ.

$$v_{\mathrm{DC}}(\varphi) = A\left[1 + \kappa J_0(m)\cos(\varphi)\right]. \tag{4.22}$$

Here, $a_n(m,\varphi)$ is the harmonic amplitude, $J_n(m)$ represents the Bessel functions of the first kind (both shown in Fig. 4.3), and $C = 2\kappa A$ is a common factor. For DFM experiments, using the MZI (see chapter 5) or the SEDI (see chapter 6), modulation depths of the order of $m \geqslant 6$ are typically used if it used $N = 10$ harmonics for solving the four parameters.

4.3.1 Fit algorithm

The voltage signal, $v(t)$, given by Eq. 4.20, is digitized with a sampling rate of $f_s > 2 \cdot 10 \cdot f_m$ and downsampled by the readout system resulting in the division into smaller segments of a specified length N_{buffer}, where each segment is now processed by a Discrete Fourier Transform (DFT) which demodulates with sine and cosine tones at the relevant harmonics of the modulation frequency. Using the $IQ-$demodulation, given by Eq. 4.11, one can be measure the complex amplitudes of the $n-$th harmonic in terms of quadrature, Q_n, and in-phase I_n

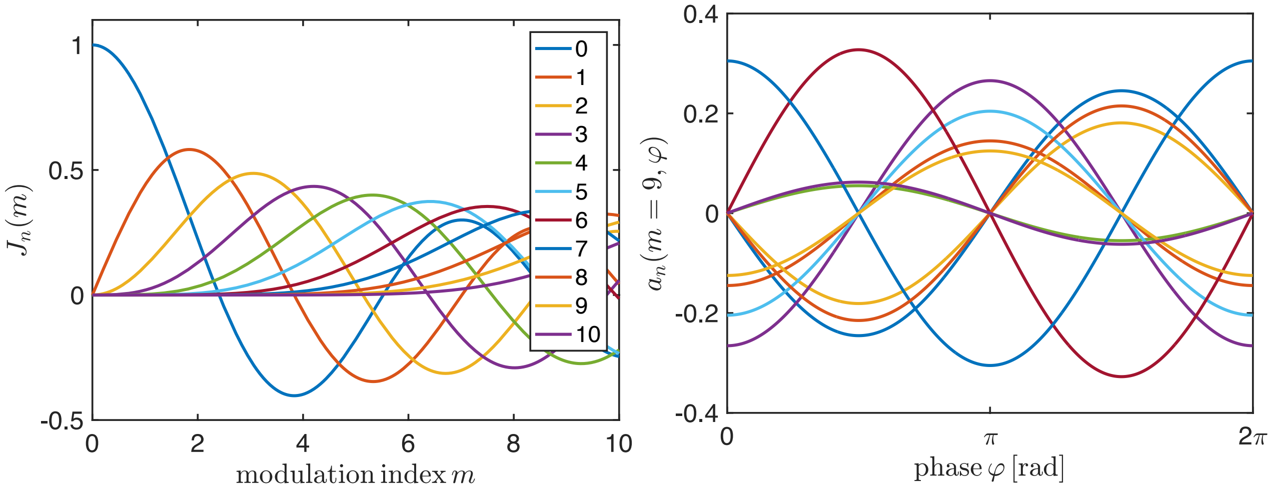

Figure 4.3: (left) Bessel functions and their amplitudes for the first $n = 10$ harmonics. (right) Given a modulation depth of $m = 9$, is plotted the dependency of the harmonic amplitudes, $a_n(m, \varphi)$, with respect to the phase, φ.

$$
\begin{aligned}
Q_n(m,\varphi) &= \cos\left(n\omega_m t\right) \cdot v_{\mathrm{AC}} \approx \frac{1}{2} C J_n(m) \cos\left(\varphi + n\frac{\pi}{2}\right) \cos(n\psi_m) \\
I_n(m,\varphi) &= \sin\left(n\omega_m t\right) \cdot v_{\mathrm{AC}} \approx -\frac{1}{2} C J_n(m) \cos\left(\varphi + n\frac{\pi}{2}\right) \sin(n\psi_m)
\end{aligned}
\tag{4.23}
$$

where the interference signal amplitude and phase are then recovered by Eq. 4.12, leading to

$$
\alpha_n(m,\varphi) = \sqrt{Q_n(m,\varphi)^2 + I_n(m,\varphi)^2}, \tag{4.24}
$$

$$
n\psi_m = \arctan\left(\frac{Q_n(m,\varphi)}{I_n(m,\varphi)}\right), \tag{4.25}
$$

where $\alpha_n(m,\varphi)$ are the measured complex amplitudes. A Levenberg-Marquardt fit algorithm is then used, which solves the set of equations iteratively and minimizes the sum of squares of the measured complex amplitudes (obtained by the demodulation of the measured signal) and the harmonic amplitudes (the analytic solution) according to the least-square expression

$$
\chi^2(\varphi, m, \psi, C) = \sum_{n=1}^{N} \left(a_n(m,\varphi) - \alpha_n(m,\varphi)\right)^2 \tag{4.26}
$$

which provides a solution for the parameters φ, m, ψ_m and C. Numerical analysis of $\chi^2(\varphi, m, \psi, C)$ has shown that considering $N \geq 10$ harmonics for a modulation depth of $m = 9$ or bigger, as is in the case of the MZI or SEDI, leads to the best resolution for the interferometric phase φ [85].

Novel fitting algorithms are currently tested at the Albert Einstein Institute with the aim of minimizing the computational load of the DFM readout while preserving the parameter estimate precision. The main candidates to replace the Levenberg-Marquardt algorithm are Kalman filtering and particle swarm optimization. Nevertheless, the review of these novel algorithms is out of the scope of this thesis.

Chapter 5

Mach-Zehnder reference interferometer upgrade

5.1 Introduction

As seen in the previous chapter, test mass readout in future satellite missions like LISA or ground-based experiments for gravitational wave detection and geodesy requires that the sensitivity of the optical phase measurement shows displacement sensitivities in the interferometer on the order of 1 $\mathrm{pm}/\sqrt{\mathrm{Hz}}$ at low frequencies. In an optimal scenario, such quasi-monolithic interferometers in stray light optimized setups in a vacuum, with higher thermal stability, possess the potential to detect all degrees of freedom of a test mass while maintaining a minimal level of complexity and would enable LISA-like performance levels. Using DFM to simplify optical setups is an option; nevertheless, DFM implementation needs the use of interferometers with unequal arm lengths. This chapter describes the design of a classic unequal arm compact interferometer, the Mach-Zehnder reference interferometer (MZI), which will later be used as a frequency reference for DFM experiments.

The original design and construction of the MZI are described in [89], and especially in [88], where it is shown the results of optical simulations during the construction of the MZI; however, a summary is given here. The MZI consists of a baseplate made of CLEARCERAM™ CCX-HS ultra-stable glass ceramic to which fused silica components are attached via UV adhesive bonding. The baseplate material is chosen for its close to zero coefficient of thermal expansion around room temperature (CTE of $(0.0 \pm 0.1) \cdot 10^{-7}/\mathrm{K}$), while fused silica is the material

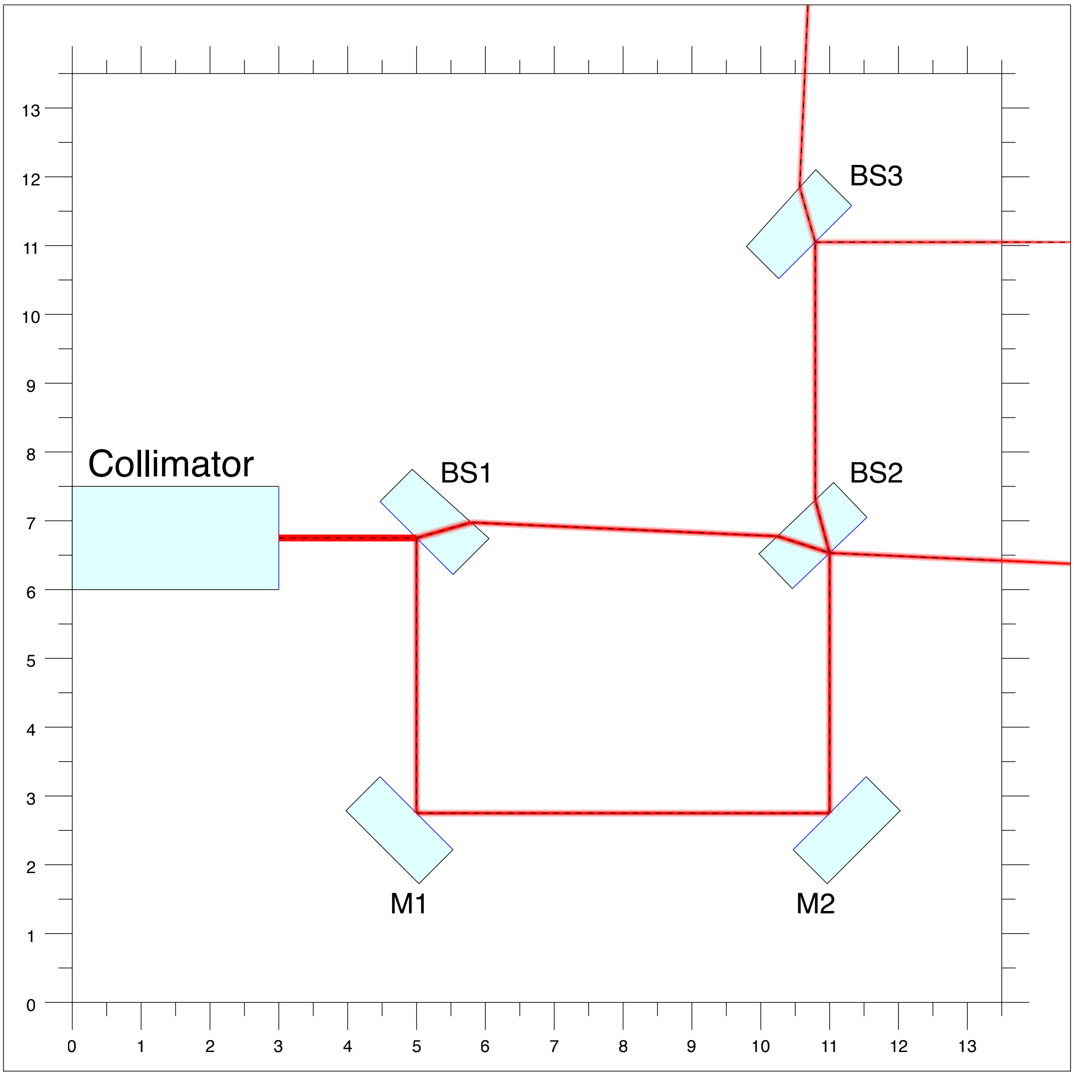

Figure 5.1: 2D drawing of the reference MZI, generated by IfoCAD. The arm length mismatch is ~70 mm. The beam splitters BS1 and BS3 have a wedge angle of 3°. The commercial fiber coupler from Schäfter+Kirchhof beam has a waist size diameter of 2 mm and a waist position of 100 mm after the fiber output coupler. Credits: K. S. Isleif.

of choice for the optical elements due to its excellent transmission properties. The baseplate has dimensions of $13.5 \times 13.5 \times 3.6\,\mathrm{cm}^3$, and the design was aided by the C++ optical modeling library IFOCAD [90]. In [89], an off-the-shelf commercial fiber coupler from Schäfter+Kirchhoff (S+K) mounted in an adjustable three-axis stage from Owis was used to inject laser light into the West port of the input beam splitter (BS1, which serves as splitting beam splitter). The MZI also includes two high-reflective (HR) mirrors, M1 and M2, and another beam splitter, BS2, which is a non-wedged component and is the recombination beam splitter in the interferometer as is shown in Fig. 5.1.

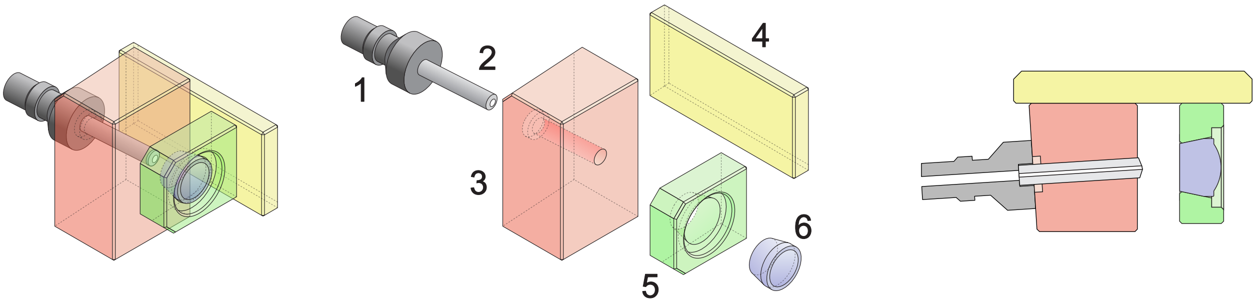

Figure 5.2: The fiber injector optical subassembly (a) consists of a polarization-maintaining 1064 nm single-mode optical fiber (1) equipped with a bare ferrule (2) held in place by a tightly fitted hole in the fused silica fiber mount (3). An off-the-shelf anti-reflectively coated aspherical lens of D-ZLAF52LA glass, modified for a tapered outer surface (6), is UV-glued into a matching hole in the fused silica lens holder (5). Finally, the fiber mount and the lens holder are joined together at the desired distance, position, and orientation using a longitudinal girder of fused silica (4) and two thermally compensating layers of UV adhesive. Credits: D. Penkert.

5.2 Fiber Injector Optical Subassembly - FIOS

To improve the previously reported stability in [89], especially at very long measurement times, a quasi-monolithic fiber injector optical subassembly (FIOS) developed in-house by D. Penkert was used instead of the commercial fiber coupler from S+K. Fig. 5.2 shows the main part of the FIOS, which, in essence, combines a fiber end and a lens into a quasi-monolithic, non-adjustable package, thus significantly reducing the effects of both mechanical and thermal creep in comparison to traditional fiber injectors. As such, a FIOS forms an integral building block for state-of-the-art all-glass optical benches developed not only for space missions [91, 92] but also for high-precision interferometers. For example, to the one presented here, three direct predecessors FIOS have been retrofitted onto AEI's Hexagon interferometer, the primary testbed for the LISA phasemeter. Also, eight of the current-generation FIOS have since been deployed on AEI's Three-Backlink Interferometer for the direct comparison of three candidate implementations of LISA's phase reference distribution system (PRDS) [93].

FIOS requires light to be coupled into their fibers, as well the design allows for the simultaneous manipulation of all of the output beam's relevant degrees of freedom (apart from its polarization) in situ on the interferometer's baseplate directly before permanently fixing them via UV adhesive curing as is described in [94]. All of the FIOS parts are pre-manufactured and generic, where a polarization-maintaining 1064nm single-mode optical fiber equipped with a standard yet slightly longer and bare ferrule for common fiber connectors utilizing an eight-degree angled physical contact (FC/APC) is held in place by a tightly fitted hole in the fused

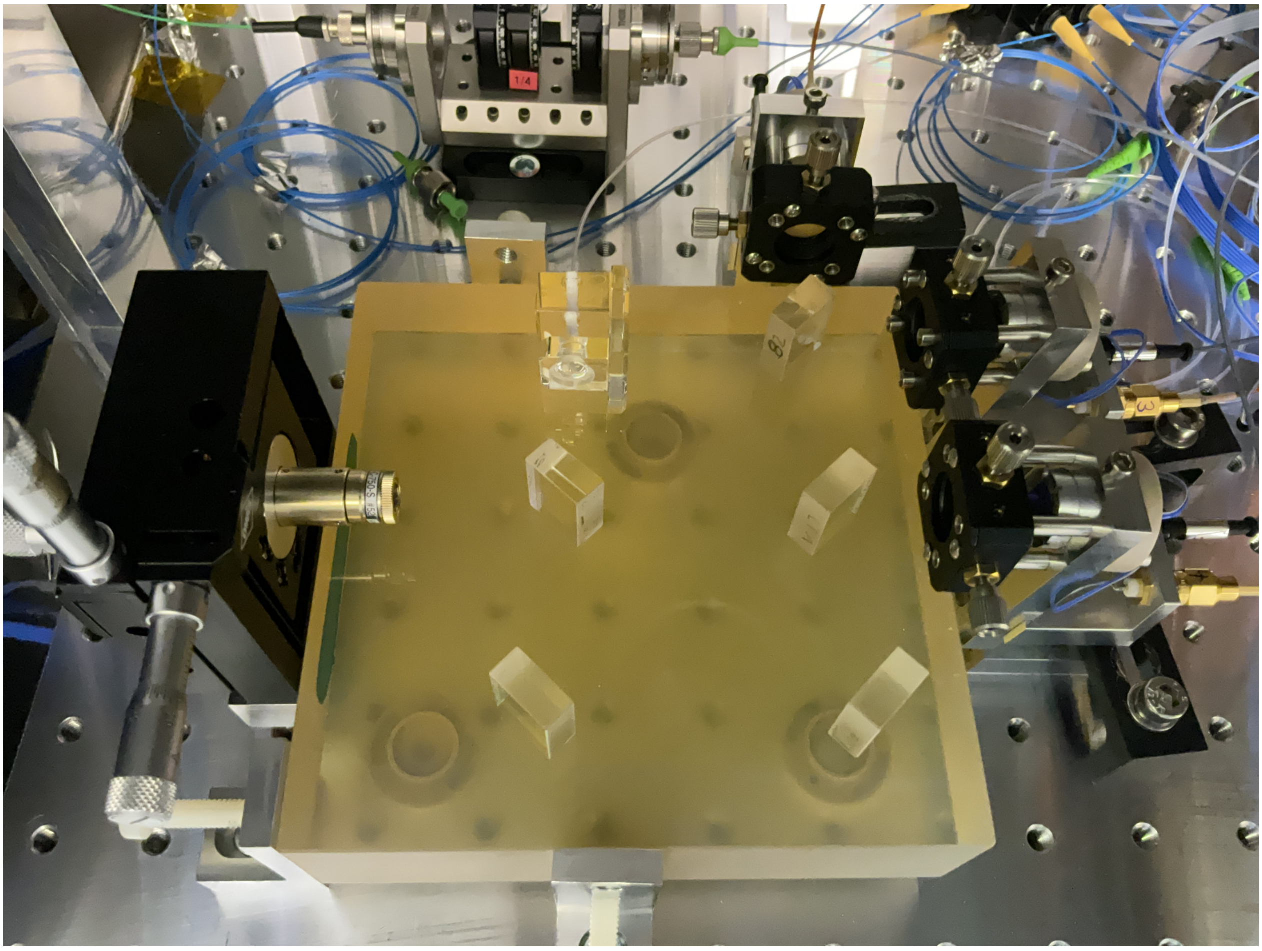

Figure 5.3: Photography of the MZI with the FIOS attached to the previous fiber collimator. FIOS produces a beam with a waist size of 2 mm diameter (same for the S+K collimator). In the photography, it is also observed the photodetectors that will be used for DFM experiments.

silica fiber mount assembly (FMA). An off-the-shelf anti-reflectively coated aspherical lens of D-ZLAF52LA glass, modified for a tapered outer surface, is UV-glued into a matching hole in the fused silica lens holder. Finally, FMA and lens holder are joined together in the desired distance, position, and orientation using a longitudinal girder of fused silica and two thermally compensating layers of UV adhesive.

The unequal arm length MZI has originally been a proof-of-concept for the stability achievable with an all-UV-adhesively bonded optical bench. In order to increase the stability, one of the latest generation FIOS was installed in the MZI, as seen in Fig. 5.3 (firstly, together with the old collimator). Using as a reference the Fig. 5.1, the beam is delivered by the FIOS and retrofitted to the North port of BS1, where it is split into the short and long arms of the MZI. The beam traveling along the long arm is reflected off mirrors M1 and M2 before interfering with

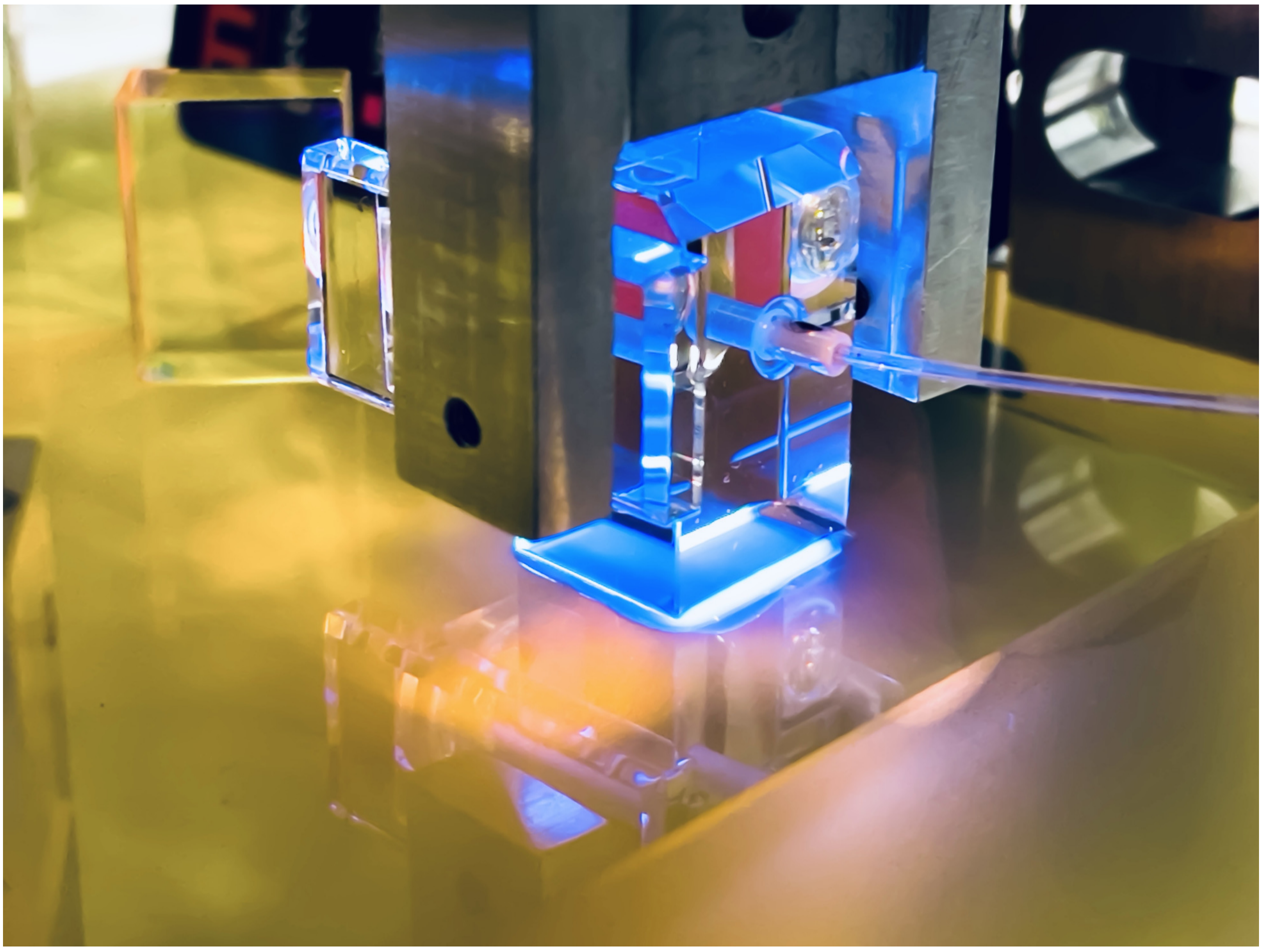

Figure 5.4: Photography of the UV adhesive bonding applied to the FIOS to be attached to the MZI. In the photography, the lower part of the homemade positioning device is observed to align the MZI FIOS. The measured contrast was 94%, and no signs of degradation have been observed during the two-year operational period encompassing several vacuum cycles.

the short arm beam at the recombination beam splitter BS2. A third and fourth beam splitters (BS3 and BS4) are placed in the North and East output ports of the beam combiner to allow performing diagnostic measurements, such as optical zero measurements, while maintaining symmetry between the photodetectors. The precise positioning and orientation of components on the baseplate are optimized via simulations to reduce the impact of spurious beams caused by residual reflections at the secondary surfaces, which have been identified as critical noise sources in high-precision interferometers. The input beam splitter and the beam combiner are wedged to separate the secondary reflections from the main optical path.

The FIOS was first pre-assembled and then installed on the MZI with all other components already fixed to the baseplate. The alignment of the FIOS was done with the help of a homemade positioning device designed by M. Mehmet, as seen in Fig. 5.4, and continuous contrast monitoring by applying a deep frequency modulation to the laser. Using a WinCamD-LCM Beam Profiler, it could be measured the beam waist diameter, which was about 2 mm over a 1 m distance, confirmed a collimated beam in the measurement range. The final contrast achieved was 94%, and no discernible contrast degradation was observed following a two-year operational period encompassing several vacuum cycles, highlighting the satisfactory long-term stability of the UV adhesive bonding.

5.3 Experimental setup for Deep Frequency Modulation experiments

As seen in section 4.3, the first-proof-of-principle experiment of an interferometric set-up using DFM has been described in [88]. The usage of DFM interferometry promises very compact, small, and simple optical setups. Nevertheless, the picometer stability requires not only the use of stable interferometers but also the use of a vacuum environment, which helps reduce the influence of air movement, electrostatic coupling, and slow temperature drifts; also critical for high-precision measurements is the temperature stability of the experiment.

Almost all the components necessary for DFM experiments (including the vacuum tank, photodetectors, and the MZI), were already available from the previous DFM project led by Dr. Katharina-Sophie Isleif. However, some of the components were upgraded to improve the previous measurements, including installing the complete vacuum system and a novel 3-layer thermal shield.

5.3.1 Vacuum system

The complete vacuum system, which is shown in Fig. 5.5, consists of the following components:

- TURBOLAB-350 Table Top
- Oil-free Scroll Pump model Leybold SCROLLVAC-SC-5-D
- Turbomolecular Pump model Leybold TURBOVAC 350i
- Angle Valve model Pfeiffer D-35614
- Ultra-High-Vacuum (UHV) gate valve from VAT

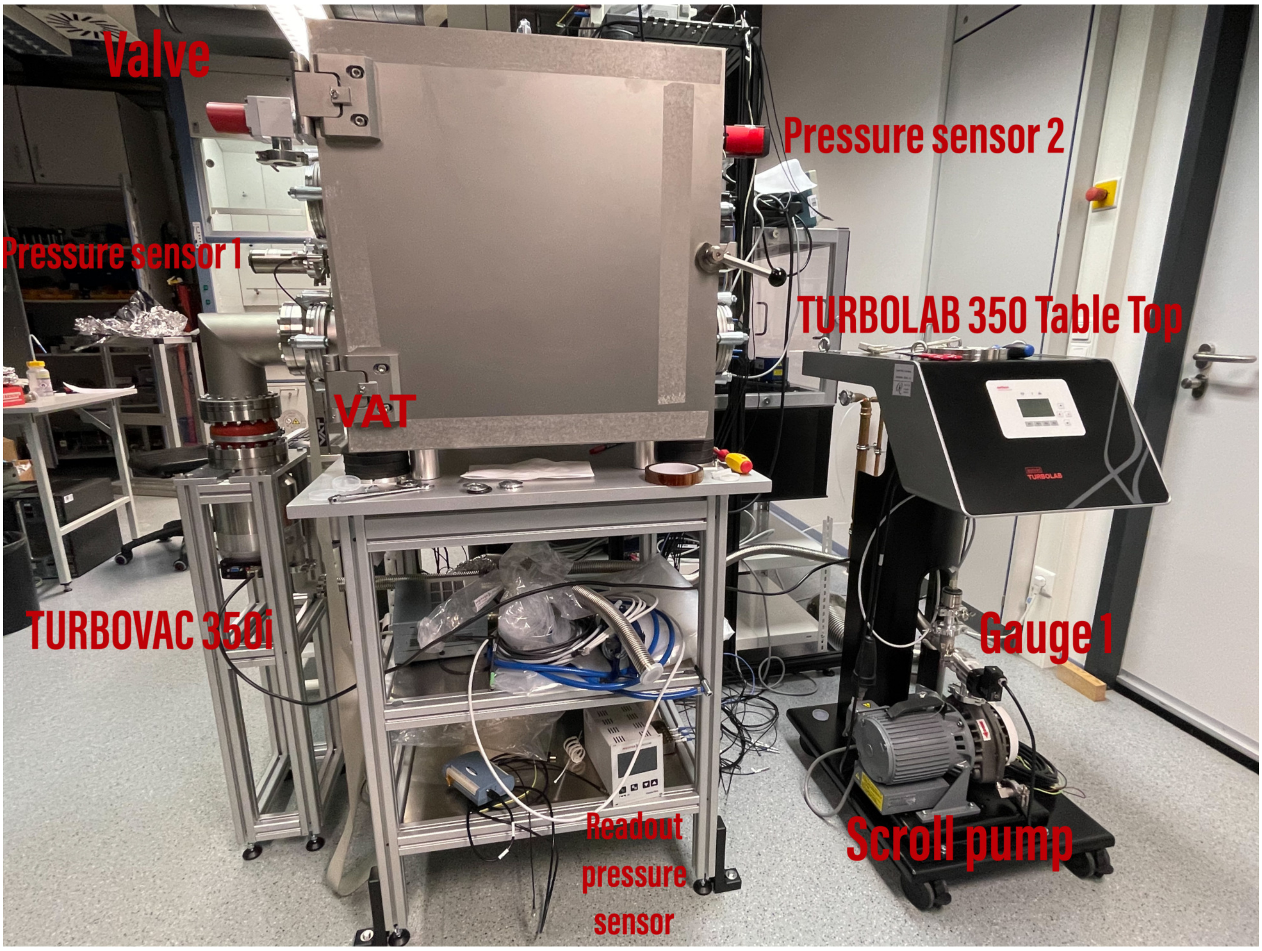

Figure 5.5: Photography of the vacuum system with all the components installed.

- Gauge 1, model Leybold SECUVAC-DN-25
- Pressure sensor 1/Gauge 2, model Leybold PENNINGVAC-PTR-90N (1×10^{-8} mbar - 1000 mbar pressure range)
- Pressure sensor 2, model Pfeiffer PTR 91
- Readout Pressure sensor Pfeiffer model Centre Two

The TURBOVAC-350i was disassembled from the TURBOLAB-350 Table Top and installed to the L-shape tube, as is seen in Fig. 5.6. This L-shaped tube and the TURBOVAC were assembled into the vacuum chamber via the UHV gate valve. The valve is necessary because, during the pumping, undesired vibrations would affect the measurements. For this case, it was included a damper or shock absorber between the pump and the L-shape tube that prevents the vibrations from coming into the chamber when the turbopump is active. Once the ultimate pressure is reached, the pumping system is switched off, and the valve is closed manually immediately. Ideally, that would give hours of a low-pressure environment. However, this amount of time is not enough if it requires overnight measurements. Therefore, in the TURBOVAC 350i configuration, it was set a pressure of 3×10^{-2} mbar as a lower pressure limit, and a pressure of $5{\times}10^{-1}$ mbar as an upper-pressure limit. This maintains the pressure level in the tank in a low-pressure mode during the long overnight measurements. The torque applied to the screws in the L-Shape and in the TURBOVAC was 20 N · m and 15 N · m, respectively.

The TURBOVAC is connected to Gauge 1 and the Scroll Pump using a 3 m Vacuum Hoses with Flanges ISO-KF25. The Tabletop is connected to the network via an RS-232 cable, allowing remote access and control of the pumping system through its IP address. A 24V DC cable also connects the Tabletop to the TURBOVAC, supplying power to its cooling fan. Since the readout system of the TURBOLAB-350 is not good enough (only stores 90 minutes of data), a second pressure sensor, model Pfeiffer PTR-91, was installed in the vacuum chamber and connected via LAN cable to the readout box, model Pfeiffer Centre Two. There, the pressure data can be stored over time using just a USB, which continuously saves the data.

To initiate pumping, the TURBOLAB can be accessed manually or remotely via IP address, with the scroll pump starting upon pressing the 'START' button. The TURBOVAC begins pumping when the pressure reaches 8×10^{-2} mbar, a process that typically takes about 1 hour. In most cases, changes in pressure are attributable to the outgassing of elements inside the vacuum system. To reduce this problem, the components inside the vacuum system (MZI and other optomechanical components) are cleaned to minimize outgassing rates. Also, to reduce temperature fluctuations in the laboratory, the vacuum chamber is covered with ArmaFlex, an elastomeric foam with low thermal conductivity for condensation control. After two weeks of pumping, the vacuum tank's minimum pressure reached about 4×10^{-6} mbar.

5.3.2 Thermal Shields

To minimize temperature fluctuations in the MZI, a lot of effort is put into isolating it from any heat disturbance, particularly environmental thermal noise, which can be coupled to the measurements. The MZI, together with all the optomechanical components like photodetectors, beam splitters, or mirror mounts, are surrounded by a system of three aluminium heat shields inside the vacuum chamber as seen

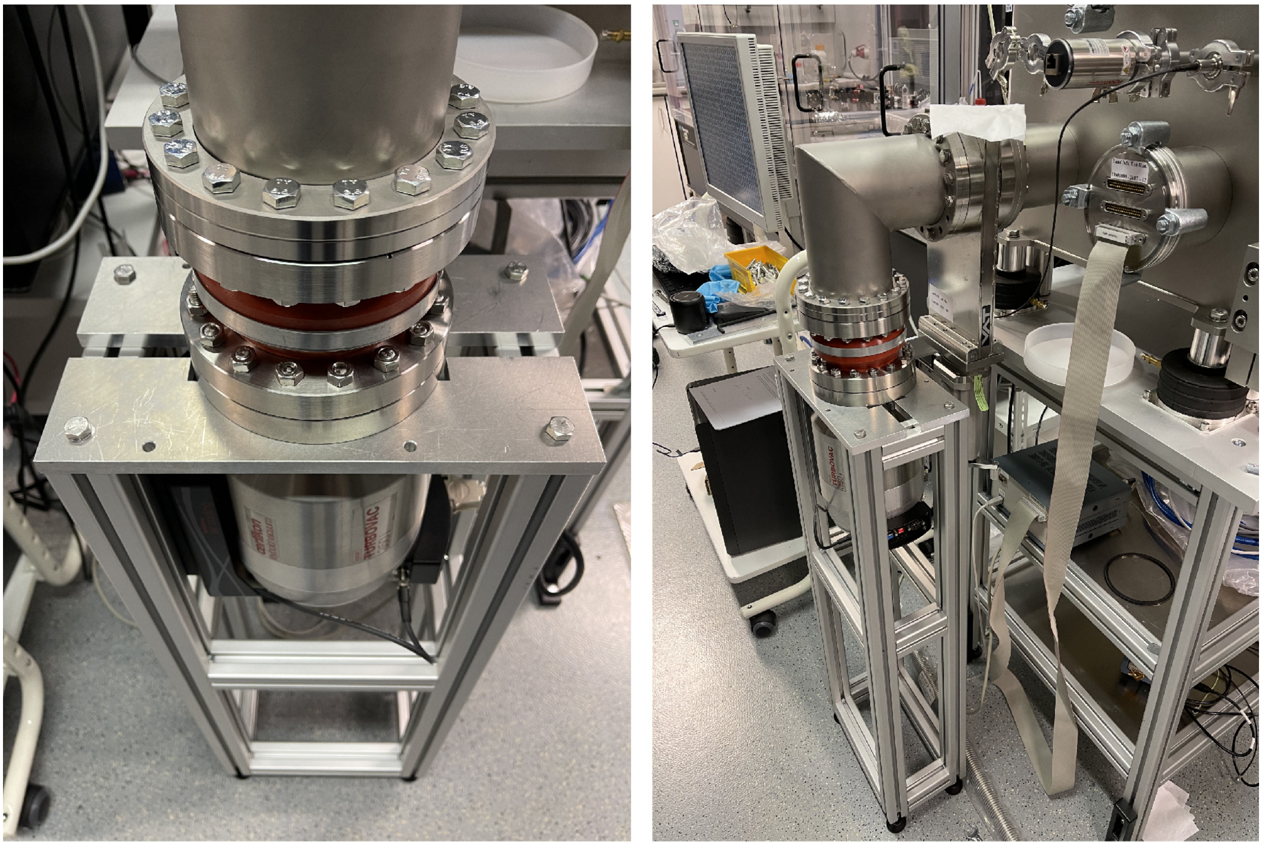

Figure 5.6: Photography of the scroll pump installed into the vacuum tank via an L-shaped tube.

in Fig. 5.7, which reduce significantly the heat transfer with the exterior. In the future, it is planned to actively control the temperature of the external sides of the vacuum chamber with thermal pads so they are always at a temperature setpoint over the ambient temperature and it can absorb the thermal fluctuations.

The in-house mechanical workshop manufactured the shields, and their surfaces were polished (in order to achieve very low thermal emissivity) in handwork with discs of cloth and without chemical components via an external company where they provided a measured roughness average of $0.04\,\mu$m. Each shield consists of six 8 mm plates made of aluminium, joined together by a series of stainless steel M3 screws. The shields are designed so that the side plates have to be fastened to the base plate first, then the end plates, and lastly, the top plate. The full plates can then be easily removed for quick access to the MZI and the rest of the optomechanical components, as seen in Fig. 5.8. The dimensions of the shield plates are listed in Table 5.1.

A circular hole with a diameter of 3 cm is drilled into the lateral sides of the shields so that the fibers and cables that feed the photodetectors and ground the sys-

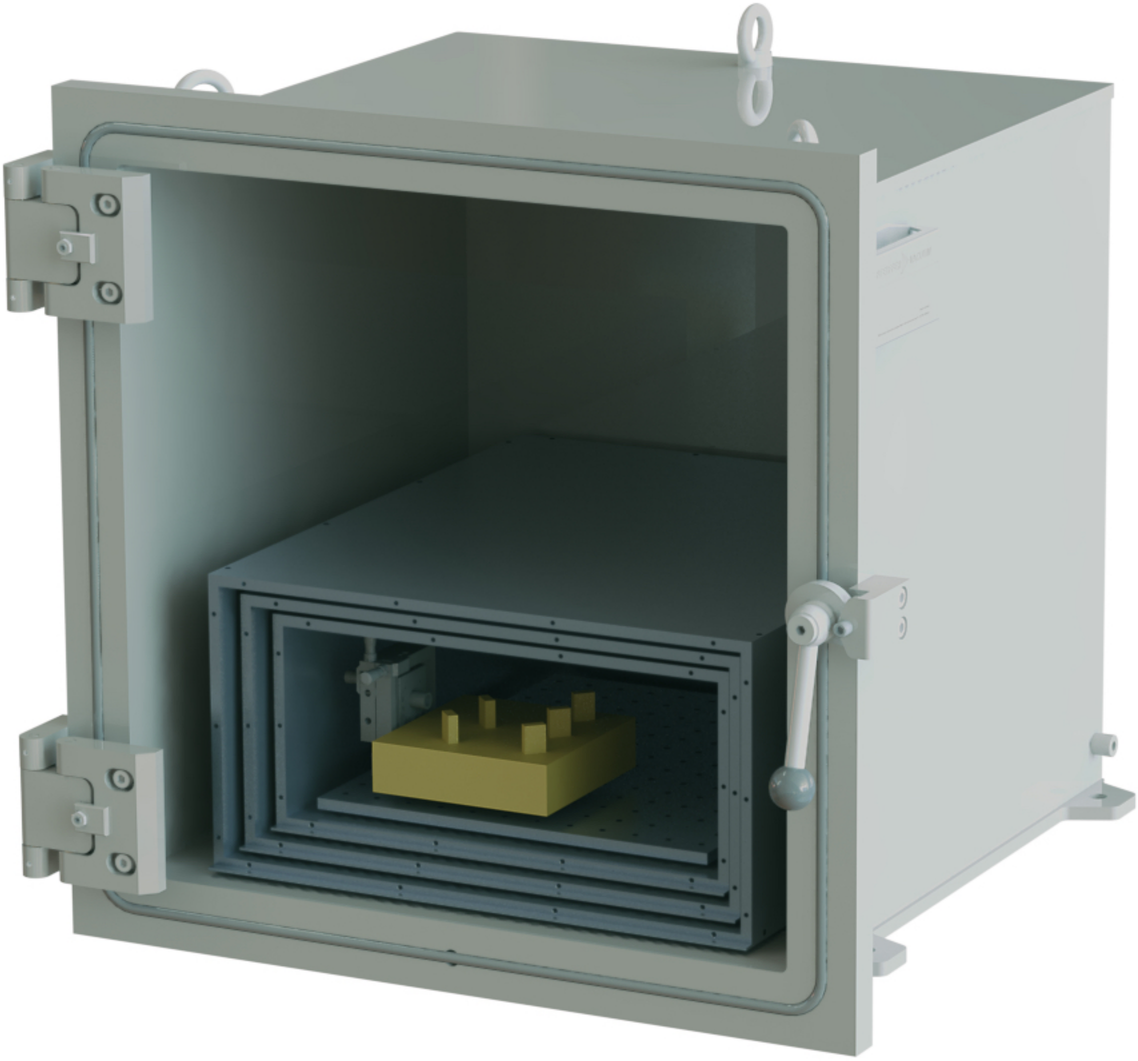

Figure 5.7: 3D view of the aluminium heat shields that surround the MZI (and the rest of optomechanical components) inside the vacuum chamber. The shields, which provide a great amount of passive thermal isolation, are supported by three small PEEK semispheres that rest on conical cuts made to each of the base plates, hence greatly reducing thermal contact between shields and minimizing conductive heat transfer in the system.

tem can enter freely. Each shield is supported by three 10 mm PEEK semispheres that rest on 5 mm deep conical cuts made to each base plate. The mechanical contact between the aluminium and the PEEK semispheres greatly reduces the thermal contact between successive shields, minimizing heat transfer via conduction in the system. All the conical cuts are vented to avoid the generation of pockets of air underneath the PEEK spheres.

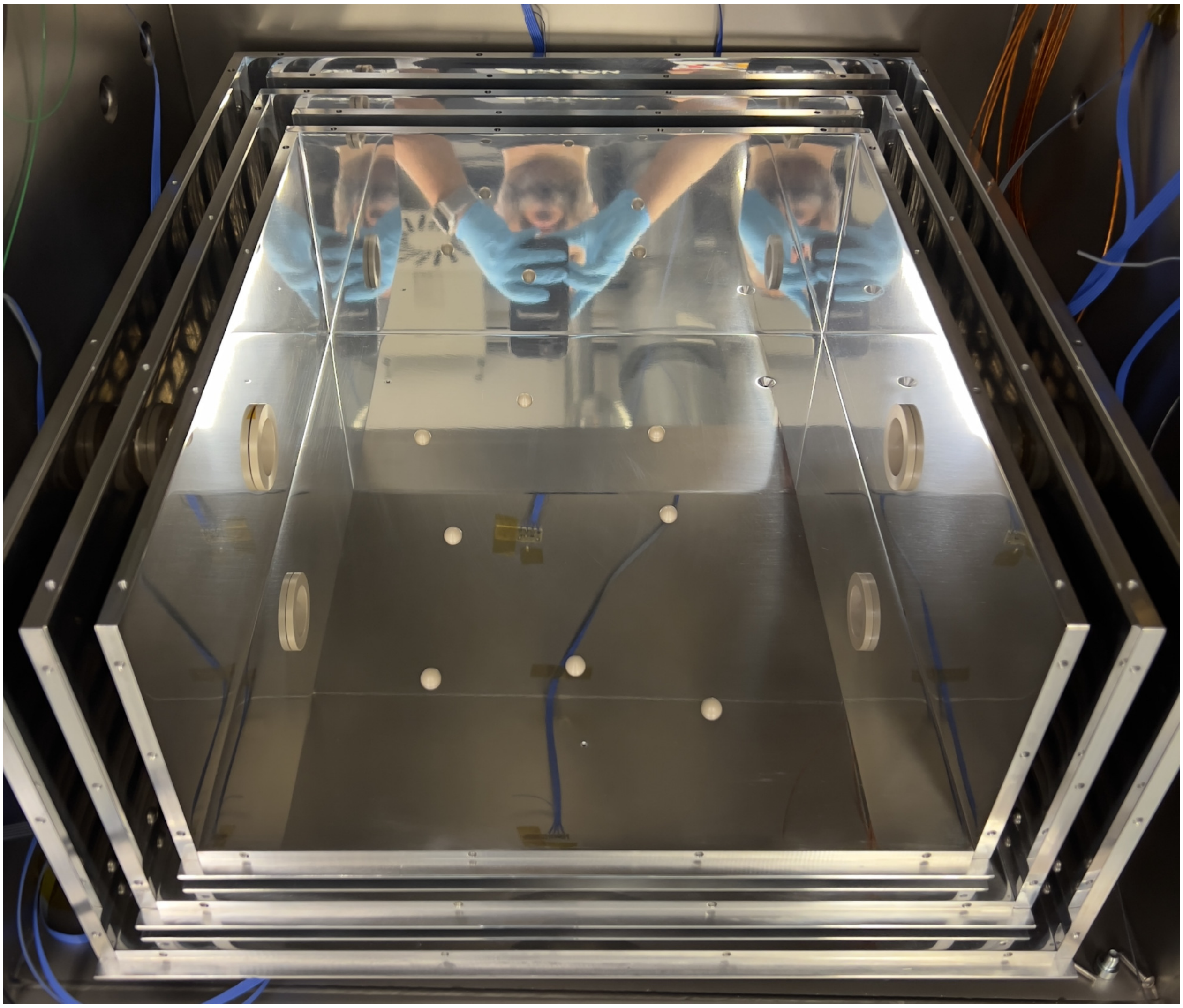

Figure 5.8: Photo of the three heat shields without top plates and with a few PEEK semispheres used as the breadboard support. Note the large specular reflectivity of the aluminium surfaces due to the special polishing technique to bring the surface emissivity down.

	Shield 1	Shield 2	Shield 3
Base-plate	412×472	380×440	348×408
Side-plate	204.43×456	176.28×424	148.14×392
End-plate	204.43×412	176.28×380	148.14×348
Front-plate	212.43×412	184.28×380	156.14×348
Top-plate	412×464	380×432	348×400
Total	$214.43 \times 412 \times 472$	$186.28 \times 380 \times 440$	$158.14 \times 348 \times 408$

Table 5.1: Dimensions in mm of the three aluminium heat shields surrounding the MZI and the optomechanical components. Each plate has a thickness of 8 mm.

5.3.3 Temperature Sensors

Positive Temperature Coefficient (PTC) thermistors (model PT10000) monitor temperature fluctuations throughout the setup. Eight of these sensors are in the vacuum chamber: five are placed on each side of the chamber (except on the chamber door), two are inside the thermal shields, and one is the out-of-loop sensor placed outside the chamber. The PTC operates on the principle that the electrical resistance of the detector's element (in this case, platinum) increases with temperature. The relationship between resistance and temperature is highly linear over small temperature ranges, but a quadratic term is needed to model the behavior accurately over wider ranges.

The Callendar-Van Dusen equation is commonly used to describe the resistance-temperature relationship of the PTC thermistors. The equation is as follows:

$$R_T = R_0 \left(1 + AT + BT^2 + C(T - 100)T^3\right) \quad \text{for} \quad T \leq 0 \tag{5.1}$$

and

$$R_T = R_0 \left(1 + AT + BT^2\right) \quad \text{for} \quad T > 0 \tag{5.2}$$

where:

- R_T is the resistance at temperature T,
- R_0 is the resistance at 0°C (which would be 10 kΩ for a PT10000),
- T is the temperature in °C,
- A, B, and C are coefficients.

The coefficients for a platinum PTC are defined by the ITS-90 International Temperature Scale given by $A = 3.9083 \times 10^{-3}\,°\mathrm{C}^{-1}$, $B = -5.775 \times 10^{-7}\,°\mathrm{C}^{-2}$ and $C = -4.183 \times 10^{-12}\,°\mathrm{C}^{-4}$ for $T \leq 0°$ C only. For the thermal analysis, since the whole experiment is operating at room temperature, only Eq. 4.2 was used.

The resistance of temperature sensors can be measured using an electrical circuit originally designed by Gerhard Heinzel, based on the design of the LISA

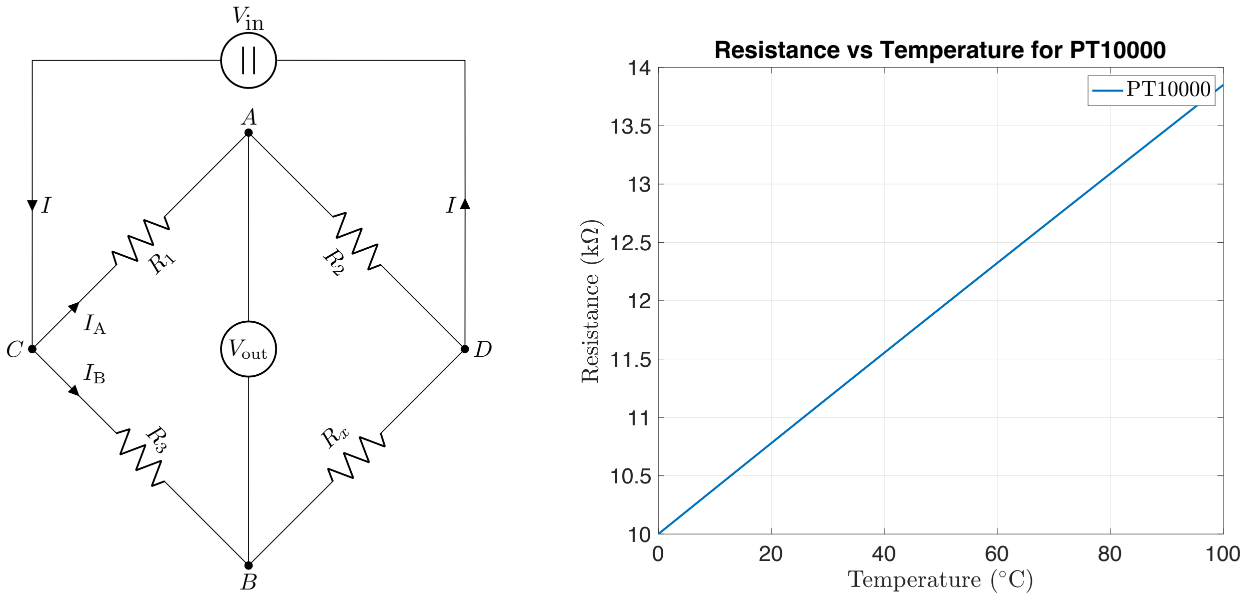

(a) Wheatstone bridge schematic.

(b) Temperature vs resistance for a PT10000 thermistor.

Figure 5.9: (a) Schematic of a Wheatstone bridge. The bridge is balanced when the ratio of resistances $R_1/R_2 = R_3/R_x$, resulting in zero voltage across the voltmeter, being *A*, *B*, *C* and *D* the circuit's nodes. (b) Temperature vs. resistance for a PT10000 thermistor. The data points follow the Callendar-Van Dusen equation, as expected for a platinum PTC.

Technology Package, which uses a Wheatstone bridge circuit. Fig. 5.9a shows a typical Wheatstone bridge consisting of two legs, while the first leg contains two known resistor values, R_1 and R_3, and the other leg includes the unknown component, R_x and the resistor R_2. The unknown electrical resistance can be measured very accurately by balancing the two legs of a Wheatstone bridge circuit. Therefore, an electrical circuit was constructed for each temperature sensor, with the thermistor's resistance being the unknown resistance R_x [95], whereas a voltage source supplied a rectangular signal with a rate of 3Hz.

Implementing a bidirectional voltage application significantly enhances the suppression of common-mode signals in a Wheatstone Bridge configuration. This effect reduces the influence of contact resistances and other noise sources, making the measurements even more precise. Consequently, this leads to observable white noise levels approximately on the order of $10^{-5}\,\text{K}/\sqrt{\text{Hz}}$, further illustrating the effectiveness of this technique in noise reduction and measurement accuracy improvement as seen in Fig. 5.10, where it can be seen the amplitude spectral density (ASD) of the different temperature sensors under operation: sensor in the MZI, top and bottom of the chamber, outside the tank, whereas S_3, S_5, S_6, and S_8 are on the other different sides of the vacuum tank. The ASD can quantify the sensor's

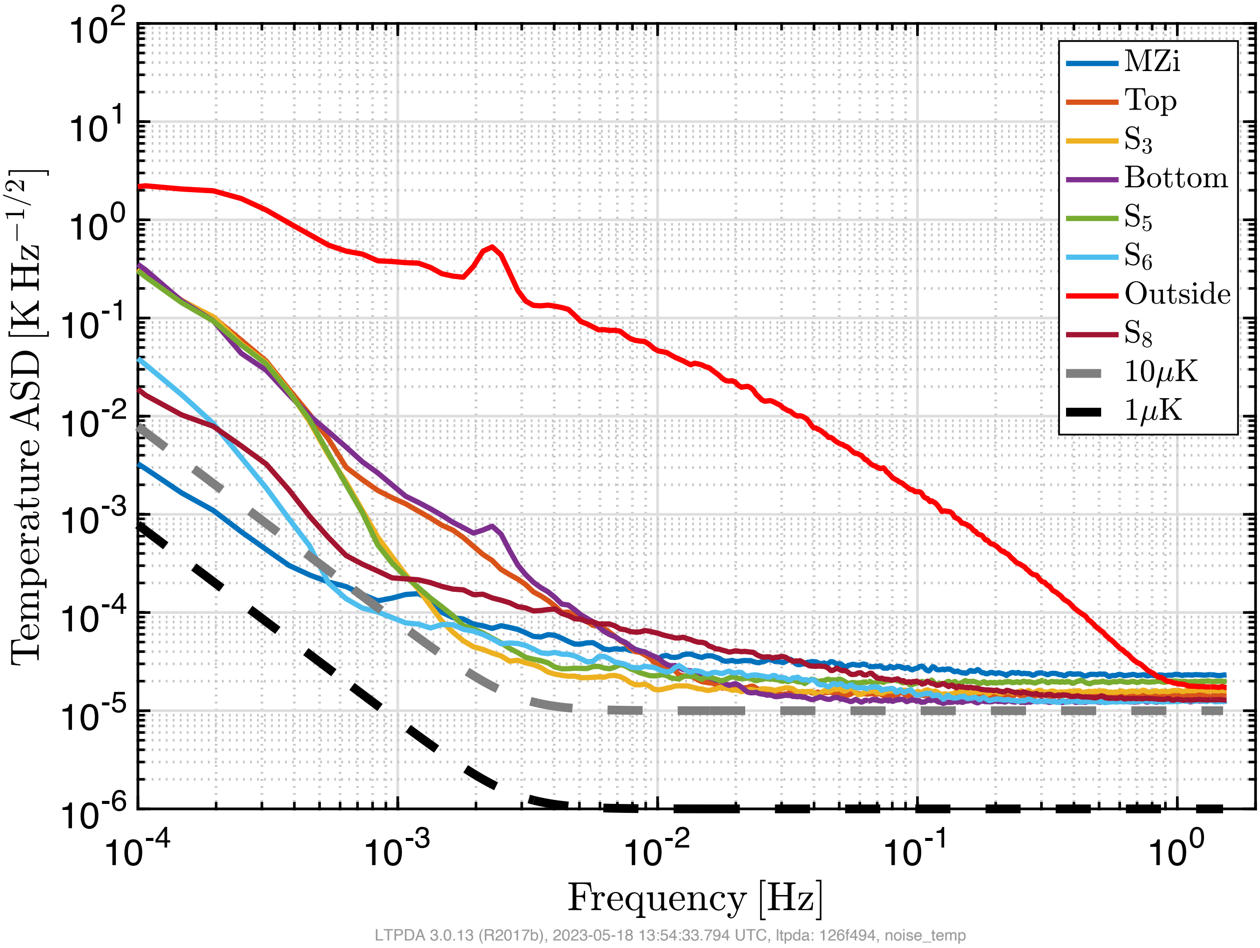

Figure 5.10: Amplitude Spectral Density of the different temperature sensors measured during operational work as it can provide insights into the sensor's performance under real-world conditions.

sensitivity to different frequencies and identify potential noise sources. This information can be used to improve the sensor's performance or to select a sensor better suited for a particular application. An electrical circuit board designed at the AEI, containing low-noise preamplifiers and high-resolution analog-to-digital converters (ADCs), provides input and output channels for the eight sensors and is connected via Universal Serial Bus (USB) to the PC. The calibration of each sensor, as well as the entire electrical circuit, was meticulously performed manually. This process involved the direct application of a human hand (in which the corporal temperature is about 36°C), where the measured value was introduced in the C++ program.

Figure 5.11: Picture of the TLB 6821 from Newport with the corresponding low noise driver, TLB 6800-LN, also from Newport, shown on the left. A picture of the "Mephisto" NPRO from Coherent is shown on the right. Credits: Newport and Coherent.

5.3.4 Laser systems

The first-proof-of-principle experiment of an interferometric set-up using DFM technology was demonstrated within the SFB geo-Q in Hannover (Germany) in collaboration with the National Institute of Standards and Technology (NIST) (Maryland, USA) by Dr. Oliver Gerberding and Dr. Katharina-Sophie Isleif. In this thesis, two kinds of lasers have been used, as seen in Fig. 5.11: the rapidly tunable external cavity diode laser (ECDL) TLB-6821 from Newport [96], mainly used for DFM experiments, and the non-planar ring oscillator (NPRO) "Mephisto" laser from Coherent [97] (also tunable in frequency via piezo and temperature but much less and slower), much more stable in frequency than the TLB-6821, which is used for the DC balanced readout scheme,

DFM interferometry promises compact, small, and simple optical setups. Attaining interferometric configurations with pathlength differences on a centimeter scale requires the laser beam to undergo frequency modulation of a magnitude around several gigahertz. Although there are some laser sources suitable for DFM interferometry, the chosen laser was the same as [88], a fiber-coupled version of an external cavity diode laser (ECDL) provided by Newport, which has the desired frequency modulation parameters, with a wavelength of λ = 1064nm and an output power of 40 mW. In [88], the parameters of the TLB 6821 can be found in detail. The DC balanced readout experiment used an NPRO 1064 nm laser, which is frequency stabilized to an iodine reference (Prometheus from Coherent) and has an output power of about 500 mW. Details on iodine-stabilized NPROs for space-based applications and the system from Coherent can be found in [98].

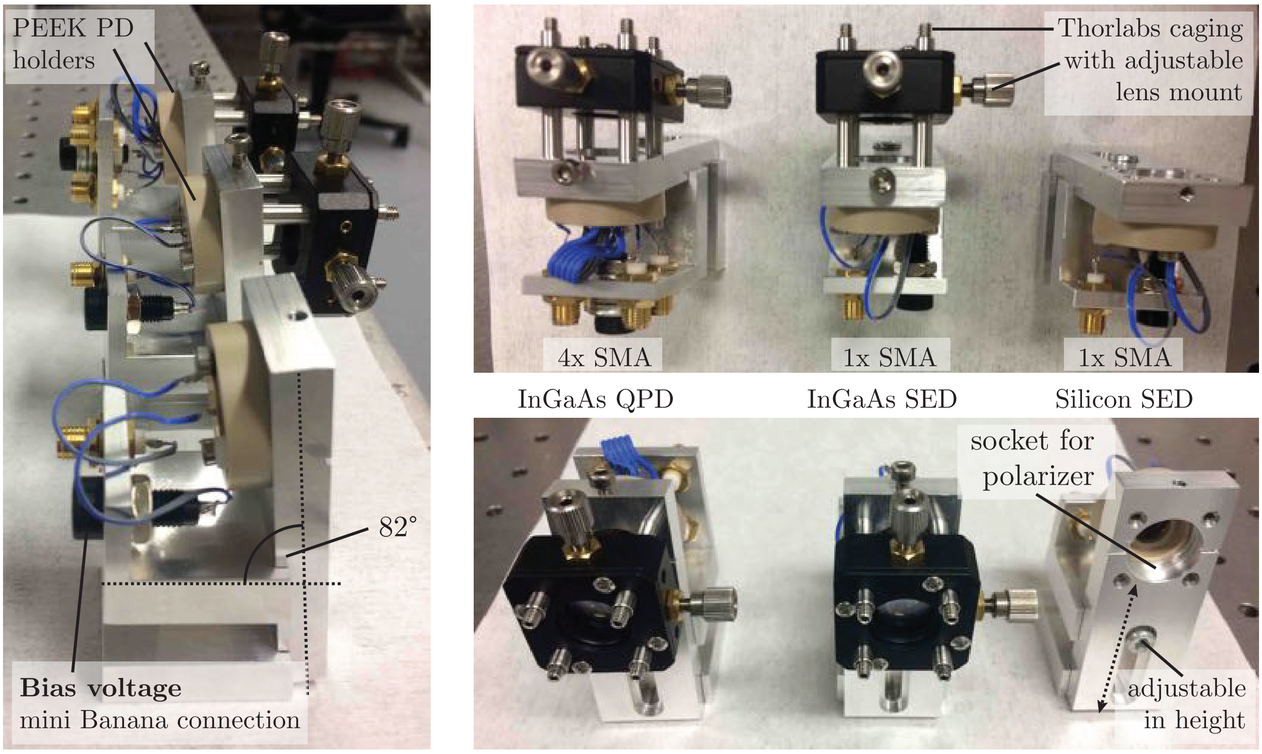

Figure 5.12: Photographs of the photodiode mounts for InGaAs QPD GAP1000Q, InGaAs SED LAPD-1-09-17-TO46 and silicon (Si) PC50. The aluminium front plate is angled by 8°, as well as the socket for the thin-film polarizers. The diode is isolated from the aluminium mount by an adapter made of PEEK. Focusing lenses for small diodes are installed in an XY translational mount from Thorlabs, SCP05, mounted by a 16 mm Caging System. Credits: K.S. Isleif.

5.3.5 Photodetectors

For DFM experiments, kHz heterodyne frequencies instead of MHz will be used, allowing the physical separation of photodiodes from transimpedance amplifiers (TIAs). The design of the photodiode mounts for the DFM test is based on the layouts from the Backlink experiment, where they consist of an aluminium base on which a plate (adjustable in height and angled by 8° to avoid back-reflections) that holds the photodiode can be mounted. Fig. 5.12 shows some photographs of the assembly with the photodetectors used for different purposes: InGaAs photodetectors LAPD-1-09-17-TO46 (active area of 1 mm diameter) from Roithner Lasertechnik are used for the interferometric readout in the MZI and laser power stabilization; QPDs GAP1000Q (also having an active area of 1 mm diameter which is divided into four segments, separated from each other by a slit of about 20 μm) from Opto-Electronic Components (OEC GmbH), which will be used for future DFM experiments involving test mass control and test the SEDI interferometer (see chapter 6); Si-SED-PC50 from First Sensor (active area of about 7.98 mm) are used for DC balanced experiments (see section 5.4). All the photodiodes include PEEK holders with different socket sizes, ensuring that the photodiode is isolated from the aluminum mount and, therefore, is only connected to the bias voltage and signal pins. Due to the small diode size, focusing lenses with a 25.4 mm focal length were used in front of them. They are mounted in an XY translational mount from Thorlabs, SCP05, which is compatible with the 16 mm Caging System by which they are mounted at the aluminium plate. Si-SED-PC50 photodiodes also include external focusing lenses with the same focal length to reduce beam-walk effects.

It has been mentioned that the InGaAs photodetectors LAPD-1-09-17-TO46 are used for amplitude stabilization, a technique that involves continuously monitoring the laser power and comparing it to a reference or desired value to maintain a consistent power level in the signal. This comparison results in an error signal representing the difference between the detected and the reference amplitudes. The error signal is then used in a feedback control system to make necessary adjustments, thereby reducing the error. For that, a single-axis FiberBench (FT-38X135 from Thorlabs) and 2 FiberPorts (PAF2-5C from Thorlabs) were used. The FiberBench includes a $\lambda/4$ and $\lambda/2$ waveplates and a linear polarizer module for polarization cleaning. There is also a FiberBench Beamsplitter Module (FBT-BSF-C from Thorlabs) where 96% of the incident light is transmitted to the FIOS/MZI, and 4% is reflected to the photodetector (which includes a focusing lens with 25.4 mm focal length) used for amplitude stabilization, as is seen in Fig. 5.13.

Using a servo designed by M. Mehmet to control fast amplitude fluctuations, which are achieved by modulating the laser diode current via the NPRO laser (which later will be used for the DC balanced experiment described in section 5.4), the control open loop achieves a unity-gain frequency of 3.5 kHz and a phase margin of 25°, as is shown in Fig. 5.14a. Fig. 5.14b shows how the NPRO locked to the MZI and mixed with the iodine-stabilized laser provides frequency noise below the NPRO free running noise in all the frequency band below 20 Hz.

Figure 5.13: Photography of the Amplitude Stabilization scheme which includes a $\lambda/4$, $\lambda/2$ and linear polarizer module for polarization cleaning and a FiberBench Beamsplitter Module 96:4 for amplitude stabilization and feeding with light the MZI.

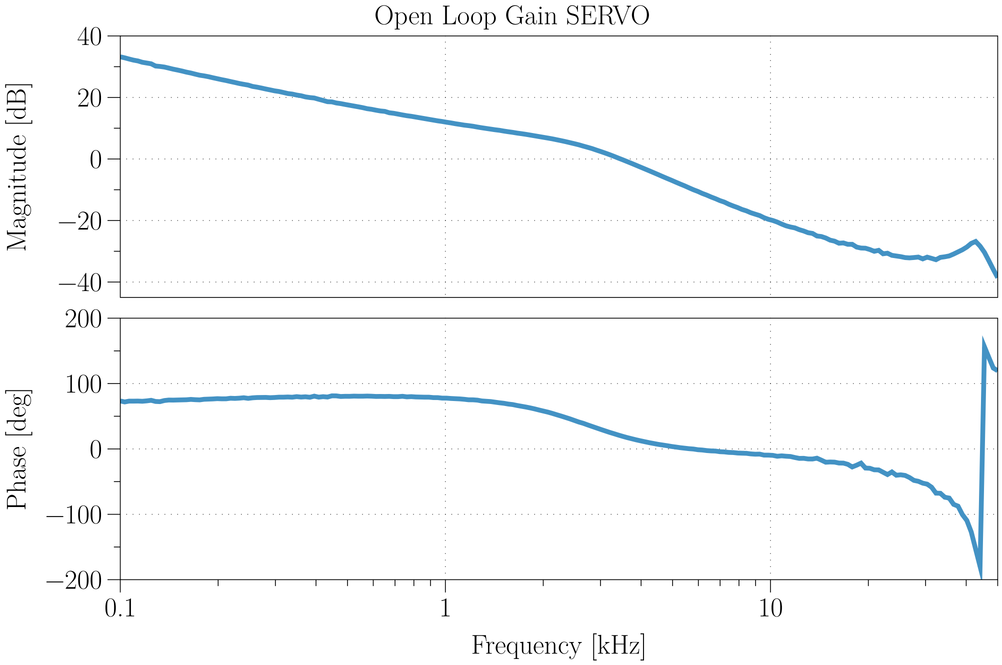

(a) Open Loop PID gain servo.

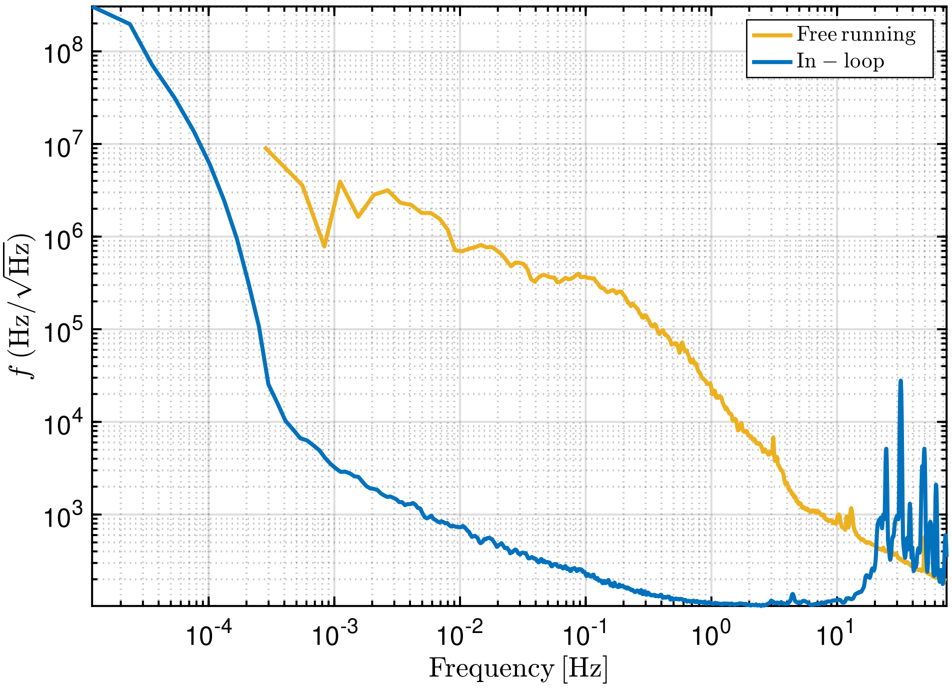

(b) Frequency noise of the free running vs. in-loop signal.

Figure 5.14: (a) Measured open loop transfer functions of the laser amplitude stabilization and (b) frequency noise spectral densities of the laser frequency stabilization. The frequency noise spectrum is shown with (in-loop signals) and without a feedback control loop.

5.4 Laser frequency stabilization via the MZI and balanced DC readout

Laser frequency noise is one of the leading sources of noise in laser interferometric inertial sensors, particularly below 1 Hz, even if the macroscopic interferometer arm lengths are matched using best efforts and even when using commercial narrow-linewidth lasers. To achieve sub-picometer sensitivities in the millihertz band, some form of reduction of the laser frequency noise is required, where the usual schemes involve stabilizing the laser to an ultra-stable optical cavity or an atomic or molecular reference. Such schemes are also commercially available, but they are bulky, costly, and rely on complex electronics. In [89], the quasi-monolithic compact MZI with the commercial fiber collimator was introduced as a simpler alternative to conventional laser locking schemes. Recent advances in interferometry techniques that rely on some form of self-homodyning [85, 86, 99, 100] motivated the implementation of the DC balanced stabilization scheme. Additionally, the DC-balanced readout scheme is a straightforward technique that does not require any modulation or AC readout electronics, making this scheme an interesting option for other experiments that require frequency noise reduction. Compared to an optical cavity or an atomic or molecular reference, the MZI technique offers a wide operating range and does not require a complex lock acquisition procedure. Continuous frequency tuning is possible by purely electronic means and does not require physically changing the resonance frequency of the frequency reference. The MZI in [89] was shown to provide impressive long-term dimensional stability, beating the sub-picometer mark at 5 mHz (for comparison, the LTP interferometer beats this mark at 10 mHz [33, 101]).

To test the FIOS's long-term stability in the upgraded MZI before it is used as a reference for future DFM experiments, frequency stability measurements were performed using the same balanced homodyne DC readout scheme.

5.4.1 DC balanced readout mathematical description

In mathematical terms, DC balance refers to the property of a signal where the average or mean value over time is zero (or some other constant value). In other words, the positive and negative parts of the signal balance each other out over time. This signal, commonly named an ”error signal”, is the difference between the desired output of a system and the actual output of the system. The error signal is used to drive the controller, which in turn adjusts the input to the system to

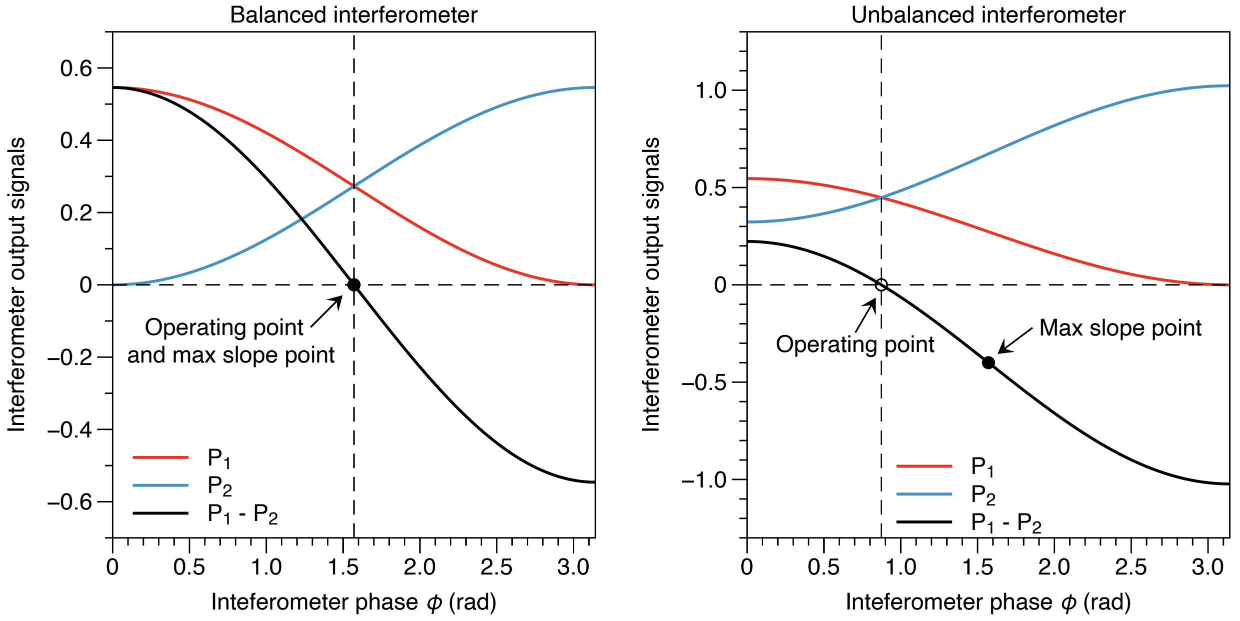

(a) Balanced interferometer.

(b) Unbalanced interferometer.

Figure 5.15: (a) Balanced interferometer. The operating point and the maximum slope are at zero, therefore, the amplitude noise of the laser cancels out, and then it is possible to lock the laser to the interferometer. (b) Unbalanced interferometer. The operating point is at zero, but the maximum slope is not. When it happens, theoretically is possible to lock the laser to the interferometer, but in practice, it is extremely difficult to maintain the lock.

reduce the error and bring the system output closer to the desired value.

In this case, DC balance will be referred to as the direct current subtraction of two photodetectors, PD_1 and PD_2. Being P_1 the optical power at PD_1 given by $P_1 = \bar{P}_1\,(1 + c_1 \cdot \cos[\varphi_l - \varphi_s])$ and P_2 the optical power at PD_2 given by $P_2 = \bar{P}_2\,(1 + c_2 \cdot \cos[\varphi_l - \varphi_s + \pi])$, where P_1 and P_2 are the signal amplitude, c_1 and c_2 are the contrast factor and φ_l and φ_s are the interferometer phase in the long and short arm respectively, a direct current subtraction is given by:

$$P_1 - P_2 \propto \bar{P}\,[\cos\varphi\, - \cos\,(\varphi + \pi)] = 2\,\bar{P}\cos\varphi\,, \tag{5.3}$$

where $\bar{P}_1 = \bar{P}_2 = \bar{P}$, $\varphi = \varphi_l + \varphi_s$ and $c_1 = c_2 = 1$ assuming equal optical power on the interfering beams and 100% contrast.

To get a balanced operation in the mid-fringe, the generated sinusoidal output signal contains regular zero crossings that can be used for locking without the need for subtracting an additional reference signal, that is, when $\bar{P}_1 - \bar{P}_2 = 0$. In the case of an unbalanced interferometer, the operating point does not match the max

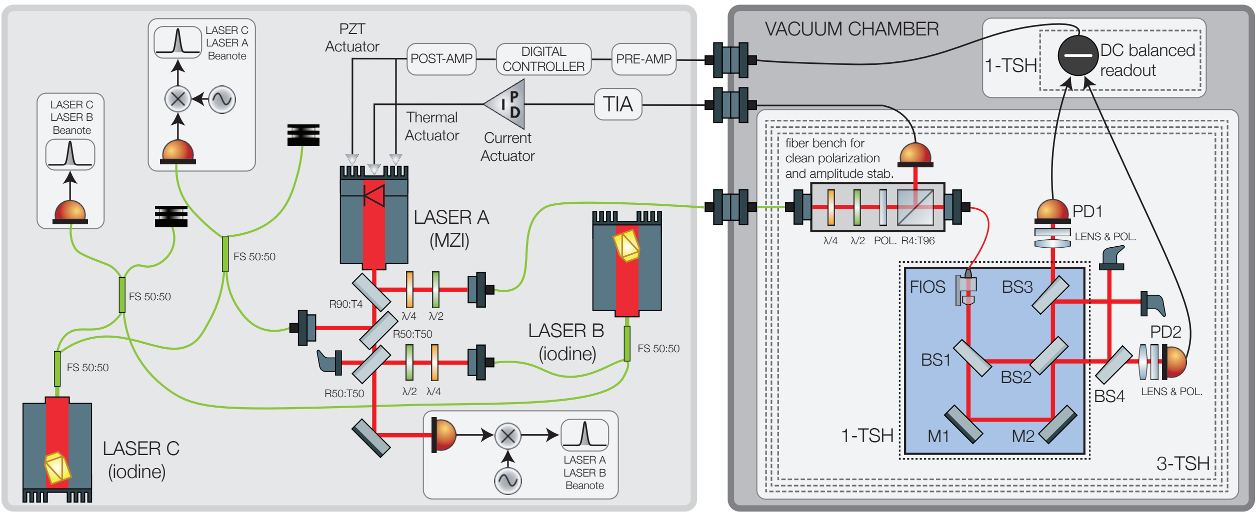

Figure 5.16: Experimental setup. Light from laser A is injected into a vacuum chamber, where it is fed to the ultra-stable interferometer (blue box) via FIOS. The interferometer, along with the auxiliary optics and detectors for polarization cleaning, amplitude stabilization, and interferometric readout, is located inside a high-performance triple-layered thermal enclosure (3-TSH) with an additional single-layer thermal shield (1-TSH) surrounding just the Mach-Zehnder interferometer. The difference-current between the two readout diodes is converted into a voltage by a homemade electronic circuit surrounded by another single-layer thermal enclosure (1-TSH). The signal is processed by a digital servo and fed back to the laser's slow and fast frequency actuators. Laser A is beaten with two iodine-stabilized lasers (lasers B and C) to help assess the achieved stability. The beat signals are mixed down to below 100 MHz with an ultra-stable signal generator and read out via a phasemeter.

slope point, unlike in the previous case.

5.4.2 Experimental description

The experimental setup is depicted in Fig. 5.16. The MZI with an arm length difference of $\Delta l \approx 7\,\mathrm{cm}$ is used as an ultra-stable length reference for laser frequency stabilization of laser A, which is a 1064 nm non-planar ring oscillator (NPRO) laser. The detection is performed by two identical $50\,\mathrm{mm}^2$ circular active area silicon PIN photodiodes located at the complementary output ports of BS2. A focusing lens is placed in front of each photodiode to help minimize transverse beam jitter; also, thin-film polarizers with high extinction ratios are mounted directly in front of the photodiodes to mitigate the impact of parasitic interferences arising from residual beams with orthogonal polarizations. The photodiodes are operated in reverse bias voltage and connected in a balanced differential trans-impedance amplifier (TIA), performing a direct current subtraction. The basic schematic of the sensor is shown in Fig. 5.17.

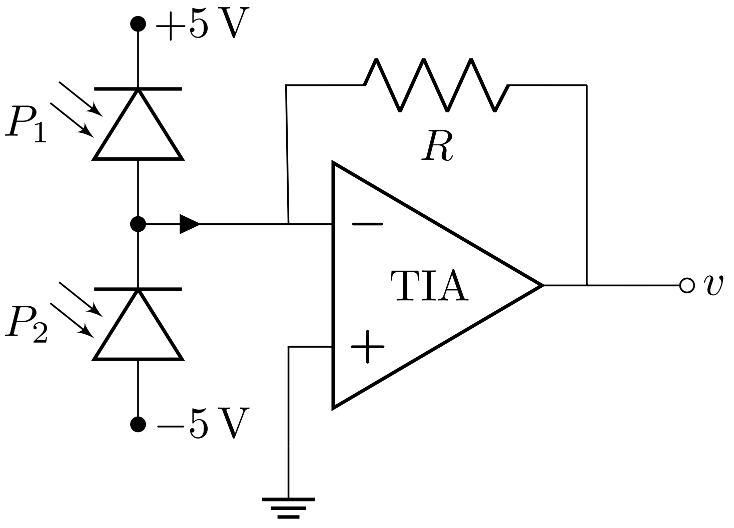

Figure 5.17: Schematic of the balanced differential trans-impedance amplifier (TIA).

As seen in section 5.4.1, the power at each photodiode depends on the laser frequency f and is given by

$$\begin{aligned} P_1(f) &= p_1 \left[1 + c_1 \cdot \cos\left(\frac{2\pi f \Delta l}{c} + \varphi_0\right)\right] \\ P_2(f) &= p_2 \left[1 + c_2 \cdot \cos\left(\frac{2\pi f \Delta l}{c} + \varphi_0 + \pi\right)\right] \end{aligned} \tag{5.4}$$

where $p_{1,2}$ are the optical powers at each photodetector in mid-fringe, $c_{1,2}$ are the interferometric contrasts at each photodetector, Δl is the interferometer's optical path length difference, c is the speed of light, and φ_0 is an arbitrary constant. After the TIA, the resulting signal is given by

$$\begin{aligned} v(f) &= G\left[P_1(f) - P_2(f)\right] \\ &= G\left[p_1 - p_2 + (c_1 p_1 + c_2 p_2) \cdot \cos\left(\frac{2\pi f \Delta l}{c} + \varphi_0\right)\right] \end{aligned} \tag{5.5}$$

where G [V/W] is the trans-impedance gain. To attain balanced operation (i.e., $p_1 = p_2$), the reflectivity dependence of BS4 on the macroscopic beam incidence angle is exploited, achieving nearly equal power levels on both photodiodes, such that

$$v(f) = Gp_1(c_1 + c_2) \cdot \cos\left(\frac{2\pi f \Delta l}{c} + \varphi_0\right) \tag{5.6}$$

Eq. 5.5 has periodic zero crossings that are used for laser locking. The slope of the error signal at the operating point is proportional to the available optical power, the interferometric contrasts, the trans-impedance gain, and the interferometer's arm length difference. A Moku:Lab by Liquid Instruments [102] is used as a digital controller to provide feedback based on the generated error signal to both the slow thermal actuator and the fast piezo-electric transducer actuator of the NPRO laser. Additionally, a pre-amplifier (SR560 by Stanford Research Systems) and a post-amplifier equipped with a low-pass filter are used to mitigate analog-to-digital converter noise originating from the digital servo and to enhance the low-frequency gain, respectively.

When the laser is locked to the MZI, the optical pathlength stability of the interferometer is transferred to the frequency stability of the laser, obeying Eq. 4.1. To isolate the MZI from external perturbations affecting its pathlength noise δl, it is placed inside a vacuum chamber at a moderate pressure of 10^{-6} mbar and surrounded by a set of the three aluminium heat shields (see Fig. 5.18), similar to the systems designed for high-performance metrology with ultra-stable optical reference cavities [103, 104].

Laser A is split in two ways. One part of the light feeds the vacuum chamber, where it is further split such that a small fraction is captured by a photodetector to stabilize the laser's amplitude, and the rest is injected into the MZI. The other part is split in two ways and interfered with two reference lasers to enable measurements of the achieved stability. The reference systems, lasers B and C, are two iodine-stabilized NPRO lasers (Prometheus by Coherent), locked to the molecular iodine hyperfine transitions R(56)32-0 'a1' and 'a2'. Laser B, which was repaired recently, corresponds to the iodine-stabilized NPRO with s/n 1723A used in the AEI many years ago in the Backlink experiment. Laser C corresponds to the iodine-stabilized NPRO with s/n 1915D, currently used by the TDOBS team. The two reference lasers are also interfered with, generating a third beatnote signal that allows a complete characterization of the three systems' stability (see section 5.4.4). The three beatnotes are captured by high-speed InGaAs photoreceivers. The two beatnotes with laser A, which are in the 0.5-2 GHz band, are mixed down to less than 100 MHz using an ultra-stable GHz signal generator (SMB100A by Rohde & Schwarz). Finally, the three beatnotes are tracked simultaneously by a

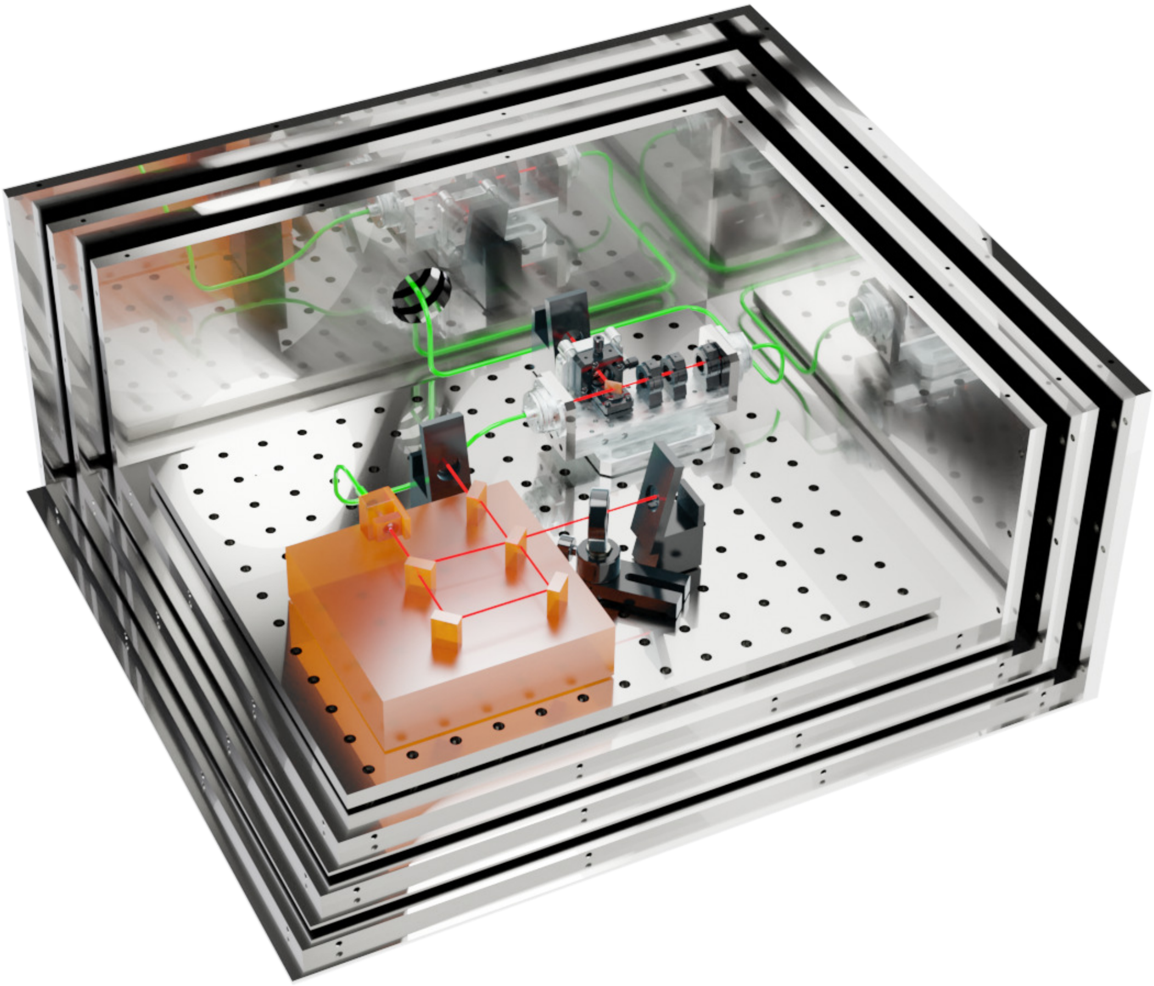

Figure 5.18: The next-generation unequal-arm Mach-Zehnder interferometer consists of an ultra-stable glass ceramic baseplate to which the fused silica components and the fiber injector optical subassembly are bonded via UV adhesive. A set of three aluminium heat shields isolates the interferometer from external temperature fluctuations. The aluminium plate surfaces are polished to lower their emissivity and slow down radiative heat transfer inside the enclosure.

Moku:Pro phasemeter [102]. The noise contributions of the signal generator and the phasemeter instrument are measured to be well below $1\,\mathrm{Hz}/\sqrt{\mathrm{Hz}}$ throughout the whole band.

Given an arm-length difference of Δl=7 cm of the MZI, the measured frequency fluctuations δf can be used to determine the effective displacement noise δl using the laser wavelength $\lambda_0 \approx 1064.5$ nm and the speed of light c,

$$\delta l = \Delta l \times \frac{\delta f}{f_0} = \Delta l \times \frac{\delta f \lambda_0}{c}. \tag{5.7}$$

By reversing this calculation, the frequency-noise level given by

$$\delta f = \frac{\delta l \cdot c}{\Delta l \cdot \lambda_0} = 4.026\,\mathrm{kHz}/\sqrt{\mathrm{Hz}} \tag{5.8}$$

can also be calculated for achieving a displacement noise of $\delta l = 1\,\mathrm{pm}/\sqrt{\mathrm{Hz}}$, which, considering reflection setups, the inclusion of geometry provides an additional factor of approximately two, resulting in a frequency noise level of approximately 8.052 $\mathrm{kHz}/\sqrt{\mathrm{Hz}}$.

5.4.3 Laser frequency stability

The frequency stability of the laser is important for precision measurements in interferometers with unequal arm lengths. For that reason, before measuring the stability of the MZI, the two identical iodine-stabilized laser systems described in 5.4.2, Laser B and Laser C, were installed independently to have the possibility to monitor their performance, interfering with both lasers and readout with a photodiode the resulting beatnote. Fig 5.19 shows a schematic of the measurement setup. The power of the reference laser was reduced using a waveplate and some grey filters. Most of the power was dumped to get comparable power levels of a few mW for both interfered beams (∼1.5 mW). The two laser systems were stabilized on two different absorption lines previously used, ’a1’ and ’a2’, which are separated by approximately 130 MHz. The spectrum of the measured beat note is shown in Fig 5.20, which is compared to a similar measurement taken by Maike Lieser in her PhD thesis [105].

With this kind of beat measurement, it is not possible to distinguish which of the two laser systems is responsible for the increased frequency noise. Still, it was assumed the older system (serial number 1915D) lost performance from 2 mHz to 1 Hz since it is well-known that 1723A was optimized again in 2021.

5.4.4 Three-Corner-Hat measurement

In the previous section, it was observed it is not possible to distinguish which of the two iodine-stabilized laser systems is responsible for the poor performance. However, it was assumed that 1915D lost performance over time. To evaluate the performance of each single laser, independently from the rest, it was carried

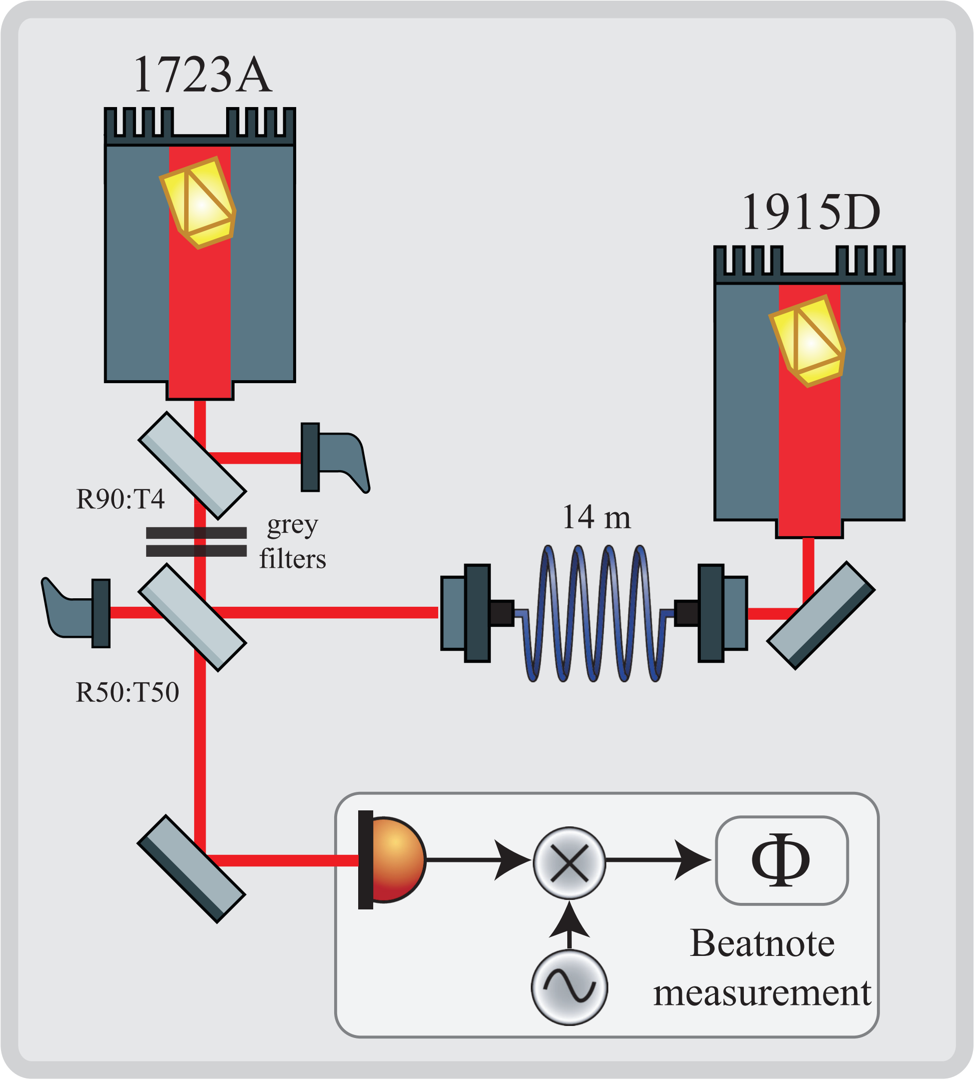

Figure 5.19: Schematic of the measurement setup between Lasers 1723A ("new" iodine) and 1915D (TDOBS iodine). A Moku:PRO was used to measure the stability beatnote.

out a three-cornered-hat (3CH) analysis [106] using the modified Allan deviation (MDEV) and the Hadamard deviation (HDEV) as the statistic functions of choice [107]. 3CH is a well-known method that allows estimating the absolute stability of the experimental system by comparing it with two other reference lasers. Also, it is relatively simple to implement and relatively insensitive to environmental noise. The 3CH measurement involves comparing the frequency of three oscillators to each other, which is performed by measuring the Allan deviation of the frequency difference between the oscillators, which is a measure of the frequency stability of an oscillator. The smaller the Allan deviation, the more stable the oscillator.

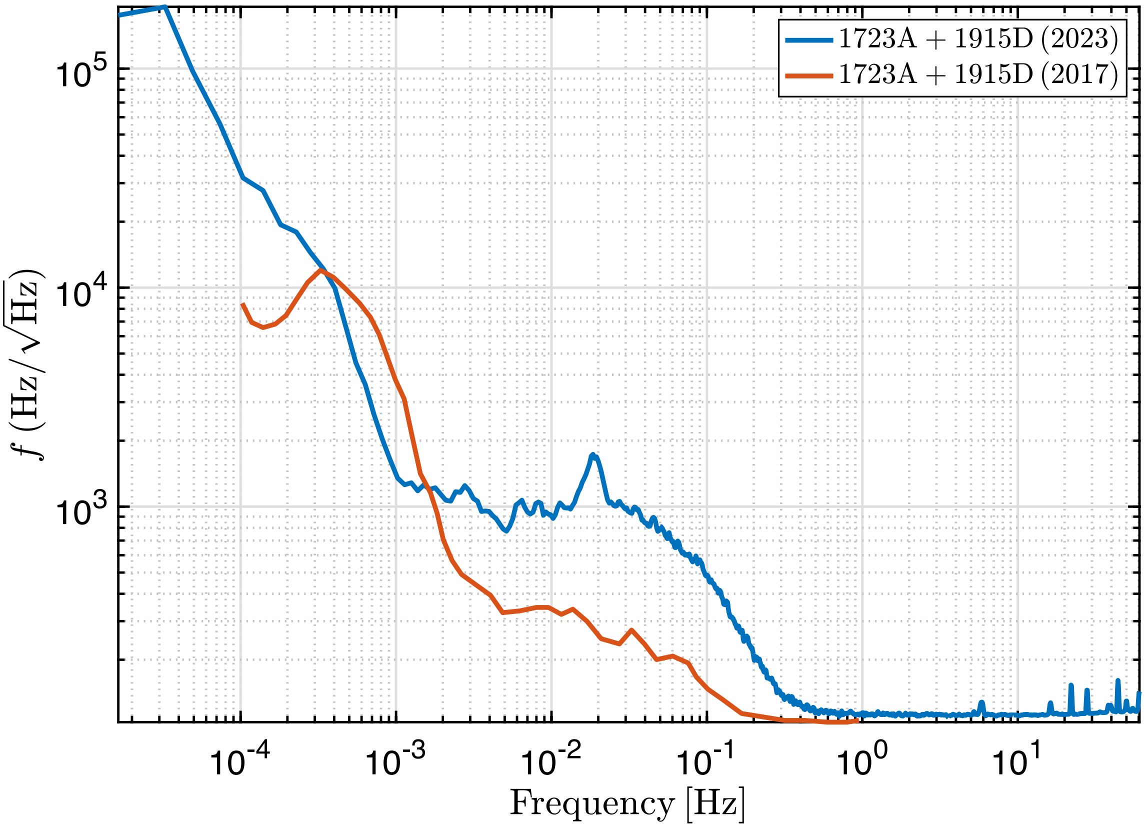

Figure 5.20: Schematic of the measurement setup between Lasers 1723A (”new” iodine) and 1915D (TDOBS iodine). A Moku:PRO was used to measure the stability beatnote.

Assuming total un-correlation between the three systems, the individual variances can be separated algebraically. Let be A the system under test (the MZI-stabilized system or laser A) and B and C the two other reference iodine stabilized lasers, it is assumed that their signals are completely uncorrelated, therefore:

$$\begin{aligned} \sigma^2_{A-B}(\tau) &= \sigma^2_A(\tau) + \sigma^2_B(\tau), \\ \sigma^2_{A-C}(\tau) &= \sigma^2_A(\tau) + \sigma^2_C(\tau), \\ \sigma^2_{B-C}(\tau) &= \sigma^2_B(\tau) + \sigma^2_C(\tau), \end{aligned} \tag{5.9}$$

where σ_{A-B}, σ_{A-C} and σ_{B-C} are the Allan deviations of the beat notes of system A with B, system A with C, and system B with C, respectively. The individual variances may be obtained algebraically as

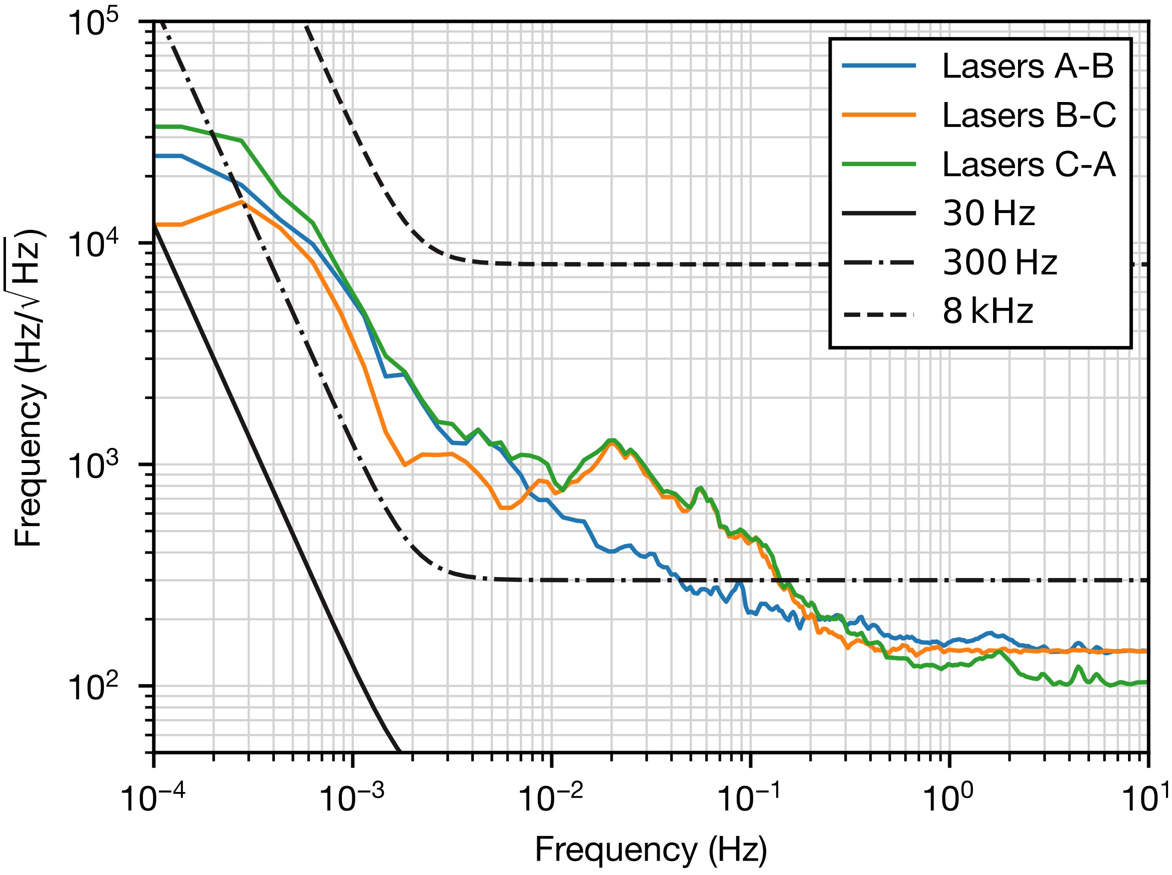

Figure 5.21: Frequency spectral densities of a 2-hour measurement of the three beatnotes (A: MZI-stabilized laser; B, C: iodine-stabilized lasers). Also shown are the frequency noise spectral densities of $30\,\text{Hz}/\sqrt{\text{Hz}} \cdot u(f)$, $300\,\text{Hz}/\sqrt{\text{Hz}} \cdot u(f)$, and $8\,\text{kHz}/\sqrt{\text{Hz}} \cdot u(f)$.

$$\begin{aligned}
\sigma_A^2(\tau) &= \frac{1}{2}\left(\sigma_{A-B}^2(\tau) + \sigma_{A-C}^2(\tau) - \sigma_{B-C}^2(\tau)\right), \\
\sigma_B^2(\tau) &= \frac{1}{2}\left(\sigma_{A-B}^2(\tau) + \sigma_{B-C}^2(\tau) - \sigma_{A-C}^2(\tau)\right), \\
\sigma_C^2(\tau) &= \frac{1}{2}\left(\sigma_{A-C}^2(\tau) + \sigma_{B-C}^2(\tau) - \sigma_{A-B}^2(\tau)\right).
\end{aligned} \tag{5.10}$$

The frequency spectral densities [72] of the three beatnotes are shown in Fig. 5.21, which also shows the frequency noise spectral density of $30\,\text{Hz}/\sqrt{\text{Hz}}$, $300\,\text{Hz}/\sqrt{\text{Hz}}$, and $8\,\text{kHz}/\sqrt{\text{Hz}}$, respectively representing the stability of a space-qualified cavity-stabilized laser system, the LISA laser frequency pre-stabilization target, and the picometer-equivalent frequency instability of an interferometer with 7 cm arm length difference scaled by Eq. 4.3. Inspection of these results reveals that the MZI-stabilized system (laser A) offers stability comparable to the two iodine-stabilized systems (lasers B and C). This complicates assessing the achieved stability since the frequency noise of the reference lasers must be addressed compared to the frequency noise of the unit under test.

The MDEV is chosen for its ability to distinguish between white and flicker phase noise at short averaging times (i.e., at short $\tau = m\tau_0$, where τ is the averaging time, τ_0 is the gate time or sampling time, and m is the averaging factor), or equivalently at high frequencies. The MDEV is also widely used in the time and frequency standards community, such that the stability results may be easily compared to other references. The HDEV is chosen for its ability to handle divergent noise sources at long averaging times. The MDEV is not a good statistic for processes having power spectral densities with f^{-4} dependency (e.g., as Eq. 4.3), as the obtained variance at long τ may depend on the measurement time. On the other hand, the HDEV examines the second difference of the fractional frequencies, which makes it robust against f^{-4} noise, allowing a direct comparison of the achieved long-term stability with noise allocations following Eq. 4.3.

Frequency data were taken over 12 h by the same phasemeter with a gate time of 6.7 ms. The data set was cut into ten sections of 1.2 h, a linear drift was removed for compensating the temperature drift in each section, and the individual Allan deviations were calculated. The arithmetic mean and standard deviation of the resulting modified Allan deviation are shown in Fig. 5.22, which also shows the MDEV of the MZI stability reported in [89], obtained via a domain conversion from the power spectral density using the MDEV transfer function [108], and the MDEV of virtual beatnotes having white frequency noise spectral densities at the $30\,\mathrm{Hz}/\sqrt{\mathrm{Hz}}$, $300\,\mathrm{Hz}/\sqrt{\mathrm{Hz}}$, and $8\,\mathrm{kHz}/\sqrt{\mathrm{Hz}}$ levels. Finally, given that the Hadamard deviation at long averaging times is the area of interest, the data is downsampled by a factor of 100 in order to decrease the otherwise long computation time of the HDEV. An averaging operation is performed to downsample the data, which limits the results to $\tau > 100 \cdot \tau_0$. The results are shown in Fig. 5.23, together with the HDEV corresponding to virtual beatnotes with $30\,\mathrm{Hz}/\sqrt{\mathrm{Hz}} \cdot u(f)$, $300\,\mathrm{Hz}/\sqrt{\mathrm{Hz}} \cdot u(f)$, and $8\,\mathrm{kHz}/\sqrt{\mathrm{Hz}} \cdot u(f)$ frequency spectral densities, obtained by numerically computing the HDEV on data generated by a simple noise model that conforms to Eq. 4.3.

The three-cornered-hat analysis reveals the individual performance of each laser. The noise bump of laser C is successfully isolated at τ between 1 and 10 s.

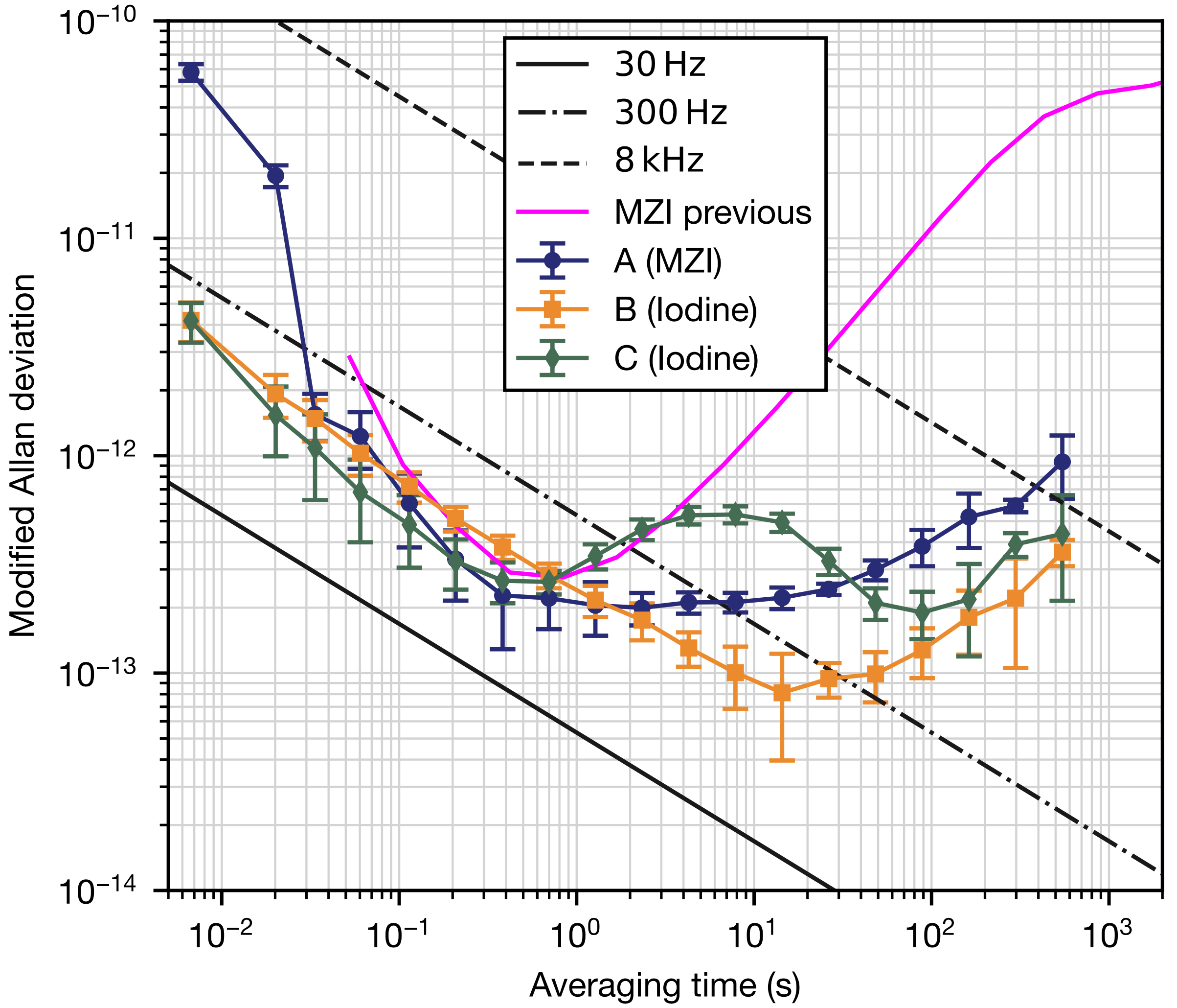

Figure 5.22: Modified Allan deviation of the three stabilized lasers derived from a three-cornered hat analysis. The data show the average instability of 10 data sets with a duration of 1.2 hours each. Error bars represent the standard deviation of the data averaged for each point. Also shown are the modified Allan deviations of virtual beatnotes with white frequency noise at $30\,\mathrm{Hz}/\sqrt{\mathrm{Hz}}$, $300\,\mathrm{Hz}/\sqrt{\mathrm{Hz}}$, and $8\,\mathrm{kHz}/\sqrt{\mathrm{Hz}}$.

At $\tau > 10\,\mathrm{s}$, laser B is roughly a factor 2 to 3 more stable than laser A. At lower averaging times, their stability is very similar, except at very short averaging times ($\tau \sim 10\,\mathrm{ms}$), where the MZI suffers from short-lived instabilities originating from the coupling of vibrations of the vacuum pumps.

As per the obtained MDEV, the MZI's fractional frequency instability is below 10^{-12} at averaging times greater than 0.1 s and over a few hundred seconds. A maximal stability of 2×10^{-13} is achieved between 1 and 10 s that is dominated

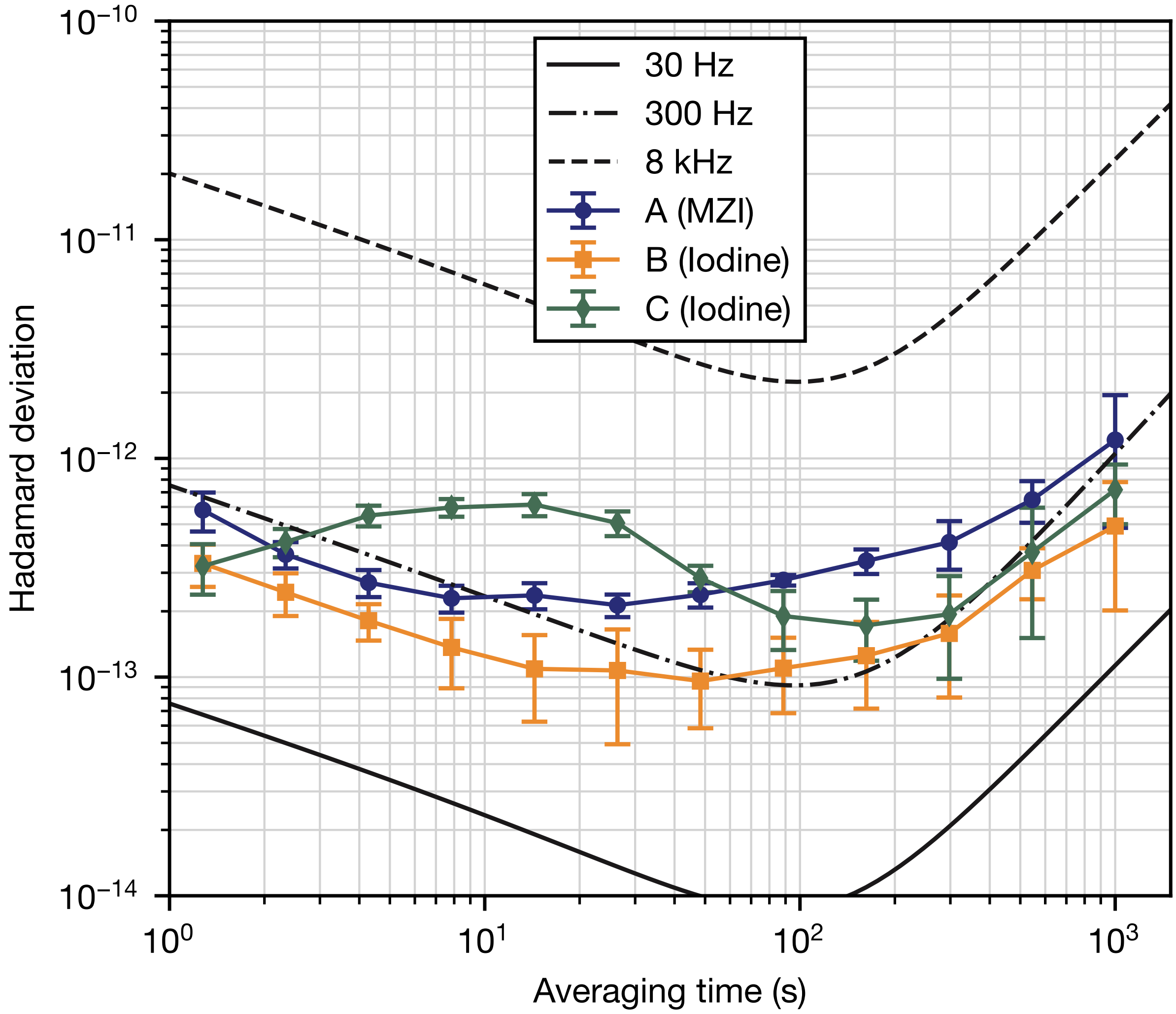

Figure 5.23: Hadamard deviation of the three stabilized lasers derived from a three-cornered hat analysis. The data show the average instability of 10 data sets with a duration of 1.2 hours each. Error bars represent the standard deviation of the data averaged for each point. Also shown are the Hadamard deviations corresponding to virtual beatnotes having frequency spectral densities of $30\,\mathrm{Hz}/\sqrt{\mathrm{Hz}} \cdot u(f)$, $300\,\mathrm{Hz}/\sqrt{\mathrm{Hz}} \cdot u(f)$, and $8\,\mathrm{kHz}/\sqrt{\mathrm{Hz}} \cdot u(f)$.

by flicker frequency noise (i.e., $1/f$ noise). On the other hand, the HDEV analysis reveals that the MZI does not meet the LISA target at averaging times between 10 and a few hundred seconds (e.g., it is a factor of 2 less stable at 50 seconds). At 700 seconds, the MZI stability is close to the target, hinting that the system may comply with this noise allocation at even longer measurement times, which can only be revealed by performing longer measurements.

Using Eq. 4.1, it can be inferred the achieved MZI pathlength stability as probed by laser B, shown in Fig. 5.24, and compare it against the previous re-

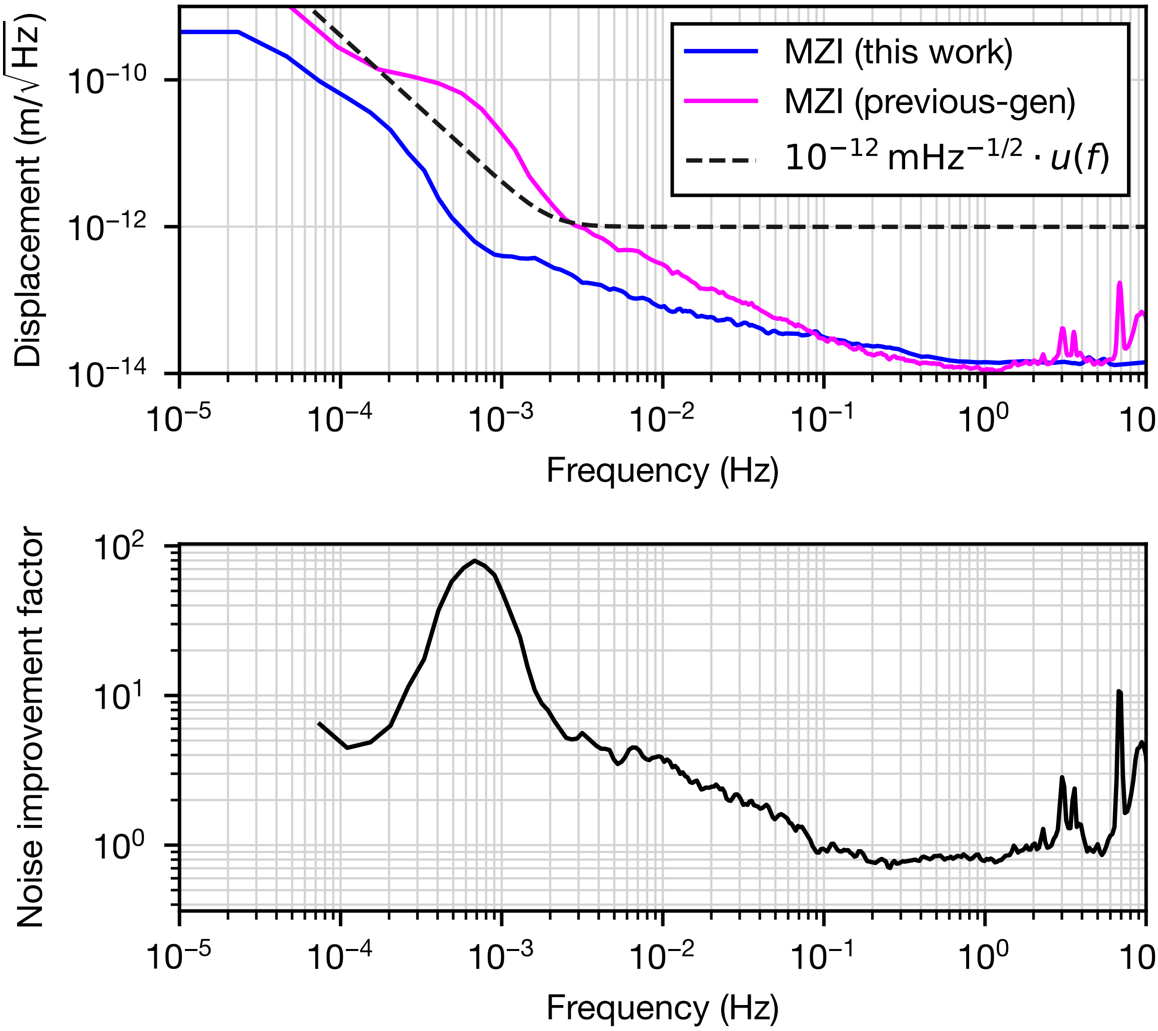

Figure 5.24: Spectral density of optical path length noise in the MZI from a 12-hour measurement, as probed by laser B. The noise floor is limited at the lower frequencies by temperature fluctuations coupling as interferometer path length changes. At frequencies higher than 1 mHz, a $1/f$ power spectrum is observed, which is suspected to be due to the effect of thermal drifts in the sensitive trans-impedance amplifier used to convert the differential interferometric current into a voltage for laser locking. Also shown are the previously realized stability and the 1 pm/$\sqrt{\mathrm{Hz}}\cdot u(f)$ displacement noise allocation commonly used for the local interferometry in LISA.

sults [89]. Thanks to the three-cornered-hat analysis, is shown the estimated stability at the lower frequencies, e.g., at frequencies below 100 mHz, where it was shown that laser B is, on average, 2.4 times more stable than laser A. At higher frequencies (e.g., around 1 Hz), the stabilities of the three lasers are similar, so the performance of laser A may be estimated as $\frac{1}{2}$ of the stability of the A-B or C-A beatnotes, which yields a noise floor of 7 fm/$\sqrt{\mathrm{Hz}}$ at 1 Hz. These results showcase a clear performance improvement of the setup below 100 mHz; therefore, with confidence, it can be claimed that the current MZI, in conjunction with the thermal shields and FIOS, is a promising platform for laser locking and future DFM experiments.

Chapter 6

Single-Element Dual-Interferometer (SEDI)

6.1 Introduction

As seen in chapter 4, one of the main advantages of DFM is the fewer optical components required, allowing for compact layouts without giving up the multi-fringe capabilities. In [87], it was introduced a successful experiment that demonstrated the actual displacement-sensing performance of DFM on the $1\,\mathrm{pm}/\sqrt{\mathrm{Hz}}$ level. The ”Test Mass in the Middle” or TMitM experiment is a single-element interferometer consisting of a custom-made triangular prism capable of sensing the motion of a test mass with sub-picometer precision. A photograph of the interferometers and a small description is shown in Fig. 6.1, where it can be seen the small volume of the single-element interferometer (or as is referred to as ’optical head’), meaning that it is readily scalable to sense one or multiple test masses in several degrees of freedom. However, while the triangular prism optical head is very compact, it relies on a second, separate interferometer (the MZI previously introduced in chapter 5 but in this case without the FIOS) also employing DFM readout for laser frequency pre-stabilization, as seen in [89]. Exploring the possibility of accommodating the inertial sensor and the frequency reference in the same optic, it was designed and later introduced in [109] a self-referenced Single-Element Dual-Interferometer (SEDI) inertial sensor, which is the same as the TMitM, is also capable of reaching sub-picometer precision for frequencies above 10 mHz.

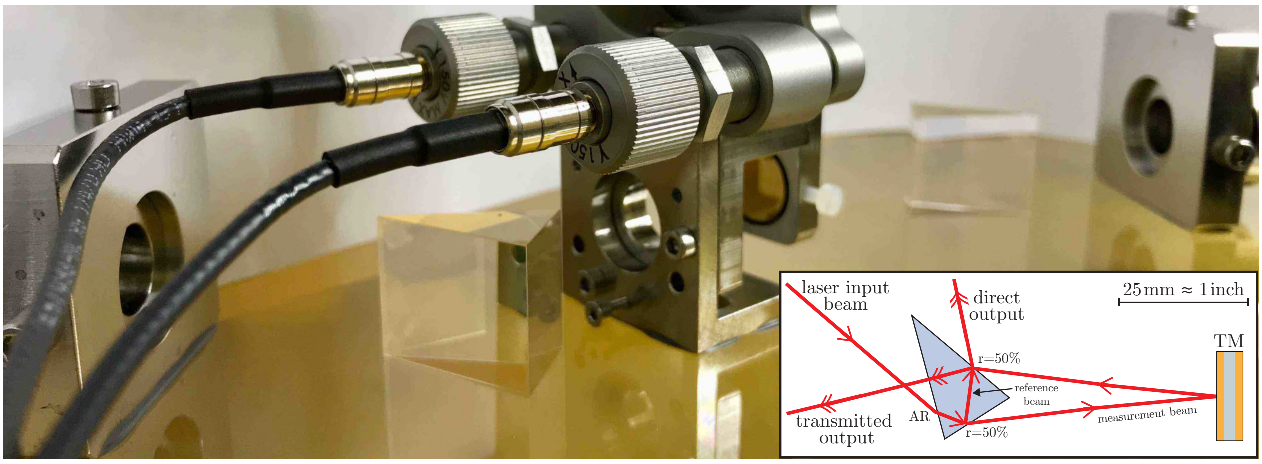

Figure 6.1: Photography of the TMitM where it can be seen one prism is placed on each side of the gold-coated mirror of 12.7 mm diameter, which is suspended from a three-axis piezo actuator. The light is fed into the interferometer via two fiber collimators. The inset shows a sketch of the left prism-shaped interferometer with its beam splitter and antireflective (AR) coating. The laser beam paths are drawn in red and hit the test mass under 4.1°. Credits: K.S. Isleif.

6.2 SEDI design and construction

SEDI's [1] optical head is shown in Fig. 6.2. The interferometer is a pentaprism made of isotropic synthetic fused silica glass, obtained via optical contacting of two smaller parts, which incorporates two unequal arm-length interferometers: a test mass interferometer (TM IFO) and a reference interferometer (Ref IFO), all in the same optic due to a custom-design. The prism features three main optical surfaces with a surface roughness of Ra $<$ 10 Å for a 1064.5 nm wavelength. Surfaces S_1 and S_3 have 50/50 beam splitter coatings that split and recombine laser beams, whereas surface S_2 serves a dual purpose: it functions as a mirror in the reference interferometer (Ref IFO) and as a window in the test mass inertial sensing interferometer (TM IFO), due to its high reflection and anti-reflection coatings (both optimized for S-polarized light), respectively. Using optical fibers in the prism's three main optical surfaces $S_{1,2,3}$, it is possible to split and deliver a single frequency-modulated laser signal to one or several of these optical heads to sense the motion of a system in multiple degrees of freedom and eliminate the need for a separate frequency reference, as in case of the TMitM experiment. On the other hand, the ref IFO has two functions: by feeding back a control signal to the source, it can correct the very slow laser frequency drift, and it also eliminates the possible remaining laser frequency noise coupling from the TM IFO measurements, which

---

[1] Section 6.2 is a summarized version of the paper *Single-Element Dual-Interferometer for Precision Inertial Sensing* by Yang Y, Yamamoto K, Huarcaya V, *et al.*

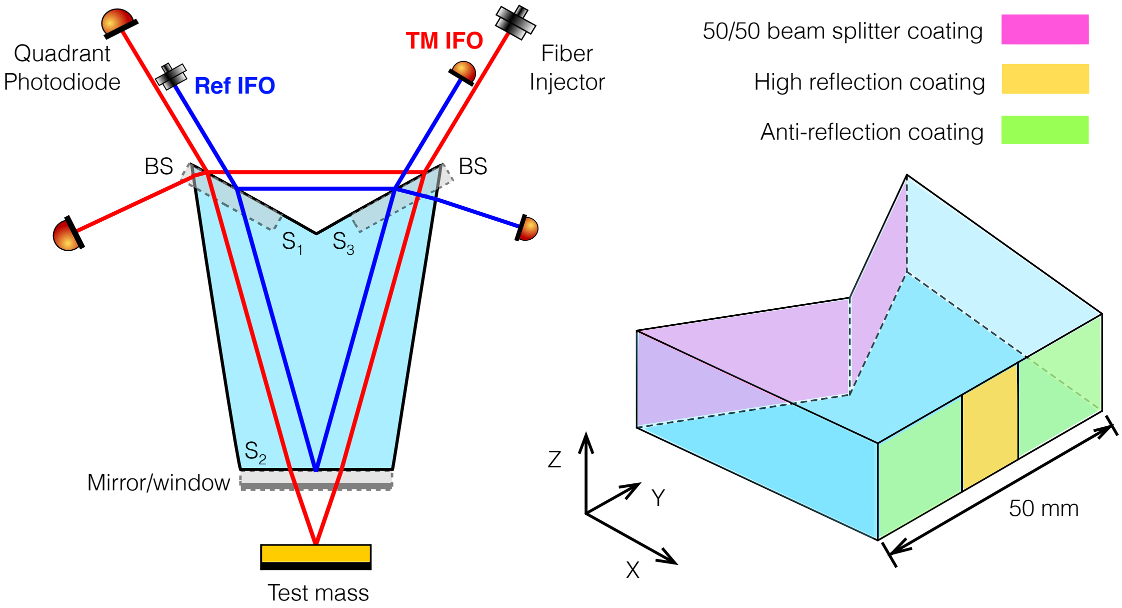

Figure 6.2: Single-element dual-interferometer optical head layout concept design. A frequency-modulated laser beam is split and delivered via two optical fibers to the prism. The prism has three main optical surfaces: S_1 and S_3 are 50/50 beam splitter coatings and are used to split and recombine the laser beams, while S_2 acts as a mirror for the reference interferometer (Ref IFO), and as a window for the test mass inertial sensing interferometer (TM IFO) via the high reflection and anti-reflection coating respectively. For the real use, S_2 = 80 mm. Credits: [109].

is an inevitable noise source (in the 0.1 mHz to 1 Hz regime) due to the unequal arm-length difference of the interferometer, by integrating the differential phase measurements from both interferometers in post-processing,

$$\phi_{\text{tm}} = 2\delta\phi + 2\pi\delta f_0\tau_{\text{tm}} + \sigma_{\text{tm}}, \tag{6.1}$$

$$\phi_{\text{ref}} = 2\pi\delta f_0\tau_{\text{ref}} + \sigma_{\text{ref}}, \tag{6.2}$$

$$\phi_{\text{tm}} - \frac{\tau_{\text{tm}}}{\tau_{\text{ref}}}\phi_{\text{ref}} = 2\delta\phi + \sigma_{\text{tm}} + \frac{\tau_{\text{tm}}}{\tau_{\text{ref}}}\sigma_{\text{ref}}, \tag{6.3}$$

where $\delta\phi$ is the phase shift due to the TM longitudinal motion, scaled by a factor of approximately 2 due to the reflection setup; δf_0 is the laser frequency noise; τ_{tm} and τ_{ref} are the time delays due to the geometric optical pathlength difference between the short and long arms in the TM IFO and Ref IFO, respectively. The σ_{tm} and σ_{ref} terms represent additional noise sources. The frequency noise cancellation is limited by the accuracy of the ΔL measurements and the absolute length of the arm mismatch in the ref IFO (as bigger the mismatch, as better laser frequency noise

Parameter	**Value**
TM IFO intra-prism pathlength (mm)	212.53
REF IFO intra-prism pathlength (mm)	156.55
TM IFO arm-length difference (mm)	500.55
REF IFO arm-length difference (mm)	143.98
S_2 to TM surface distance (mm)	180.88
AOI to the TM (deg)	9.71

Table 6.1: Geometrical parameters relevant to the structural analysis and noise investigations. AOI: angle of incidence.

couples in and can be stabilized), obtained by measuring the effective modulation index m, as described in section 4.3. Having this frequency noise suppressed by combining the signals from the TM and Ref IFOs, the main noise sources are thermal (optics thermal expansion, refractive index variations, or fiber injector jitter), electronic and optical (stray light noise, and cross-coupling of test mass tilt into the length measurement). For the future TMitM 2.0 using the SEDI (see section 7.3), two of these custom-designed prisms are going to be used. Appendix D.4 shows the SEDI's optical head design and several photos of the interferometer taken with a camera and a digital microscope model VHX-7000 where it can be seen the high reflection coating and some minor imperfections (orders of micrometer) on the glass surface.

6.2.1 SEDI manufacturing imperfections

Dealing with manufacturing tolerances and imperfections is expected in any complex optics experiment. Relative alignment errors between the three optical surfaces of the optical head (OH) can cause a bad overlap between the interferometer arms and lead to poor interferometric contrast, which has been observed in both SEDIs: SEDI 1, which will be used for TM control and DFM measurements (see section 6.3), has a maximum contrast of 85%, whereas SEDI 2, which will be used for the SEDI DC Balanced readout experiment (see section 6.4), has a measured contrast of 40%. Using the interferometer simulation software Ifocad [90], it is possible to simulate manufacturing tolerances (values not shown) and imperfections and optimize the prism geometry.

Some important geometrical parameters are given in Table 6.1, whereas nominal parameters used in the simulation are listed in [109]. Fig. 6.3 shows ghost beam suppression in test mass interferometer (TM IFO) and reference interferom-

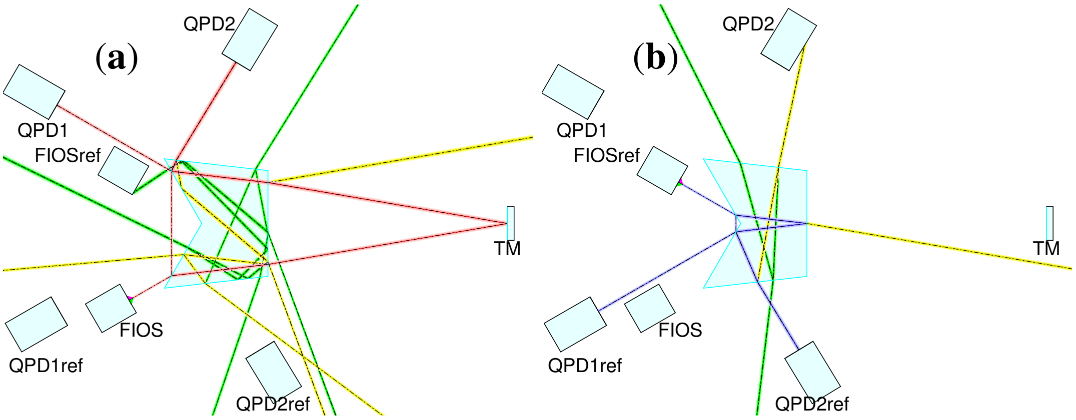

Figure 6.3: Ghost beam suppression in test mass inertial sensing interferometer (TM IFO) (**a**) and reference interferometer (Ref IFO) (**b**). The relative angle between the two side surfaces of the prism is the biggest driver of the amount of stray light directed toward the detectors; therefore, via simulation, this angle is optimized where ghost beams down to a certain power threshold are kept from impinging the detectors. The nominal beams of the test mass and the reference interferometer are shown in red and blue, respectively, in the already optimized optical head. This plot represents ghost beams at the 10^{-3} (yellow) and 10^{-7} (green) relative power levels. Credits: [109].

eter (Ref IFO), where a beam tracing routine was used to propagate the beams within the optical system formed by the fiber injectors, the OH, and the QPDs. A ghost beam having perfect overlap with the nominal beam and having an optical power above $3.5 \cdot 10^{-11}$ relative to the nominal beam power could cause instabilities at the picometer displacement level; therefore, it is important to suppress ghost beams or stray light effects in the setup geometry. It was found that the relative angle between the two side surfaces of the prism is the biggest driver of the amount of stray light directed toward the detectors. By tuning this angle and inspecting the resulting set of ghost beams, it is possible to choose a geometry that guarantees suppression of stray light to a considerable degree.

In [109], it is explained and analyzed in detail geometrical errors injected into the OH model where it was found that relative alignment errors between the optical surfaces, parameterized by angles α and γ (Figure 6.4a); and deviations from perpendicularity of the optical surfaces relative to the base of the prism (Figure 6.4b) are the critical parameters which most affect to the performance of the prism.

During the alignment of both prisms, geometrical errors affecting the relative alignment between optical surfaces were not observed. Nevertheless, as written before, both SEDIs have different interferometric contrasts. Since it is complicated to observe manufacturing imperfections affecting the perpendicularity of the optical surfaces, even with the digital microscope, it is assumed that both SEDIs

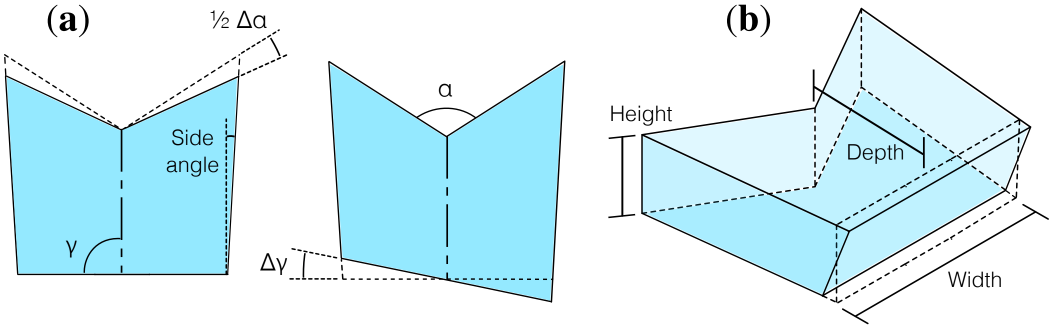

Figure 6.4: Critical manufacturing tolerances are divided into two categories where only one has been observed. Tolerances affecting the relative alignment between optical surfaces, which are parameterized by α and γ, lead to in-plane beam misalignments that can be compensated for in both interferometers by tuning the direction of the incident beams; nevertheless, tolerances affecting the perpendicularity of the optical surfaces with respect to the prism base cause off-plane beam misalignments and result in an unavoidable loss of interferometric contrast which is already confirmed with the measured contrast in both SEDIs where one of them has less contrast than the other. Credits: [109].

have different surface perpendicularities with respect to the prism base, which is extremely difficult to compensate for.

Fig. 6.5 shows a Monte-Carlo simulation where injected errors in the form of deviations from perpendicularity into all three optical surfaces following a uniform distribution showing that the TM IFO performs better than Ref IFO, which was observed when one of the SEDIs was mounted for DFM test (see section 6.3), because S_2 acts as a window for the TM IFO and its perpendicularity has little effect on this interferometer. Simulations show that deviations of up to 0.1 degrees from perpendicularity are allowable while maintaining the interference contrast greater than 14% in Ref IFO and greater than 28% in TM IFO; therefore, observing the different contrast in both manufactured SEDIs, the maximum deviation from perpendicularity in SEDI 2 has to be greater than 0.1 degrees.

In [109], the main noise sources of the SEDI inertial sensor are described in detail, which is mainly the laser frequency noise due to the unequal arm lengths. Although this noise source is mitigated by the dual interferometer configuration using Eq. 6.3, the second noise source is thermal noise, which can be particularly strong in optical setups like the SEDI sensor. Thermal noise typically arises from mechanical changes from thermal expansion and alterations in the refractive index. The latter is particularly crucial in this experiment, given the considerable optical path length within the prisms of the interferometers' long arms. However,

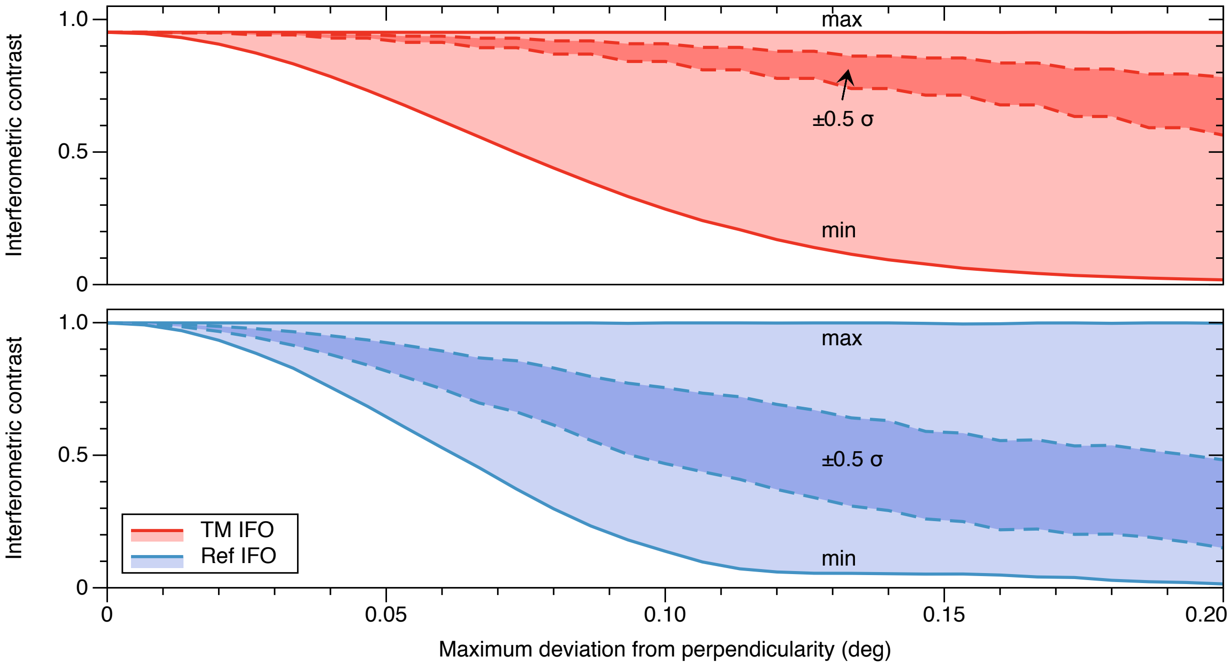

Figure 6.5: Sensitivity to manufacturing imperfections affecting the perpendicularity of the optical surfaces is shown in the interferometric contrast of the reference and test mass interferometer. The dark-shaded area bordered by dashed lines corresponds to ±0.5 σ, while the light-shaded region is bordered by continuous lines representing the maximum and minimum of the distribution. It was observed both SEDIs used for the DFM and DC balanced have different contrasts, which leads to think one of the SEDIs has a bigger deviation from perpendicularity than the other one. Credits: [109].

as thermal and laser frequency noise have no correlation, eliminating both of them simultaneously is usually not feasible.

6.3 DFM preliminary results using SEDI

To test the working principle of the SEDI using DFM, one of the prism was assembled in an aluminium breadboard as is shown in Fig. 6.6 surrounded by a multi-layer insulation foil attached in thin aluminium thermal shields. The experimental set-up is shown in Fig. 6.6a: a fiber-based laser (TLB 6821 from Newport, already seen in 5.3.4 with a laser power of 20 mW maximum) preparation is used to divide, via a 50:50 fiber splitter, a beam feeding the reference and test mass interferometer. The test mass mirror was mounted on a PZT-actuated mount, whereas four single-element photodetectors were used to measure the interferometric signal given by the reference and test mass interferometers. A contrast of more than 85% was measured in both interferometers after alignment. The photodetector signals are digitized using a data acquisition (DAQ) card with a sampling rate of 250

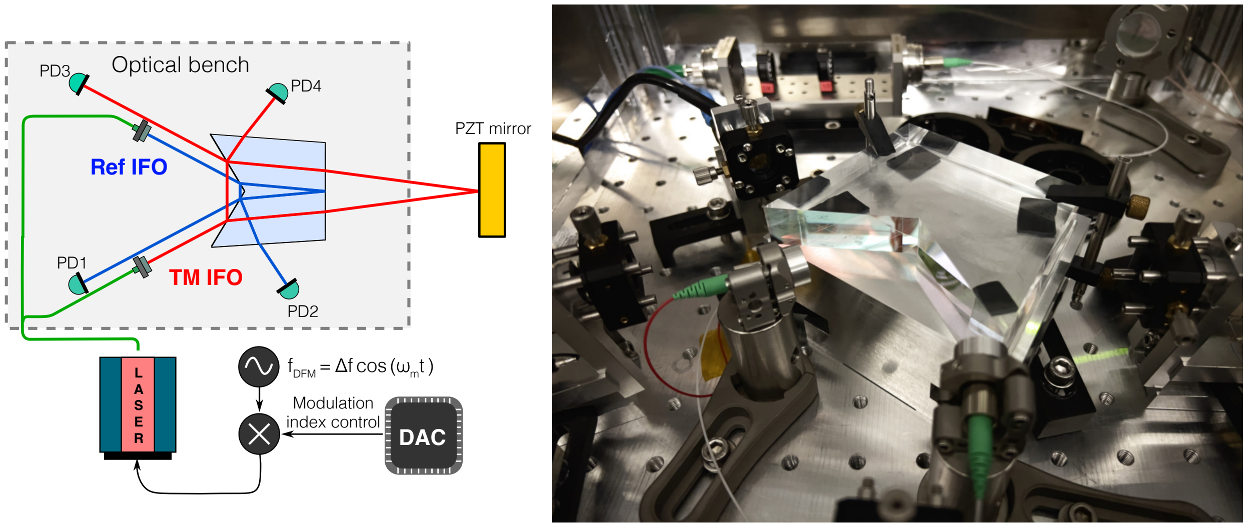

(a) SEDI DFM test layout.

(b) SEDI DFM test photography.

Figure 6.6: (a) Optical layout of the DFM test using the SEDI. (b) Photography of the experiment. Four single-element PDs were used for the TM and Ref IFO. Also, a 1” mirror mounted in a Polaris kinematic mirror mount with three piezoelectric adjusters (POLARIS-K1S3P) was used for future test mass control readout. The measured contrast was about 85% for both Ref and TM IFO.

kHz per channel. During the acquisition, it was used a modulation frequency of $f_m = 1$ kHz and an effective modulation depth of $m_{ref} \approx 7.6$ and $m_{TM} \approx 21$ for the reference and test mass interferometer, respectively. Electronic noise can be measured by subtracting the two-phase readouts generated by electronically splitting one photodetector output and feeding it into two DAQ channels (channels 0 and 2 for PD1 and channels 1 and 3 for PD2, respectively), where the subtraction of the phases from two identical channels (theoretically) combines to zero:

$$\varphi_{0^-} = \varphi_{Ch_{0,1}} - \varphi_{Ch_{2,3}} \approx 0 \tag{6.4}$$

Optical π−measurements are measured by comparing the noise floor between the two complementary optical signals generated in the SEDI and being readout by two photodetectors:

$$\varphi_{\pi} = \varphi_{Ch_{0,1}} + \varphi_{Ch_{2,3}} \approx \pi \tag{6.5}$$

The phase performance, φ, which measures the expected displacement sensitivity and linearity of the readout from the fit algorithm, is shown as phase spectral densities in Fig. 6.7. The blue and orange lines directly represent the reconstructed

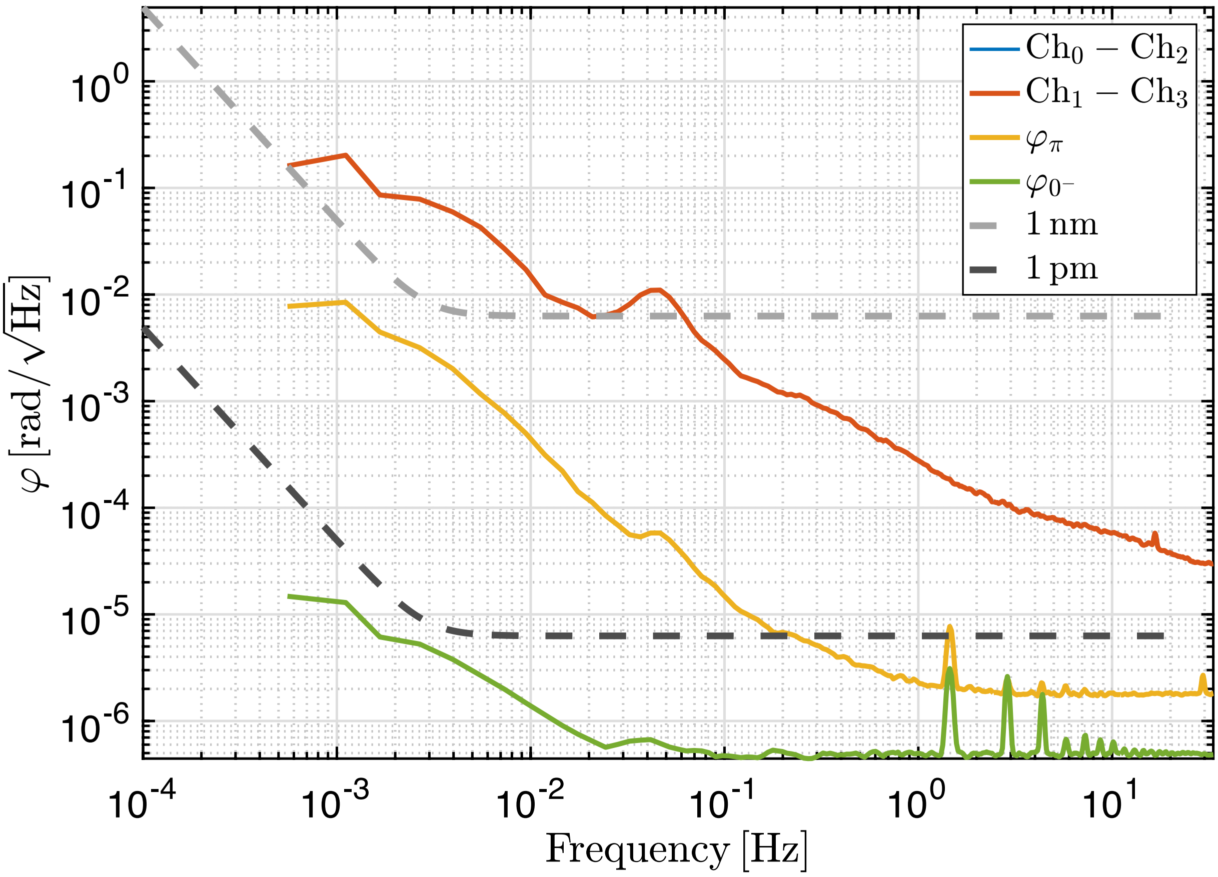

Figure 6.7: Spectral densities of the phase determined from the frequency domain fit algorithm with the modulation parameters f_m = 1 kHz, and an effective modulation depth of $m_{ref} \approx 7.6$ and $m_{TM} \approx 21$ for the reference and test mass interferometer, respectively. The blue and orange lines, representing the DAQ channels split for channels 0, 1 and 2, 3, respectively, are overexposed, and they correspond to the interferometric outputs of the SEDI. The residuals between two measurements, which are electronically split, are given by φ_{0^-} (green line), whereas the residuals of the π-combination are given by φ_π (yellow line). As a reference, it also plots the typical 1 pm requirement for the displacement sensitivity aimed at LISA and the 1 nm noise line.

phase outputs for the SEDI sensor. Since the entire setup is on air, surrounded by thin thermal shields, both channel outputs show the expected influence of thermal noise below 1 Hz. Hence, interferometers reaching sensitivities of 1 $\mathrm{pm}/\sqrt{\mathrm{Hz}}$ below 1 Hz are typically operated in a vacuum environment where it maintains higher thermal stability. Based on this, it is assumed that thermal fluctuations, air density changes, and laser frequency noise largely dominate the low-frequency noise. However, φ_{0^-} and φ_π are important because they give an insight into the presence of other limiting noise sources. The zero combinations for both interferometers, given by the green line in Fig. 6.7, show a white noise floor above 100 mHz of 0.5 μrad/$\sqrt{\text{Hz}}$, which is most probably ADC digitization noise usually present at these levels manifesting small residuals at 1.5, 2, and 3.5 Hz, probably due to slight differences in the detection bandwidth of the DAQ system, leading to non-linearities in the zero combination φ_{0^-}.

The π-combination, φ_π, is plotted as yellow line in Fig. 6.7. The white noise floor of this combination is not plotted, but it is probably on the same order of magnitude as for the zero combinations. It is well known the π-combination is not sensitive to either displacement noise, laser frequency noise, or non-sinusoidal frequency modulations because (except for a phase shift of π) both beams contain the same interference. At 200 mHz, this combination achieves a performance of 6 μrad/$\sqrt{\text{Hz}}$, which corresponds to a displacement noise of 1 pm/$\sqrt{\text{Hz}}$ (except for some peaks also visible in the zero combination φ_{0^-}) leading to a performance of 8 mrad/$\sqrt{\text{Hz}}$ at 1 mHz. This increased phase noise in low frequencies is explained again as the expected thermal noise below 1 Hz. An amplitude stabilization scheme is expected to be implemented soon, which would lead to a reduced noise level in the π combination. Since a polarization cleaning stage was implemented before the light injection in the fiber collimators, amplitude fluctuations were not observed.

Following the example of the MZI, phase stability in the SEDI reference interferometer is planned to be improved soon by migrating the current optical setup to a vacuum chamber and surrounding it with passive thermal insulation layers.

6.4 Laser frequency stabilization via SEDI prism and balanced DC readout

With the experience gained in the DC-balanced readout experiment using the MZI (see 5.4) and [110], the entire setup was used to reproduce the DC-balanced readout using another of the SEDIs (since the other one was busy with the DFM tests) in order to test the interferometer stability. Due to space constraints, only the Ref IFO was used. The experimental setup is shown in Fig. 6.8. Light from a 1064 nm non-planar ring oscillator laser (laser B) is split two ways, with one part being fed to a vacuum chamber containing the SEDI prism and the remaining part being interfered with a reference 1064 nm laser (laser A) that is locked to a molecular iodine hyperfine transition (R(56)32-0 ‘a1’). Inside the vacuum chamber, the light is first injected into a small bench where a combination of retarder waveplates and a polarizer produces S-polarized light. A small portion of the light is captured by an auxiliary photodiode and used to stabilize the laser amplitude. The rest is

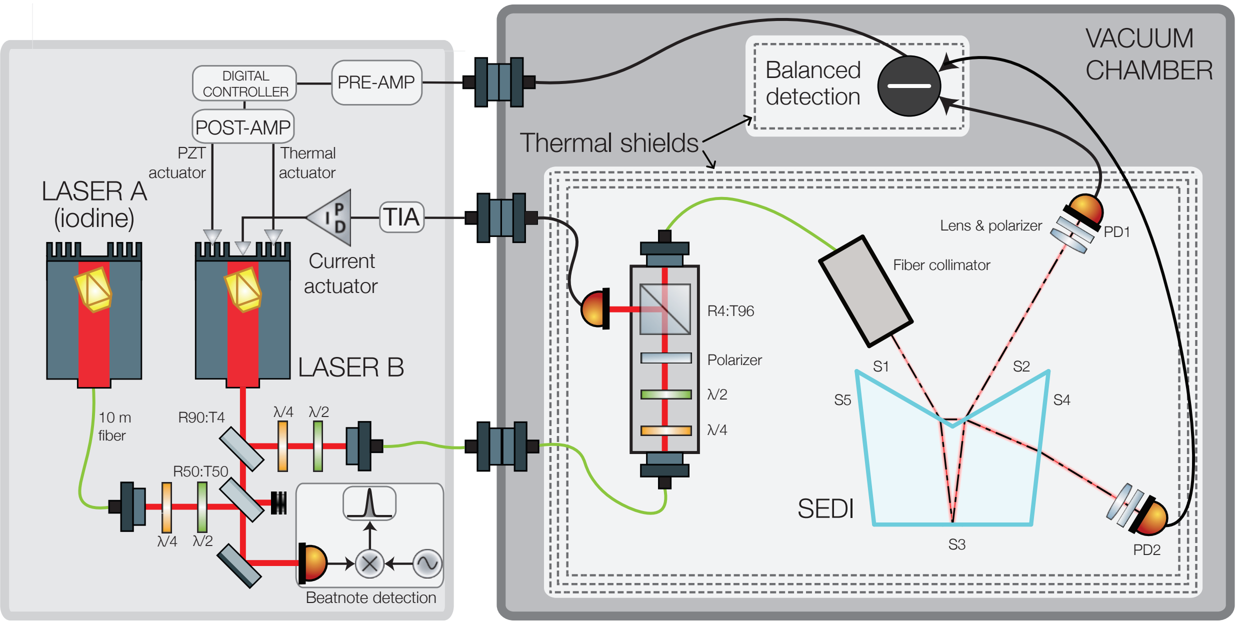

Figure 6.8: Experimental setup. The single-element dual-interferometer (SEDI) prism is surrounded by thermal shields and placed inside a vacuum chamber along with auxiliary optics for polarization adjustment and amplitude stabilization. A commercial fiber collimator is used to inject a beam derived from laser B into the SEDI reference interferometer. Two photodiodes are placed at the complementary output ports of the interferometer, with a focusing lens and thin film polarizer placed in front that help mitigate known noise sources. The difference current between the two photodiodes is converted to a voltage via a low-noise low-drift transimpedance amplifier. The amplifier signal is filtered, digitized, and used as input in a digital PI controller to derive a control signal that is fed back to laser B's fast and slow actuators, thereby transferring the interferometer's path length stability to the laser frequency. A beatnote signal in the order of a few GHz is obtained by interfering laser B with a second, more stable laser (laser A). The beatnote signal is mixed down to below 100 mHz using an ultra-stable GHz source and read by a micro-cycle-stable phasemeter to characterize the achieved stability.

coupled back into a fiber and injected into the SEDI prism's Ref IFO via a commercial fiber coupler. All of the components mentioned above are mounted on an aluminium breadboard and surrounded by a high-performance multi-layer thermal shield similar to the one described in 5.3.2.

The photodiodes are operated in reverse bias voltage and connected in a balanced differential trans-impedance amplifier (TIA) performing a direct current subtraction, giving rise to a signal with sinusoidal dependence on the laser frequency and the interferometer's pathlength noise. A focusing lens is placed in front of each photodiode to minimize transverse beam walk, and thin-film polarizers with high extinction ratios are placed after the lens to mitigate the impact of stray light of wrong polarization. Balanced operation is obtained by adjusting the polarizer's

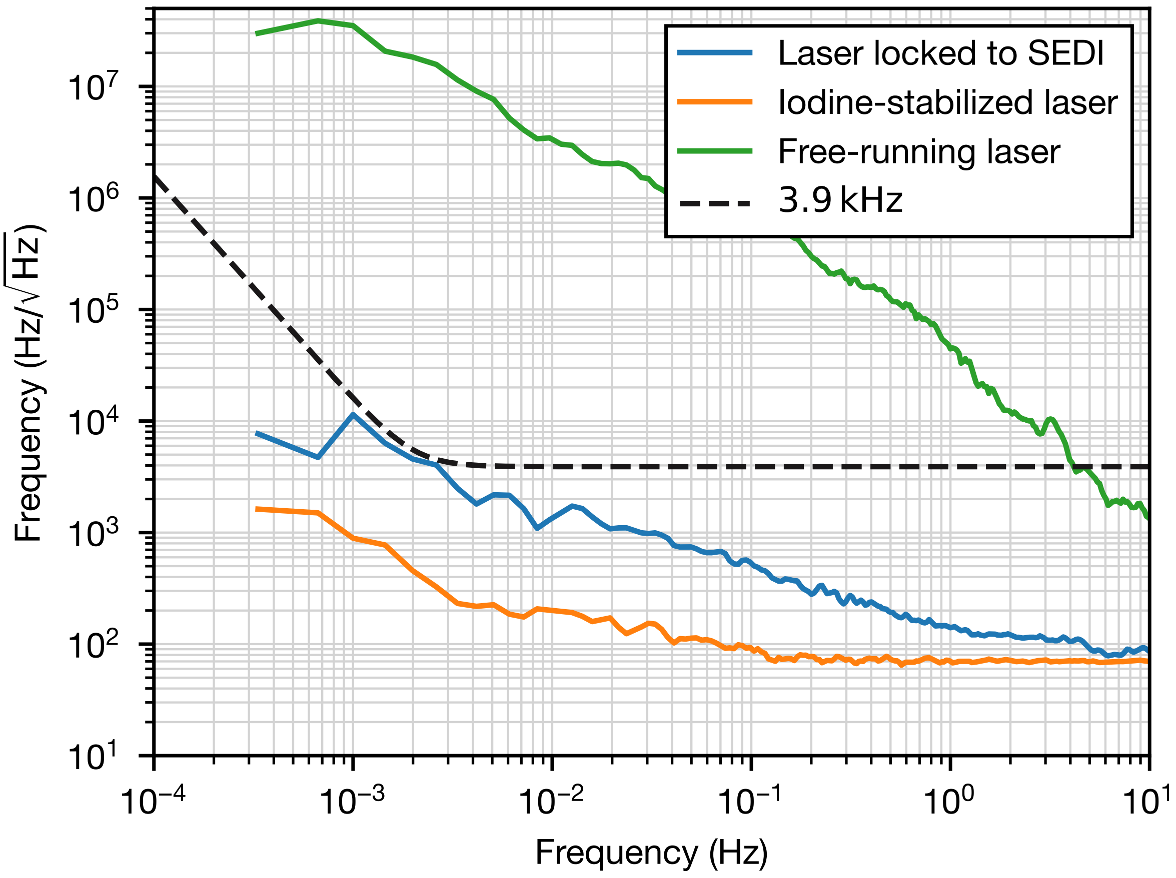

Figure 6.9: Frequency spectral densities of laser B when it is free-running (green), laser B when it is locked to the SEDI reference interferometer (blue), and laser A, which is used as reference (orange). The picometer-equivalent frequency noise for a 14.4-cm interferometer is represented by a black dashed curve at $3.9\,\mathrm{kHz}/\sqrt{\mathrm{Hz}} \times u(f)$.

rotation angles such that both photodiodes receive the same amount of laser power at the mid-fringe operating point. A separate thermal shield surrounds the TIA to avoid temperature cross-couplings between the optics and electronics, and the TIA output signal is low-pass-filtered and enhanced by a pre-amplifier before being digitized by a Moku:Lab instrument and used as an error signal in a digital PI-controller. The resulting control signal is filtered by a post-amplifier and fed back to the laser via a slow thermal actuator and a high-speed piezo-electric transducer actuator. The beatnote between lasers A and B is in the GHz regime. Thus, it is down-mixed to below 100 MHz by an ultra-stable GHz signal generator (SMB100A by Rohde & Schwarz) before being read out by a Moku:Lab instrument acting as a phasemeter.

The frequency spectral density [72] and modified Allan deviation [107] of the

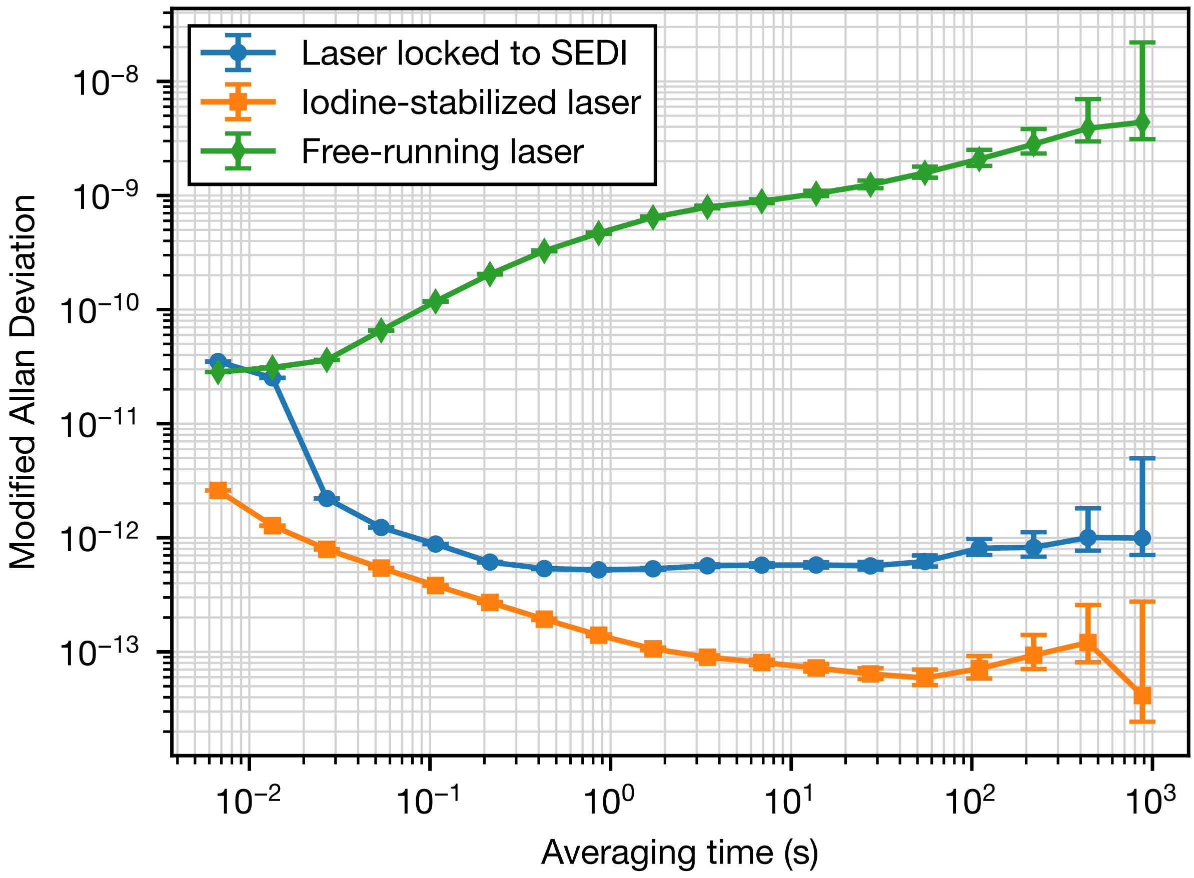

Figure 6.10: Modified Allan deviations of laser B when it is free-running (green), laser B when it is locked to the SEDI reference interferometer (blue), and laser A (together with another iodine-stabilized NPRO laser), which is used as reference (orange).

beatnote between the laser locked to SEDI and the iodine-stabilized reference laser are shown in Fig. 6.9 and 6.10 respectively for a typical 1-hour measurement at a rate of 150 samples per second (blue curves). Also shown is the free-running noise of the laser (green) and the noise of the reference laser (orange) when it was measured using two iodine-stabilized NPRO lasers. Given an arm-length difference of Δl=144 mm, Eq. 5.7 can be used to determine the effective displacement noise δl, which by reversing this calculation, the frequency-noise level is given by

$$\delta f = \frac{\delta l \cdot c}{\Delta l \cdot \lambda_0} = 1.957\,\mathrm{kHz}/\sqrt{\mathrm{Hz}} \tag{6.6}$$

As usual, for achieving a displacement noise of $\delta l = 1\,\mathrm{pm}/\sqrt{\mathrm{Hz}}$, when consid-

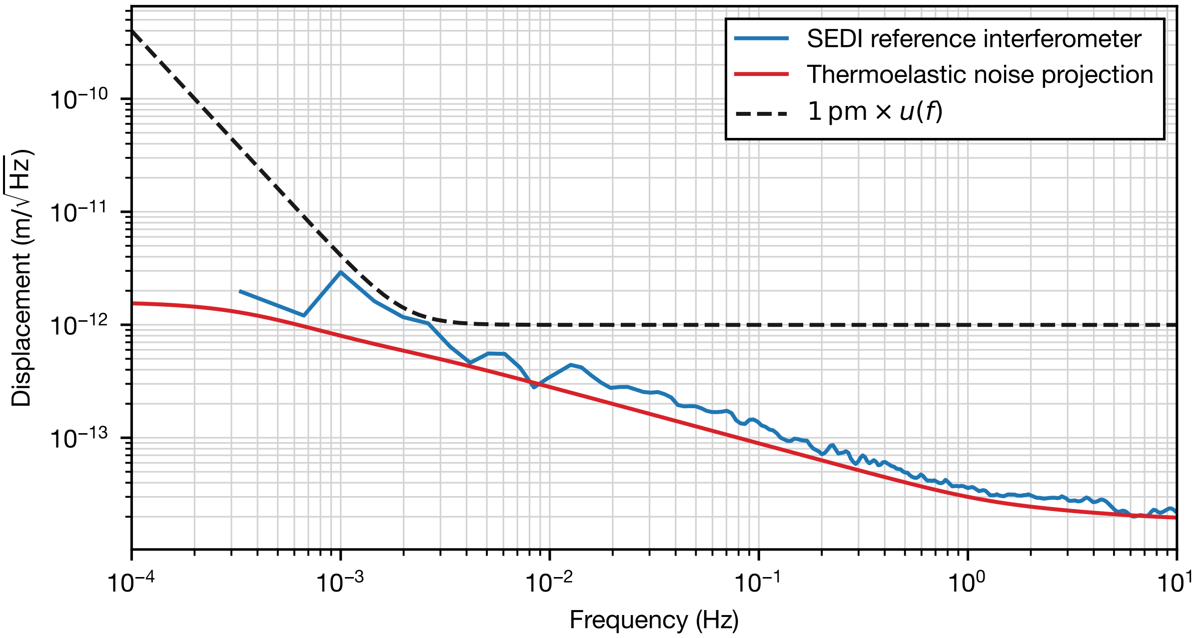

Figure 6.11: Amplitude spectral density of the SEDI reference interferometer pathlength (blue) and projection of the thermoelastic noise (red). A displacement noise of 1 pm/$\sqrt{\text{Hz}}\times u(f)$ is represented by the black dashed curve.

ering reflection setups, the inclusion of geometry provides an additional factor of approximately two, resulting in a frequency noise level of about 3.914 kHz/$\sqrt{\text{Hz}}$, representing the picometer-equivalent frequency instability of an interferometer with 144 mm arm length difference scaled by Eq. 4.3, which is shown in figure 6.9 (black dashed line).

Fig. 6.9 and 6.10, which provide largely the same information, reveals that the noise of the reference laser (laser A) is low enough compared to the laser under test (laser B), that its instability can be neglected in the estimation of the noise of the unit under test. The laser locked to the SEDI prism presents a fractional frequency instability below the 10^{-12} level for averaging times between 0.1 and 1000 seconds. This performance is similar to what can be expected from high-performance iodine-stabilized reference systems. The measured fractional frequency instability is converted into equivalent pathlength noise by invoking

$$\frac{\Delta(l_{\text{ref}})}{l_{\text{ref}}} = \frac{\Delta f}{f_0}, \tag{6.7}$$

where f_0 is the average laser frequency (roughly 282 THz). The resulting pathlength noise is shown in Figure 6.11, together with a projection of thermoelastic noise obtained via numerical modeling, using the model described in [109] and assuming a uniform temperature distribution of $20\,\mu\mathrm{K}/\sqrt{\mathrm{Hz}}$ spectral density in the surface of the prism, which is consistent with the measurements of the temperature inside the vacuum chamber (i.e, Fig. 5.10). Better performance is expected once the SEDI is installed or bonded in an ultra-stable baseplate with FIOS instead of commercial collimators (see section 7.3).

Part IV

Future Work & Conclusion

Chapter 7

Future work

7.1 Six DoF optical lever TM readout

Six-degree-of-freedom sensing with high precision is crucial for upcoming gravitational space missions and tabletop ground-based experiments like torsion balances if one wants to test on-ground gravitational reference sensors. Performing measurements across all six degrees of freedom for a TM is essential to mitigate the cross-coupling noise, frequently a significant limiting factor in performance. In [111], it is described as a six-degree-of-freedom interferometer system based on multiplex differential wavefront sensing and longitudinal pathlength sensing, which, compared to conventional capacitive sensing or optical levers, has a higher measurement accuracy. Nevertheless, all interferometric readout systems, compared with the simplicity of the optical levers, are not straightforward to implement in a vacuum chamber in combination with the torsion balance for test mass readout. Therefore, the optical lever geometry already introduced in Chapter 3 will be extended by an additional degree of freedom that senses the vertical motion of the TM to realize an all-optical six-DoFs TM sensor. In this new geometry, a novel diamond-shaped TM, as depicted in Fig. 7.1a, was designed and built in an ultra-stable aluminium structure containing the TM and four vacuum-compatible QPDs and collimators, as is shown in Fig. 7.1b. The six-DoFs optical lever still needs to be tested and implemented in the vacuum chamber, where a better sensitivity is expected as noise sources such as temperature fluctuation or acoustic coupling will be smaller than in-air measurements.

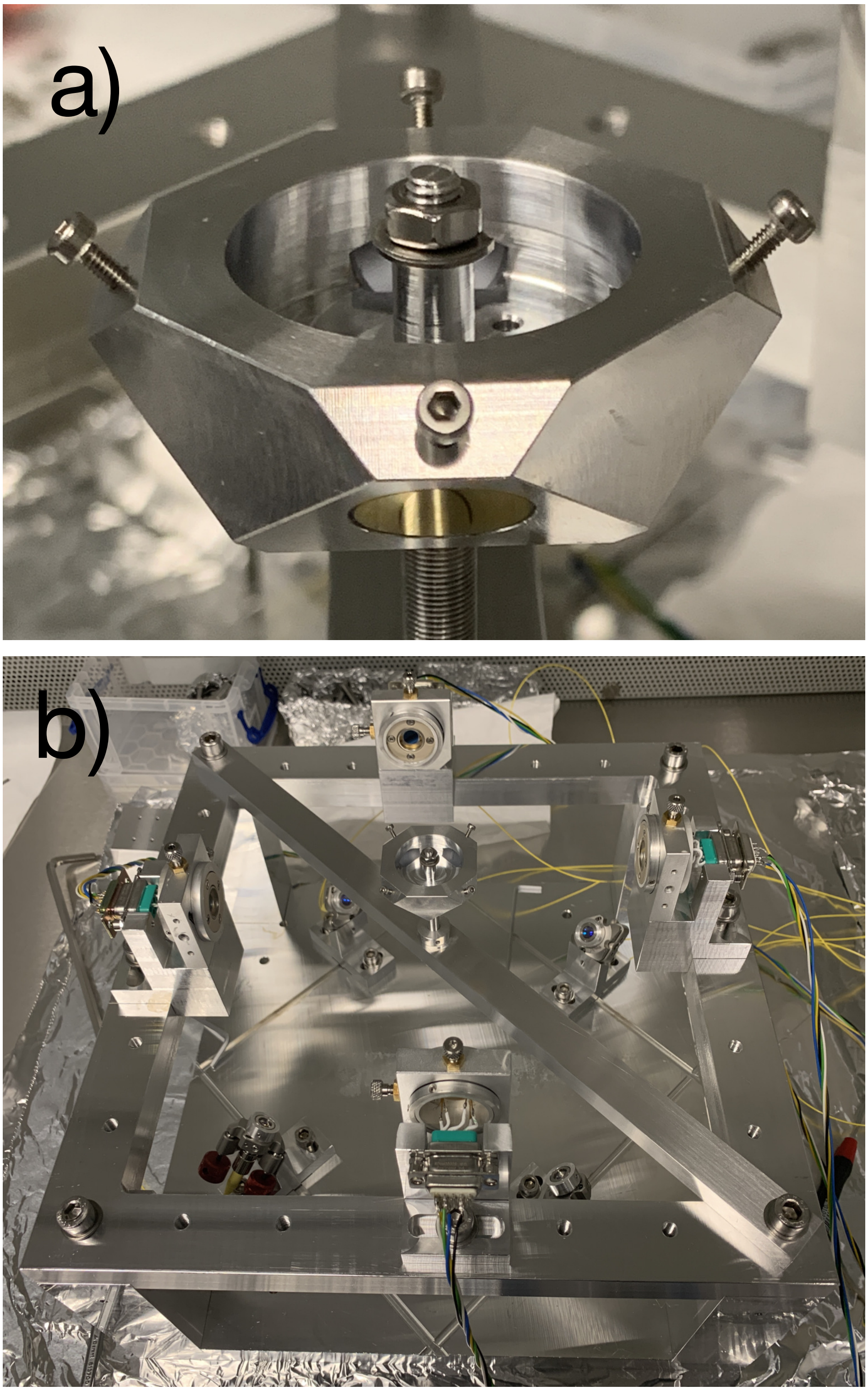

Figure 7.1: (a) Photography of the Diamond shape already built and installed in the aluminium structure. With this novel design, the optical lever will have an additional degree of freedom that senses the vertical motion of the TM. (b) Photography of next-generation optical lever readout sensor able to measure 6-DoFs. The diamond-shaped TM, the new vacuum-compatible photodetectors, and the new commercial fiber collimators F110APC-532 from Thorlabs.

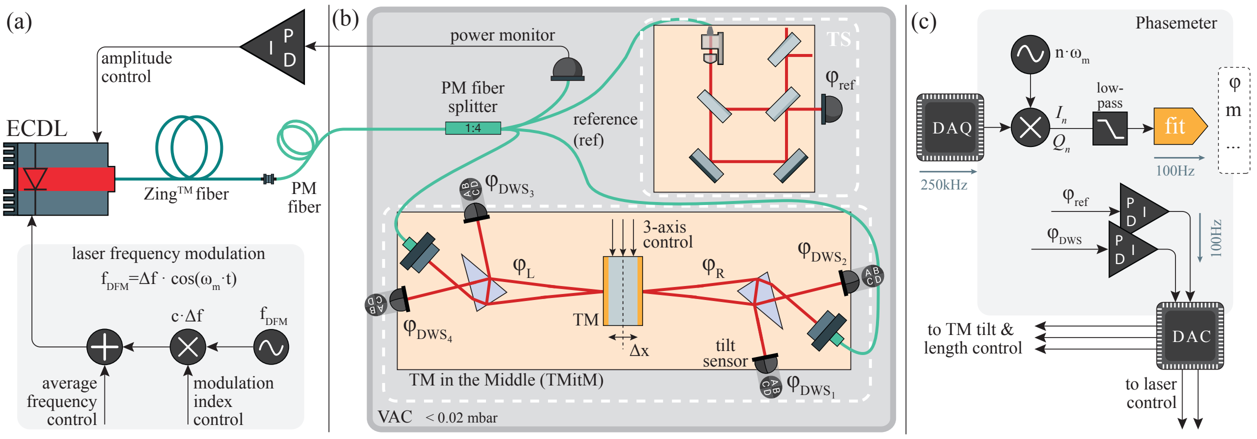

Figure 7.2: Sketch of the planned TMitM experiment upgraded, based on [87], where shows the laser preparation (a) consisting in a fiber-coupled external-cavity diode laser (ECDL) where is applied a deep frequency modulation f_{DFM}. (b) shows the vacuum chamber (VAC), which will house two 3-layer thermal shields (TS) that cover two quasi-monolithic interferometers: the well-known reference MZI (ref) with the FIOS and the test mass in the middle (TMitM). The data-acquisition (DAQ) system has eight analog inputs that are simultaneously digitized and processed in a software phase meter, both shown in inset (c). Analog control voltages are provided by a digital-to-analog converter (DAC) and are used to actuate on the laser and the test mass (TM). Credits: K.S. Isleif.

7.2 Test Mass in the Middle future upgrade

In chapter 5 it was described the upgrades in the MZI, originally built by O. Gerberding and K.S. Isleif, consisting of the FIOS and a novel three-layer thermal shields which reached a displacement noise below the $1\,\mathrm{pm}/\sqrt{\mathrm{Hz}}\cdot u(f)$. One of the successful experiments with the original MZI was the ”Test Mass in the Middle” (TMitM), where it was demonstrated a displacement-sensing performance of DFM on the $1\,\mathrm{pm}/\sqrt{\mathrm{Hz}}$ level, as described in [87] and where the MZI was used as a reference interferometer. The TMitM consisted of a 4-mm-thick mirror that is gold coated on both sides and mounted on a three-axis piezotransducer (PZT) glued in the center of a glass ceramic Clearceram optical bench (OB). Two interferometers, with a triangular base surface with two equal sides of about 25 mm in length, one on each side of the TM, allowed to perform two redundant interferometric measurements of the same TM motion.

The original experiment was performed with an 8-channel data-acquisition card with a 250 kHz sampling rate, used to digitize the photodiode voltages generated from the photocurrents via transimpedance amplifiers. The tilt of the TM in the horizontal and vertical directions was controlled by actuating on the three-axis PZT mount. As an error signal, a differential-wave-front-sensing (DWS) measure-

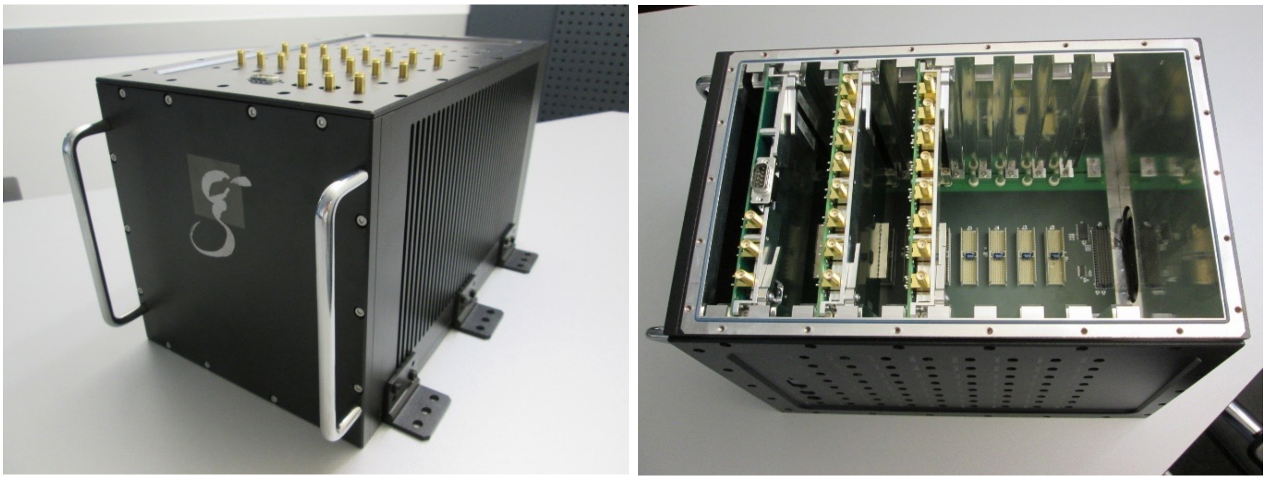

Figure 7.3: Photography of next-generation multi-channel phase readout instrument, able to process up to 64 independent readout channels. Credits: J.J. Esteban

ment was used, provided by quadrant photodiodes (QPDs). Nevertheless, the limited number of readout channels allowed only one QPD during the displacement-performance measurements, which was used to suppress TM tilts actively.

With time, two more transimpedance amplifier boxes based on the previous existing one were built, having a total of 26 channels available. Also, two more 8-channel DAQs were purchased, meaning that an upgrade of the TMitM using four QPDs (16 channels in total, plus 3 channels for the MZI) is now possible. Fig. 7.2 shows a sketch of the planned TMitM experiment upgrade, which consists basically of two interferometers: the well-known reference MZI (ref) (this time with the FIOS as a fiber injector), which will be used as a frequency reference, and the TMitM, both of them covered by the thermal shields described in section 5.3.2. Increasing the number of channels would improve the accuracy of the error signal used to actuate on the three-axis PZT mount and monitor the out-of-loop behavior of the TM tilts, having this time enough signals to stabilize the laser frequency and modulation or the TM path length. Also, it will be a good test for the in-house phasemeter, which will be used in LISA. Currently, a custom-designed phasemeter has been built as the first demonstrator of a multi-channel phase readout instrument, as seen in Fig. 7.3, able to process up to 64 independent readout channels, enabling real-time digital signal processing and control functions. Once the DFM algorithm is programmed in the phasemeter, it will be an excellent test for the upgraded TMitM.

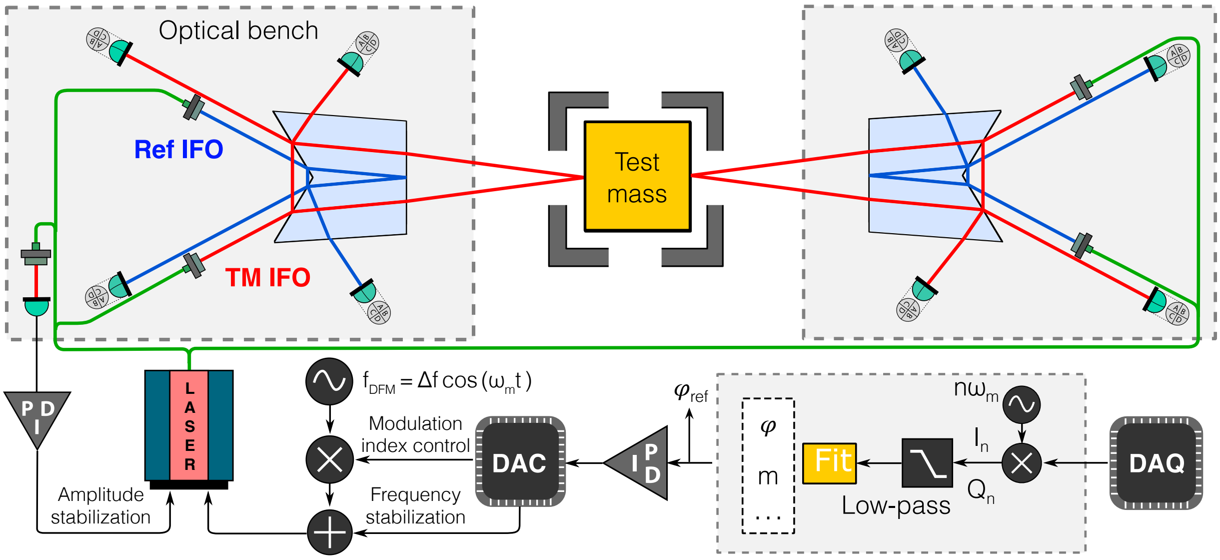

Figure 7.4: Planned design layout of the single-element dual-interferometer (SEDI) experiment. A cubic test mass is probed from opposite sides by a pair of heptagonal prism optical heads fed from a single frequency-modulated laser source. Each optical head hosts two interferometers, one reading the displacement of the test mass and another acting as a frequency reference. The deep frequency modulation (DFM) interferometric signals will be captured by photodiodes, digitized, and processed by a phasemeter. The phase measurement of the reference interferometer will be used as a control signal for the laser's frequency and modulation index and as a calibration signal for the test mass displacement measurement. Credits: [109].

7.3 Test Mass in the Middle 2.0 (with SEDI)

In chapter 6, the SEDI was described as a new interferometer with a novel topology that includes the reference and TM interferometer in the same optics. Fig. 7.4 shows a planned experiment layout based on the TMitM experiment and the SEDI, where a test mass is probed from opposite sides by a pair of SEDI detectors. The same layout applies to any number of SEDI sensors probing any degrees of freedom of one or multiple test masses simply by scaling the required fiber injectors and phasemeter channels. Since the frequency modulation depth applied to the laser beam must be at the GHz level to reach sufficient modulation depth in centimeter-scale setups such as SEDI, the best current option will be the external cavity diode laser TLB 6821 from Newport, already seen in 5.3.4. The photodiodes are based on InGaAs with a small active area diameter of 0.5 mm to achieve high bandwidth and interferometric contrast, which were introduced in section 5.3.5. The signals will be subsequently digitized using a data acquisition system with a sample rate of 250 kHz, where the digital signals are demodulated by a software phasemeter that decimates the data rate down to 100 Hz and implements the non-linear DFM fit algorithm. Fig. 7.5 shows a photograph of both SEDI's

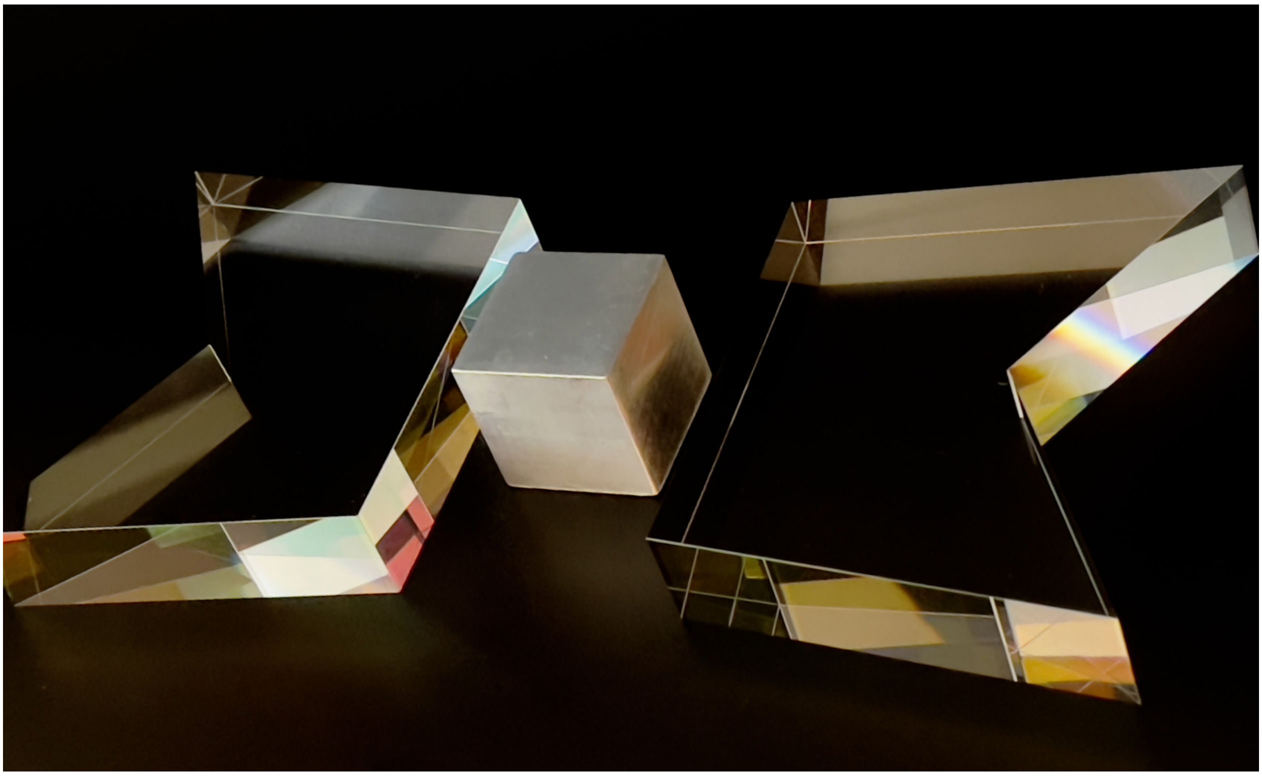

Figure 7.5: Photography of two SEDIs and a TM mock-up. Both SEDI's are not expected to be 100% the same due to small manufacturing tolerances and imperfections. For SEDI 1, the maximum contrast was 85%. For SEDI 2 (the one used for the SEDI DC balanced experiment), it reached 40%.

(together with a TM mock-up), which will be used for different purposes, including DFM and DC balanced readout, already seen in sections 6.3 and 6.4, respectively.

The construction of the new TMitM based on SEDIs is expected to be in the near future, and the test will probably be in the new torsion balance, which is currently being commissioned at Leibniz Universität Hannover (TerraQ) and the Max-Planck Institute for Gravitational Physics (Albert Einstein Institute).

Chapter 8

Summary and outlook

8.1 5-DoF Optical Lever

In chapter 3, it was shown an optical TM readout system based on the combination of four optical levers and quadrant photodiodes. This TM readout system allows for an independent measurement of the five degrees of freedom x_{TM}, y_{TM}, θ_{TM}, ψ_{TM}, and ϕ_{TM} of a cubic TM. These degrees of freedom can be measured simultaneously, and the signal analysis allows the disentangling of TM rotations and translations. This feature was used to reveal cross couplings due to the non-perfect alignment of the setup and the hysteresis introduced by the hexapod. Albeit being a simple and economical device built from off-the-shelf laser diodes and QPDs, this system demonstrated an angular and translational resolution below 600 nrad/$\sqrt{\mathrm{Hz}}$ and 300 nm/$\sqrt{\mathrm{Hz}}$, respectively, at frequencies between 10 mHz and 1 Hz. It was also compared to the rotational sensing performance against a commercial autocollimator, where the angular displacement spectral density yielded a sensitivity of 330 nrad/$\sqrt{\mathrm{Hz}}$ at 100 mHz, which was about an order of magnitude below the simultaneously recorded data from the autocollimator (about 4.2 μrad/$\sqrt{\mathrm{Hz}}$). Furthermore, the better signal-to-noise ratio and higher sampling rate enabled signal analysis at frequencies above 100 mHz, revealing the higher harmonic peaks due to the discontinuous motion of the hexapod.

In the future, a new optical lever readout system, which has been built, will be able to extend an extra degree of freedom and is expected to be tested soon in the torsion balance.

8.2 Mach-Zehnder Interferometer

An ultra-stable Mach-Zehnder interferometer with unequal arm lengths capable of reaching $1\,\mathrm{pm}/\sqrt{\mathrm{Hz}} \cdot u(f)$ from $10\,\mu\mathrm{Hz}$ to $10\,\mathrm{Hz}$ was presented in chapter 5. This Mach-Zehnder is one to two orders of magnitude more stable in the lower frequencies than the previous realization. This stability was achieved by applying two passive techniques to reduce noise sources of thermal origin. First, a quasi-monolithic fiber injector which provides an ultra-stable input beam that is much more robust to temperature changes than what is possible with conventional fiber injectors. Second, a high-performance enclosure provides an ultra-quiet thermal environment, reducing the coupling of temperature-driven effects to path length noise in the interferometer, such as thermoelastic deformation of the baseplate and components and refractive index fluctuations.

A combination of frequency and time domain analysis techniques was used to assess the stability of the MZI-stabilized laser along with two iodine-stabilized reference lasers. The individual stability of each system was disentangled from a simultaneous three-signal measurement using the three-cornered-hat method (3CH). Due to the nature of the involved noise sources, which are white frequency noise at high frequency (i.e., at a short averaging time, τ) and random run noise at low frequency (i.e., at long τ), two different variance functions were used, with one providing greater confidence at short τ (the modified Allan deviation), and one greater confidence at long τ (the Hadamard deviation). The 3CH analyses revealed that the stability of the MZI system is comparable to the two reference systems, which are based on stabilization to molecular iodine hyperfine transitions near 532 nm. The frequency of the MZI-stabilized laser is within the target of $300\,\mathrm{Hz}/\sqrt{\mathrm{Hz}} \cdot u(f)$ for all frequencies above 40 mHz. At frequencies between $10\,\mu\mathrm{Hz}$ and 40 mHz, it is a factor of 1 to 5 less stable. The stability could be improved by increasing the interferometer's arm length difference (e.g., from 7 cm to 40 cm, as in the LTP interferometer) and addressing the associated complexities of the longer optical path length. However, a more exciting prospect is combining the techniques of Mach-Zehnder stabilization and arm-locking [78], which could lead to a frequency stability orders of magnitude better than $300\,\mathrm{Hz}/\sqrt{\mathrm{Hz}} \cdot u(f)$, potentially allowing the requirements on time delay interferometry to be relaxed. Since the reference interferometer can be integrated as part of the optical bench, this technique eliminates the need for a separate laser stabilization subsystem, which makes this an interesting scheme for future gravity missions [38, 112].

8.3 Single-Element Dual-Interferometer (SEDI)

In chapter 6, it was shown the design and construction of the SEDI inertial sensor, theoretically able to measure test mass displacements with a precision greater than 1 pm/$\sqrt{\text{Hz}}$ above 10 mHz. The potential applications of this new sensor cover many areas of science and technology. In experimental gravitational physics and notably in next-generation space-based gravity missions, the SEDI sensor offers a scalable solution for multi-channel test mass readout. Satellites employing drag-free control to trail a free-floating test mass to follow an undisturbed geodesic require measuring the motion of said test mass in several degrees of freedom with high precision and large dynamic range. The reduced size and weight of the SEDI sensor mean that several optical heads can be applied to offer increased sensitivity and redundancy in these measurements, making it a suitable candidate for these applications. The sensor fits in a small package of a few cubic inches and has a single optical component that hosts two interferometers with arms of unequal length. The dual-interferometer configuration allows the SEDI sensor to act as its own reference for laser frequency noise suppression. Due to the intrinsic minimalism of this optical setup, this device can be integrated into an optical readout platform that features multiple optical heads and can interrogate several degrees of freedom of a mechanical system. The perpendicularity of the three optical surfaces has been identified as the most critical manufacturing specification. This parameter has a significant impact on the resulting interferometric contrast, which is a common issue in interferometers employing a single optical element. In fact, it was found that both SEDIs have different interferometric contrasts of 85 and 40%, respectively, due to manufacturing tolerances. Preliminary results of on-air null measurement show a noise floor above 100 mHz of 0.5 μrad/ $\sqrt{\text{Hz}}$. The π measurements show a performance of 1 pm/$\sqrt{\text{Hz}}$ at 200 mHz. It is expected that using a proper amplitude stabilization scheme in combination with a high-performance enclosure, already seen in section 5.3.2, which will provide an ultra-quiet thermal environment, would reduce the noise level in both null and π-measurements. Lastly, using the same DC-balanced readout scheme used in section 5.4, it was demonstrated experimentally that SEDI has a performance of 1 pm/$\sqrt{\text{Hz}} \cdot u(f)$ from 1 mHz to 10 Hz.

Bibliography

[1] Richard P Feynman, Fernando B Morinigo, and William G Wagner. *Feynman Lectures on Gravitation*. Addison-Wesley, 1995.

[2] Qing Li, Chao Xue, Jian-Ping Liu, Jun-Fei Wu, Shan-Qing Yang, Cheng-Gang Shao, Li-Di Quan, Wen-Hai Tan, Liang-Cheng Tu, Qi Liu, Hao Xu, Lin-Xia Liu, Qing-Lan Wang, Zhong-Kun Hu, Ze-Bing Zhou, Peng-Shun Luo, Shu-Chao Wu, Vadim Milyukov, and Jun Luo. Measurements of the gravitational constant using two independent methods. *Nature*, 560(7720):582–588, Aug 2018.

[3] Carlo Rovelli. *Quantum Gravity*. Cambridge University Press, 2008.

[4] Roger Penrose. *The Road to Reality: A Complete Guide to the Laws of the Universe*. Knopf, 2004.

[5] Katherine Freese. *The Cosmic Cocktail: Three Parts Dark Matter*. Princeton University Presss, 2014.

[6] Tobias Westphal, Hans Hepach, Jeremias Pfaff, and Markus Aspelmeyer. Measurement of gravitational coupling between millimetre-sized masses. *Nature*, 591(7849):225–228, Mar 2021.

[7] M Hueller, A Cavalleri, R Dolesi, S Vitale, and W J Weber. Torsion pendulum facility for ground testing of gravitational sensors for lisa. *Classical and Quantum Gravity*, 19(7):1757, mar 2002.

[8] Barry C. Barish and Rainer Weiss. LIGO and the Detection of Gravitational Waves. *Physics Today*, 52(10):44–50, 10 1999.

[9] B. P. Abbott et al. Observation of gravitational waves from a binary black hole merger. *Phys. Rev. Lett.*, 116:061102, Feb 2016.

[10] Alexander McPherson and Lawrence James DeLucas. Microgravity protein crystallization. *npj Microgravity*, 1(1):15010, Sep 2015.

[11] David C. Aveline, Jason R. Williams, Ethan R. Elliott, Chelsea Dutenhoffer, James R. Kellogg, James M. Kohel, Norman E. Lay, Kamal Oudrhiri, Robert F. Shotwell, Nan Yu, and Robert J. Thompson. Observation of bose–einstein condensates in an earth-orbiting research lab. *Nature*, 582(7811):193–197, Jun 2020.

[12] G. Reinhart, D. J. Browne, F. Kargl, F. García-Moreno, M. Becker, E. Sondermann, K. Binder, J. S. Mullen, G. Zimmermann, R. H. Mathiesen, W. H. Sillekens, and H. Nguyen-Thi. In-situ x-ray monitoring of solidification and related processes of metal alloys. *npj Microgravity*, 9(1):70, Sep 2023.

[13] Aleksey Baldygin, Abrar Ahmed, Ryan Baily, Md Farhad Ismail, Muhammed Khan, Nigel Rodrigues, Ali-Reza Salehi, Megnath Ramesh, Sanjay Bhattacharya, Thomas Willers, Derek Gowanlock, and Prashant R. Waghmare. Effect of gravity on the spreading of a droplet deposited by liquid needle deposition technique. *npj Microgravity*, 9(1):49, Jun 2023.

[14] Hansjorg Dittus, Claus Lammerzahl, and Slava G. Turyshev. *Lasers, Clocks and Drag-Free Control*. Springer Berlin, Heidelberg, 2007.

[15] M. R. Drinkwater, R. Floberghagen, R. Haagmans, D. Muzi, and A. Popescu. *GOCE: ESA's First Earth Explorer Core Mission*, pages 419–432. Springer Netherlands, Dordrecht, 2003.

[16] ESA. Living planet programme. `https://www.esa.int/kids/en/learn/Earth/ESA_s_Living_Planet_Programme`, 2000.

[17] M. van der Meijde, R. Pail, R. Bingham, and R. Floberghagen. Goce data, models, and applications: A review. *International Journal of Applied Earth Observation and Geoinformation*, 35:4–15, 2015. GOCE earth science applications and models (Based on the ESA GOCE solid earth workshop, 16-17 October 2012).

[18] Z. Zhu, Z.B. Zhou, L. Cai, Y.Z. Bai, and J. Luo. Electrostatic gravity gradiometer design for the future mission. *Advances in Space Research*, 51(12):2269–2276, 2013.

[19] Reiner Rummel. *GOCE: Gravitational Gradiometry in a Satellite*, pages 93–103. Springer Berlin Heidelberg, Berlin, Heidelberg, 2010.

[20] Zhang Yong-zhi, Xu Hai-jun, Wang Wei-Dong, Duan Hu-rong, and Zhang Ben-ping. Gravity anomaly from satellite gravity gradiometry data by goce in japan ms9.0 strong earthquake region. *Procedia Environmental Sciences*, 10:529–534, 2011. 2011 3rd International Conference on Environmental Science and Information Application Technology ESIAT 2011.

[21] Byron Tapley, Srinivas Bettadpur, Michael Watkins, and Christoph Reigber. The gravity recovery and climate experiment: Mission overview and early results. *Geophysical Research Letters*, 31:4, 05 2004.

[22] Richard P. Kornfeld, Bradford W. Arnold, Michael A. Gross, Neil T. Dahya, William M. Klipstein, Peter F. Gath, and Srinivas Bettadpur. Grace-fo: The gravity recovery and climate experiment follow-on mission. *Journal of Spacecraft and Rockets*, 56(3):931–951, 2019.

[23] Klaus Abich et al. Grace-follow on laser ranging interferometer: German contribution. *Journal of Physics: Conference Series*, 610(1):012010, apr 2015.

[24] Daniel Schütze, Gunnar Stede, Vitali Müller, Oliver Gerberding, Tamara Bandikova, Benjamin S. Sheard, Gerhard Heinzel, and Karsten Danzmann. Laser beam steering for grace follow-on intersatellite interferometry. *Opt. Express*, 22(20):24117–24132, Oct 2014.

[25] Klaus Abich et al. In-orbit performance of the grace follow-on laser ranging interferometer. *Phys. Rev. Lett.*, 123:031101, Jul 2019.

[26] Justyna Sliwinska, Malgorzata Winska, and Jolanta Nastula. Validation of GRACE and GRACE-FO mascon data for the study of polar motion excitation. *Remote. Sens.*, 13(6):1152, 2021.

[27] Frédéric Frappart and Guillaume Ramillien. Monitoring groundwater storage changes using the gravity recovery and climate experiment (grace) satellite mission: A review. *Remote Sensing*, 10(6), 2018.

[28] Taehwan Jeon, Ki-Weon Seo, Kookhyoun Youm, Jianli Chen, and Clark R. Wilson. Global sea level change signatures observed by grace satellite gravimetry. *Scientific Reports*, 8(1):13519, Sep 2018.

[29] Byron D. Tapley, Michael M. Watkins, Frank Flechtner, Christoph Reigber, Srinivas Bettadpur, Matthew Rodell, Ingo Sasgen, James S. Famiglietti,

Felix W. Landerer, Don P. Chambers, John T. Reager, Alex S. Gardner, Himanshu Save, Erik R. Ivins, Sean C. Swenson, Carmen Boening, Christoph Dahle, David N. Wiese, Henryk Dobslaw, Mark E. Tamisiea, and Isabella Velicogna. Contributions of GRACE to understanding climate change. *Nature Climate Change*, 9(5):358–369, April 2019.

[30] C Zanoni, D Bortoluzzi, J W Conklin, I Köker, B Seutchat, and S Vitale. Summary of the results of the lisa-pathfinder test mass release. *Journal of Physics: Conference Series*, 610(1):012022, apr 2015.

[31] M. Armano et al. Sub-femto-g free fall for space-based gravitational wave observatories: Lisa pathfinder results. *Phys. Rev. Lett.*, 116:231101, Jun 2016.

[32] S. Anza et al. The ltp experiment on the lisa pathfinder mission. *Classical and Quantum Gravity*, 22(10):S125, apr 2005.

[33] M. Armano *et al.* Sensor noise in lisa pathfinder: In-flight performance of the optical test mass readout. *Phys. Rev. Lett.*, 126:131103, Apr 2021.

[34] M. Armano et al. Lisa pathfinder performance confirmed in an open-loop configuration: Results from the free-fall actuation mode. *Phys. Rev. Lett.*, 123:111101, Sep 2019.

[35] M. Armano et al. Precision charge control for isolated free-falling test masses: Lisa pathfinder results. *Phys. Rev. D*, 98:062001, Sep 2018.

[36] M. Armano *et al.* Beyond the required lisa free-fall performance: New lisa pathfinder results down to 20 μHz. *Physical Review Letters*, 120(6).

[37] Yungui Gong, Jun Luo, and Bin Wang. Concepts and status of chinese space gravitational wave detection projects. *Nature Astronomy*, 5(9):881–889, Sep 2021.

[38] Jun Luo et al. Tianqin: a space-borne gravitational wave detector. *Classical and Quantum Gravity*, 33(3):035010, jan 2016.

[39] Wen-Hong Ruan, Zong-Kuan Guo, Rong-Gen Cai, and Yuan-Zhong Zhang. Taiji program: Gravitational-wave sources. *International Journal of Modern Physics A*, 35(17):2050075, 2020.

[40] Seiji Kawamura et al. The japanese space gravitational wave antenna—decigo. *Classical and Quantum Gravity*, 23(8):S125, mar 2006.

[41] D B DeBra and J W Conklin. Measurement of drag and its cancellation. *Classical and Quantum Gravity*, 28(9):094015, apr 2011.

[42] M. Armano et al. Capacitive sensing of test mass motion with nanometer precision over millimeter-wide sensing gaps for space-borne gravitational reference sensors. *Phys. Rev. D*, 96:062004, Sep 2017.

[43] H. Inchauspé, T. Olatunde, S. Apple, S. Parry, B. Letson, N. Turetta, G. Mueller, P. J. Wass, and J. W. Conklin. Numerical modeling and experimental demonstration of pulsed charge control for the space inertial sensor used in lisa. *Phys. Rev. D*, 102:042002, Aug 2020.

[44] The eLISA Consortium et al. The gravitational universe, 2013.

[45] J. I. Thorpe et al. Micrometeoroid events in lisa pathfinder. *The Astrophysical Journal*, 883(1):53, sep 2019.

[46] Rita Dolesi et al. Gravitational sensor for lisa and its technology demonstration mission. *Classical and Quantum Gravity*, 20(10):S99, apr 2003.

[47] T A Wagner, S Schlamminger, J H Gundlach, and E G Adelberger. Torsion-balance tests of the weak equivalence principle. *Classical and Quantum Gravity*, 29(18):184002, aug 2012.

[48] Andrew Chilton, Ryan Shelley, Taiwo Olatunde, Giacomo Ciani, John W Conklin, and Guido Mueller. The uf torsion pendulum, a lisa technology testbed: Sensing system and initial results. *Journal of Physics: Conference Series*, 610(1):012038, apr 2015.

[49] H B Tu, Y Z Bai, Z B Zhou, and J Luo. Electrostatic-control performance measurement of the inertial sensor with a torsion pendulum. *Journal of Physics: Conference Series*, 154(1):012036, mar 2009.

[50] H B Tu, Y Z Bai, Z B Zhou, L Liu, L Cai, and J Luo. Performance measurements of an inertial sensor with a two-stage controlled torsion pendulum. *Classical and Quantum Gravity*, 27(20):205016, sep 2010.

[51] S. E. Pollack, S. Schlamminger, and J. H. Gundlach. Outgassing, Temperature Gradients and the Radiometer Effect in LISA: A Torsion Pendulum Investigation. *AIP Conference Proceedings*, 873(1):158–164, 11 2006.

[52] A Cavalleri, G Ciani, R Dolesi, A Heptonstall, M Hueller, D Nicolodi, S Rowan, D Tombolato, S Vitale, P J Wass, and W J Weber. A new torsion pendulum for testing the limits of free-fall for lisa test masses. *Classical and Quantum Gravity*, 26(9):094017, apr 2009.

[53] A Cavalleri, G Ciani, R Dolesi, M Hueller, D Nicolodi, D Tombolato, P J Wass, W J Weber, S Vitale, and L Carbone. Direct force measurements for testing the lisa pathfinder gravitational reference sensor. *Classical and Quantum Gravity*, 26(9):094012, apr 2009.

[54] Massimo Bassan, Antonella Cavalleri, Martina De Laurentis, Fabrizio De Marchi, Rosario De Rosa, Luciano Di Fiore, Rita Dolesi, Noemi Finetti, Fabio Garufi, Aniello Grado, Mauro Hueller, Leopoldo Milano, Giuseppe Pucacco, Ruggero Stanga, Daniele Vetrugno, Massimo Visco, Stefano Vitale, and William J. Weber. A two-stage torsion pendulum for ground testing free fall conditions on two degrees of freedom. *Nuclear and Particle Physics Proceedings*, 291-293:134–139, 2017. “New eyes on the Universe” CRIS 2016 Cosmic Rays International Seminars Proceedings of the Cosmic Rays International Seminars.

[55] Giacomo Ciani, Andrew Chilton, Stephen Apple, Taiwo Olatunde, Michael Aitken, Guido Mueller, and John W. Conklin. A new torsion pendulum for gravitational reference sensor technology development. *Review of Scientific Instruments*, 88(6):064502, 06 2017.

[56] Giacomo Ciani. *Free-fall of LISA Test Masses: a new torsion pendulum to test translational acceleration*. PhD thesis, University of Trento, 2008.

[57] LISA Pathfinder collaboration. Lisa pathfinder: First steps to observing gravitational waves from space. *Journal of Physics: Conference Series*, 840(1):012001, may 2017.

[58] Pau Amaro-Seoane et al. Laser Interferometer Space Antenna. *arXiv.org*, February 2017.

[59] D. N. A. SHAUL, H. M. ARAÚJO, G. K. ROCHESTER, M. SCHULTE, T. J. SUMNER, C. TRENKEL, and P. WASS. Charge management for lisa and lisa pathfinder. *International Journal of Modern Physics D*, 17(07):993–1003, 2008.

[60] O Jennrich. Lisa technology and instrumentation. *Classical and Quantum Gravity*, 26(15):153001, jul 2009.

[61] F Acernese, E Calloni, R De Rosa, L Di Fiore, L Garcia, and L Milano. An optical readout system for the LISA gravitational reference sensors. *Classical and Quantum Gravity*, 21(5):S621–S627, feb 2004.

[62] A Cavalleri, G Ciani, R De Rosa, L Di Fiore, R Dolesi, F Garufi, M Hueller, D Nicolodi, A La Rana, L Milano, D Tombolato, S Vitale, P J Wass, and W J Weber. Ground testing, with a four mass torsion pendulum facility, of an optical-read-out for the LISA gravitational reference sensor. *Journal of Physics: Conference Series*, 154:012012, mar 2009.

[63] Fausto Acernese, Rosario De Rosa, Luciano Di Fiore, Fabio Garufi, Adele La Rana, and Leopoldo Milano. Some progress in the development of an optical readout system for the lisa gravitational reference sensor. *AIP Conference Proceedings*, 873(1):339–343, 2006.

[64] A Grado, R De Rosa, L Di Fiore, F Garufi, L Milano, G Russano, and V Spagnuolo. An optical read-out system for the lisa gravitational reference sensor: present status and perspectives. *Journal of Physics: Conference Series*, 840(1):012047, 2017.

[65] Gerhard Meyer and Nabil M. Amer. Novel optical approach to atomic force microscopy. *Applied Physics Letters*, 53(12):1045–1047, 1988.

[66] J. M. Hogan, J. Hammer, S.-W. Chiow, S. Dickerson, D. M. S. Johnson, T. Kovachy, A. Sugarbaker, and M. A. Kasevich. Precision angle sensor using an optical lever inside a sagnac interferometer. *Opt. Lett.*, 36(9):1698–1700, 2011.

[67] Yohannes Panduputra, Tuck Wah Ng, Adrian Neild, and William Yeong Liang Ling. Adhesion force studies using a dangling optical lever with variable sensitivity. *Opt. Lett.*, 36(2):175–177, Jan 2011.

[68] V Huarcaya, G Apelbaum, V Haendchen, Q Wang, G Heinzel, and M Mehmet. Five degrees of freedom test mass readout via optical levers. *Classical and Quantum Gravity*, 37(2):025004, dec 2019.

[69] Newport. HXP100 – MECA. `https://www.newport.com/p/HXP100-MECA`, 2015.

[70] M. Bassan, A. Cavalleri, M. De Laurentis, F. De Marchi, R. De Rosa, L. Di Fiore, R. Dolesi, N. Finetti, F. Garufi, A. Grado, M. Hueller, L. Mar-

coni, L. Milano, G. Pucacco, R. Stanga, M. Visco, S. Vitale, and W. J. Weber. Approaching free fall on two degrees of freedom: Simultaneous measurement of residual force and torque on a double torsion pendulum. *Phys. Rev. Lett.*, 116:051104, Feb 2016.

[71] Trioptics. TA 100 – 38. `https://trioptics.com/products/triangle-electronic-autocollimators/`.

[72] Michael Tröbs and Gerhard Heinzel. Improved spectrum estimation from digitized time series on a logarithmic frequency axis. *Measurement*, 39(2):120–129, February 2006.

[73] Michael Troebs and Gerhard Heinzel. Improved spectrum estimation from digitized time series on a logarithmic frequency axis (vol 39, pg 120, 2006). *Measurement*, 42(1):170–170, 2009.

[74] B.P. Abbot *et al.* (LIGO Scientific Collaboration and Virgo Collaboration). GW170817: Observation of gravitational waves from a binary neutron star inspiral. *Physical Review Letters*, 119(16), October 2017.

[75] M. Coleman Miller and Nicolás Yunes. The new frontier of gravitational waves. *Nature*, 568(7753):469–476, April 2019.

[76] Holger Müller, Sven Herrmann, Claus Braxmaier, Stephan Schiller, and Achim Peters. Modern michelson-morley experiment using cryogenic optical resonators. *Physical Review Letters*, 91(2), July 2003.

[77] Massimo Tinto, Daniel A. Shaddock, Julien Sylvestre, and J. W. Armstrong. Implementation of time-delay interferometry for LISA. *Physical Review D*, 67(12), June 2003.

[78] LISA Frequency control study team. LISA Frequency Control White Paper. *LISA-JPL-TN-823*, 2000.

[79] M. P. Ross, K. Venkateswara, C. A. Hagedorn, C. J. Leupold, P. W. F. Forsyth, J. D. Wegner, E. A. Shaw, J. G. Lee, and J. H. Gundlach. A low-frequency torsion pendulum with interferometric readout. *Review of Scientific Instruments*, 92(5):054502, 05 2021.

[80] A Staley and *et al.* Achieving resonance in the advanced ligo gravitational-wave interferometer. *Classical and Quantum Gravity*, 31(24):245010, nov 2014.

[81] E. A. Shaw, M. P. Ross, C. A. Hagedorn, E. G. Adelberger, and J. H. Gundlach. Torsion-balance search for ultralow-mass bosonic dark matter. *Phys. Rev. D*, 105:042007, Feb 2022.

[82] Gerhard Heinzel, Felipe Guzmán Cervantes, Antonio F. García Marín, Joachim Kullmann, Wang Feng, and Karsten Danzmann. Deep phase modulation interferometry. *Opt. Express*, 18(18):19076–19086, Aug 2010.

[83] Daniel A. Shaddock. Digitally enhanced heterodyne interferometry. *Opt. Lett.*, 32(22):3355–3357, Nov 2007.

[84] Glenn de Vine, David S. Rabeling, Bram J. J. Slagmolen, Timothy T-Y. Lam, Sheon Chua, Danielle M. Wuchenich, David E. McClelland, and Daniel A. Shaddock. Picometer level displacement metrology with digitally enhanced heterodyne interferometry. *Opt. Express*, 17(2):828–837, Jan 2009.

[85] Oliver Gerberding. Deep frequency modulation interferometry. *Optics Express*, 23(11):14753, May 2015.

[86] Katharina-Sophie Isleif, Oliver Gerberding, Thomas S. Schwarze, Moritz Mehmet, Gerhard Heinzel, and Felipe Guzmán Cervantes. Experimental demonstration of deep frequency modulation interferometry. *Opt. Express*, 24:1676–1684, Jan 2016.

[87] Katharina-Sophie Isleif, Gerhard Heinzel, Moritz Mehmet, and Oliver Gerberding. Compact multifringe interferometry with subpicometer precision. *Physical Review Applied*, 12(3), September 2019.

[88] Katharina-Sophie Isleif. *Laser interferometry for LISA and satellite geodesy missions*. Hannover : Institutional Repository of Leibniz Universität Hannover, 2018.

[89] Oliver Gerberding, Katharina-Sophie Isleif, Moritz Mehmet, Karsten Danzmann, and Gerhard Heinzel. Laser-frequency stabilization via a quasimonolithic mach-zehnder interferometer with arms of unequal length and balanced dc readout. *Phys. Rev. Appl.*, 7:024027, Feb 2017.

[90] IfoCAD. http://www.lisa.aei-hannover.de/ifocad/.

[91] M Chwalla, K Danzmann, G Fernández Barranco, E Fitzsimons, O Gerberding, G Heinzel, C J Killow, M Lieser, M Perreur-Lloyd, D I Robertson, S Schuster, T S Schwarze, M Tröbs, H Ward, and M Zwetz. Design and

construction of an optical test bed for lisa imaging systems and tilt-to-length coupling. *Classical and Quantum Gravity*, 33(24):245015, nov 2016.

[92] Christian J. Killow, Ewan D. Fitzsimons, Michael Perreur-Lloyd, David I. Robertson, Henry Ward, and Johanna Bogenstahl. Optical fiber couplers for precision spaceborne metrology. *Appl. Opt.*, 55(10):2724–2731, Apr 2016.

[93] Katharina-Sophie Isleif, Lea Bischof, Stefan Ast, Daniel Penkert, Thomas S Schwarze, Germán Fernández Barranco, Max Zwetz, Sonja Veith, Jan-Simon Hennig, Michael Tröbs, Jens Reiche, Oliver Gerberding, Karsten Danzmann, and Gerhard Heinzel. Towards the lisa backlink: experiment design for comparing optical phase reference distribution systems. *Classical and Quantum Gravity*, 35(8):085009, mar 2018.

[94] Nicole Knust. The optical benches of the three-backlink experiment: Construction, commissioning and characterization. Master's thesis, Leibniz Universität Hannover, 2020.

[95] Karl Hoffmann. Applying the wheatstone bridge circuit. *HBM*, 1974.

[96] Newport. Vortex plus tlb 6821. `https://www.newport.com/f/vortex-plus-finely-tunable-lasers`, 2015.

[97] Coherent. Npro prometheus. `https://www.coherent.com/lasers/cw-solid-state/mephisto`, 2012.

[98] Volker Leonhardt and Jordan B. Camp. Space interferometry application of laser frequency stabilization with molecular iodine. *Appl. Opt.*, 45(17):4142–4146, Jun 2006.

[99] Thomas Kissinger, Thomas O.H. Charrett, and Ralph P. Tatam. Range-resolved interferometric signal processing using sinusoidal optical frequency modulation. *Opt. Express*, 23(7):9415–9431, Apr 2015.

[100] Andrew J. Sutton, Oliver Gerberding, Gerhard Heinzel, and Daniel A. Shaddock. Digitally enhanced homodyne interferometry. *Opt. Express*, 20(20):22195–22207, Sep 2012.

[101] M. Armano *et al.* Sensor noise in lisa pathfinder: An extensive in-flight review of the angular and longitudinal interferometric measurement system. *Phys. Rev. D*, 106:082001, Oct 2022.

[102] Liquid Instruments. Liquid instruments. `https://www.liquidinstruments.com`.

[103] Miguel Dovale Álvarez. *Optical Cavities for Optical Atomic Clocks, Atom Interferometry and Gravitational-Wave Detection*. Springer International Publishing, 2019.

[104] Josep Sanjuan, Norman Gürlebeck, and Claus Braxmaier. Mathematical model of thermal shields for long-term stability optical resonators. *Optics Express*, 23(14):17892, July 2015.

[105] Maike Lieser. *LISA optical bench development : Experimental investigation of tilt-to-length coupling for a spaceborne gravitational wave detector*. PhD thesis, Leibniz Universität Hannover, 2017.

[106] J.E. Gray and D.W. Allan. A method for estimating the frequency stability of an individual oscillator. In *28th Annual Symposium on Frequency Control*. IEEE, 1974.

[107] W Riley and D Howe. Handbook of Frequency Stability Analysis. *Special Publication (NIST SP) - 1065*, 2008.

[108] Enrico Rubiola. *Phase Noise and Frequency Stability in Oscillators*. Cambridge University Press, November 2008.

[109] Yichao Yang, Kohei Yamamoto, Victor Huarcaya, Christoph Vorndamme, Daniel Penkert, Germán Fernández Barranco, Thomas S. Schwarze, Moritz Mehmet, Juan Jose Esteban Delgado, Jianjun Jia, Gerhard Heinzel, and Miguel Dovale Álvarez. Single-element dual-interferometer for precision inertial sensing. *Sensors*, 20(17):4986, September 2020.

[110] Victor Huarcaya, Miguel Dovale Álvarez, Daniel Penkert, Stefano Gozzo, Pablo Martínez Cano, Kohei Yamamoto, Juan José Esteban Delgado, Moritz Mehmet, Karsten Danzmann, and Gerhard Heinzel. 2×10^{-13} fractional laser-frequency stability with a 7-cm unequal-arm mach-zehnder interferometer. *Phys. Rev. Appl.*, 20:024078, Aug 2023.

[111] Hao Yan, Hsien-Chi Yeh, and Qiuli Mao. High precision six-degree-of-freedom interferometer for test mass readout. *Classical and Quantum Gravity*, 39(7):075024, mar 2022.

[112] Ziren Luo, ZongKuan Guo, Gang Jin, Yueliang Wu, and Wenrui Hu. A brief analysis to taiji: Science and technology. *Results in Physics*, 16:102918, March 2020.

Appendices

A.1 Tcl hexapod code: rotation motion

```
#Rotation Step Range [-0.1, 0.1]

set TimeOut 10
set code 0

OpenConnection $TimeOut socketID
if {$socketID == -1} {
  puts stdout "OpenConnection failed => $socketID"
  return
}

# Main

set T0 5000; #Time delay
set Range 0.2; #From Min to Max (degree)
set loop 3; #How many times do you want to repeat?
set pi [expr 2*asin(1.0)]; #Pi
set period 20; #perion is 20 second
set delta 0.2; #Time interval
set amplitude 0.1; #Amplitude(degree)
set step [expr $period/$delta];

HexapodMoveAbsolute $socketID HEXAPOD Work 0 0 -11 0 0 $amplitude; # Position(
   mm,degree)
after $T0

for {set i0 0} {$i0<3} {incr i0} {
    for {set i 0} {$i<$step} {incr i} {
      set displacement [expr $amplitude*cos(2*$pi*($i*$delta+$delta)/$period)-
         $amplitude*cos(2*$pi*$i*$delta/$period)]
      set velocity [expr $amplitude*abs($displacement/$delta)]
      HexapodMoveIncrementalControlWithTargetVelocity $socketID HEXAPOD Work
         Rotation 0 0 $displacement $velocity
  }
}

# Close TCP socket
TCP_CloseSocket $socketID
```

B.2 Tcl hexapod code: random displacement

```
# Display error and close procedure
proc DisplayErrorAndClose {socketID code APIName} {
  global tcl_argv
  if {$code != -2 && $code != -108} {
    set code2 [catch "ErrorStringGet $socketID $code strError"]
    if {$code2 != 0} {
      puts stdout "$APIName ERROR => $code - ErrorStringGet ERROR => $code2"
      set tcl_argv(0) "$APIName ERROR => $code"
    } else {
      puts stdout "$APIName $strError"
      set tcl_argv(0) "$APIName $strError"
    }
  } else {
    if {$code == -2} {
      puts stdout "$APIName ERROR => $code : TCP timeout"
      set tcl_argv(0) "$APIName ERROR => $code : TCP timeout"
    }
    if {$code == -108} {
      puts stdout "$APIName ERROR => $code : The TCP/IP connection was closed
         by an administrator"
      set tcl_argv(0) "$APIName ERROR => $code :  The TCP/IP connection was
         closed by an administrator"
    }
  }
  set code2 [catch "TCP_CloseSocket $socketID"]
  return
}

# Main process
set TimeOut 20
set code 0

# Open TCP socket
OpenConnection $TimeOut socketID
if {$socketID == -1} {
  puts stdout "OpenConnection failed => $socketID"
  return
}

set code [catch "HexapodMoveAbsolute $socketID HEXAPOD Work -0.13 -0.54 -11 0
   0 0.08"]
if {$code != 0} {
    DisplayErrorAndClose $socketID $code "HexapodMoveAbsolute"
    return
}

after 1000

set code [catch "HexapodMoveAbsolute $socketID HEXAPOD Work -0.11 0.69 -11 0 0
    -0.11"]
if {$code != 0} {
    DisplayErrorAndClose $socketID $code "HexapodMoveAbsolute"
    return
```

```
}

after 1000

set code [catch "HexapodMoveAbsolute $socketID HEXAPOD Work -0.39 -0.61 -11 0
   0 -0.15"]
if {$code != 0} {
    DisplayErrorAndClose $socketID $code "HexapodMoveAbsolute"
    return
}

after 1000

set code [catch "HexapodMoveAbsolute $socketID HEXAPOD Work 0.02 -0.55 -11 0 0
    -0.08"]
if {$code != 0} {
    DisplayErrorAndClose $socketID $code "HexapodMoveAbsolute"
    return
}

after 1000

set code [catch "HexapodMoveAbsolute $socketID HEXAPOD Work 0.02 -0.66 -11 0 0
    -0.07"]
if {$code != 0} {
    DisplayErrorAndClose $socketID $code "HexapodMoveAbsolute"
    return
}

after 1000

set code [catch "HexapodMoveAbsolute $socketID HEXAPOD Work 0.64 -0.54 -11 0 0
    -0.03"]
if {$code != 0} {
    DisplayErrorAndClose $socketID $code "HexapodMoveAbsolute"
    return
}

after 1000

set code [catch "HexapodMoveAbsolute $socketID HEXAPOD Work 0.59 -0.13 -11 0 0
    0"]
if {$code != 0} {
    DisplayErrorAndClose $socketID $code "HexapodMoveAbsolute"
    return
}

# Close TCP socket
TCP_CloseSocket $socketID
```

C.3 5-DoF TM readout Matlab code

```
clear all

%% Load the files
trans_data = dlmread ('TRANSLATIONAL_matrix.txt');
save('trans_data.mat', 'trans_data');
rot_data = dlmread ('ROTATIONAL_matrix.txt');
save('rot_data.mat', 'rot_data');
Mat_x = dlmread ('x_displ.txt'); %THIS IS THE FILE YOU WANT TO ANALIZE
save('mat_x.mat', 'Mat_x');
Mat_y = dlmread ('y_displ.txt'); %THIS IS THE FILE YOU WANT TO ANALIZE
save('mat_y.mat', 'Mat_y');
Mat_rot = dlmread ('rot_displ.txt'); %THIS IS THE FILE YOU WANT TO ANALIZE
save('mat_rot.mat', 'Mat_rot');

%% Translational Displacement
displ = trans_data(:,7);
%x Displacement
QPD1 = trans_data(:,2);
QPD3 = -trans_data(:,4);
%y Displacement
QPD2 = trans_data(:,3);
QPD4 = -trans_data(:,5);

%% Statistical Analysis Translational Displacement
format long

X = [ones(length(displ),1) displ];
b1 = X\QPD1;
b2 = X\QPD2;
b3 = X\QPD3;
b4 = X\QPD4;

V1 = X*b1;
V2 = X*b2;
V3 = X*b3;
V4 = X*b4;

%% Rotational Displacement
rot_displ = rot_data(:,7);
rot_QPD1 = rot_data(:,2);
rot_QPD2 = rot_data(:,3);
rot_QPD3 = rot_data(:,4);
rot_QPD4 = rot_data(:,5);

%% Statistical Analysis Rotational Displacement
format long

Y = [ones(length(rot_displ),1) rot_displ];
c1 = Y\rot_QPD1;
c2 = Y\rot_QPD2;
c3 = Y\rot_QPD3;
c4 = Y\rot_QPD4;
```

```
VR1 = Y*c1;
VR2 = Y*c2;
VR3 = Y*c3;
VR4 = Y*c4;

%% Matrix Analysis

syms d beta
d = 225000; %distance in mm or m or um
beta = 45*(pi/180); %To change the angle, just change the first factor.
k = 1E3; %Remember to divide 1000 if you use mrad

%Analytical A and B
Aa = 2*sin(beta);
Bb = 2*d;

%% Calibration Factors (Using the micrometer & non-normalized)

k1 = 943.4;
k2 = 878.1;
k3 = 874.4;
k4 = 858.2;
K_micro = 1E6; %divide by 1E6 if you are using micrometer

%% Analytical and measured Matrix Defined

Ma = [0, 0, 0, k1*d/(k*K_micro), 0;...
    k1/K_micro, 0, k1*sqrt(2)*d/(k*K_micro), 0, 0;...
    0, 0, 0, 0, k2*d/(k*K_micro);...
    0, k2/K_micro, k2*sqrt(2)*d/(k*K_micro), 0, 0;...
    0, 0, 0, -k3*d/(k*K_micro), 0;...
    -k3/K_micro, 0, k3*sqrt(2)*d/(k*K_micro), 0, 0;...
    0, 0, 0, 0, -k4*d/(k*K_micro);...
    0, -k4/K_micro, k4*sqrt(2)*d/(k*K_micro), 0, 0];

M = [b1(2) 0 c1(2);...
    0 b2(2) c2(2);...
    -b3(2) 0 c3(2);...
    0 -b4(2) c4(2)];

Ml = inv(M'*M)*M';
Mal = inv(Ma'*Ma)*Ma';
proof = Ml*M;

%% Position Loop

positionMat_x = zeros(length(Mat_x),5);
positionMat_y = zeros(length(Mat_y),5);
positionMat_rot = zeros(length(Mat_rot),5);

for i = 1:length(Mat_x)
   positionMat_x(i,:) = (Mal*Mat_x(i, [1 2 3 4 5 6 7 8])');
end
```

```
for i = 1:length(Mat_y)
   positionMat_y(i,:) = (Mal*Mat_y(i, [1 2 3 4 5 6 7 8])');
end

for i = 1:length(Mat_rot)
   positionMat_rot(i,:) = (Mal*Mat_rot(i, [1 2 3 4 5 6 7 8])');
end

%% ALL PLOTS

figure; hold all;

subplot(5, 3, 1)
plot (positionMat_x(:,1),'k', 'Color',[0, 0.4470, 0.7410], 'LineWidth', 1.5)
grid on
grid minor
axis tight
ylim([-400 400])
xlim([0 6000])
ylabel('$x_{\mathrm{pos.}}[\mu␣\mathrm{m}]$','interpreter','latex')
title('$x\,␣\mathrm{Motion}$','interpreter','latex')
%
subplot(5, 3, 2)
plot (positionMat_y(:,1),'k', 'Color',[0,0.5,0])
grid on
grid minor
axis tight
ylim([-8 11])
xlim([0 6000])
title('$y\,␣\mathrm{Motion}$','interpreter','latex')
%
subplot(5, 3, 3)
plot (positionMat_rot(:,1),'k', 'Color',[0,0.5,0])
grid on
grid minor
axis tight
ylim([-8 11])
xlim([0 800000])
title('$\mathrm{Rotational}\,␣\mathrm{Motion}$','interpreter','latex')
%
subplot(5, 3, 4)
plot (positionMat_x(:,2),'k', 'Color',[0,0.5,0])
grid on
grid minor
axis tight
ylim([-7 6])
xlim([0 6000])
ylabel('$y_{\mathrm{pos.}}[\mu␣\mathrm{m}]$','interpreter','latex')
%
subplot(5, 3, 5)
plot (positionMat_y(:,2),'k', 'Color',[0, 0.4470, 0.7410], 'LineWidth', 1.5)
grid on
grid minor
axis tight
```

```
ylim([-400 400])
xlim([0 6000])
%
subplot(5, 3, 6)
plot (positionMat_rot(:,2),'k', 'Color',[0,0.5,0])
grid on
grid minor
axis tight
ylim([-7 6])
xlim([0 800000])
%
subplot(5, 3, 7)
plot (positionMat_x(:,3),'k','Color',[0,0.5,0])
grid on
grid minor
axis tight
ax = gca;
ax.YAxis.Exponent = -2;
ylim([-3.1E-2 6E-2])
xlim([0 6000])
ylabel('$$\mathrm{}\,␣\theta[\mathrm{mrad}]$','interpreter','latex')
%
subplot(5, 3, 8)
plot (positionMat_y(:,3),'k','Color',[0,0.5,0])
grid on
grid minor
axis tight
ax = gca;
ax.YAxis.Exponent = -2;
ylim([-0.031 0.06])
xlim([0 6000])
%
subplot(5, 3, 9)
plot (positionMat_rot(:,3),'k', 'Color',[0, 0.4470, 0.7410], 'LineWidth', 1.5)
grid on
axis tight
grid minor
ylim([-1 1.2])
xlim([0 800000])
%
subplot(5, 3, 10)
plot (positionMat_x(:,4),'k','Color',[0,0.5,0])
grid on
grid minor
axis tight
ax = gca;
ax.YAxis.Exponent = -2;
ylim([-5E-2 5E-2])
xlim([0 6000])
ylabel('$$\mathrm{}\,␣\psi[\mathrm{mrad}]$','interpreter','latex')
%
subplot(5, 3, 11)
plot (positionMat_y(:,4),'k','Color',[0,0.5,0])
grid on
```

```
grid minor
axis tight
ax = gca;
ax.YAxis.Exponent = -2;
ylim([-5E-2 5E-2])
xlim([0 6000])
%
subplot(5, 3, 12)
plot (positionMat_rot(:,4),'k', 'Color',[0,0.5,0])
grid on
grid minor
axis tight
ax = gca;
ax.YAxis.Exponent = -2;
ylim([-5E-2 5E-2])
xlim([0 800000])
%
subplot(5, 3, 13)
plot (positionMat_x(:,5),'k','Color',[0,0.5,0])
grid on
grid minor
axis tight
ax = gca;
ax.YAxis.Exponent = -2;
ylim([-8E-2 3E-2])
xlim([0 6000])
ylabel('$$\mathrm{}\,␣\phi[\mathrm{mrad}]$','interpreter','latex')
xlabel ('$\mathrm{Time\,␣Series}$','interpreter','latex')
%
subplot(5, 3, 14)
plot (positionMat_y(:,5),'k','Color',[0,0.5,0])
grid on
grid minor
axis tight
ax = gca;
ax.YAxis.Exponent = -2;
ylim([-8E-2 3E-2])
xlim([0 6000])
xlabel ('$\mathrm{Time\,␣Series}$','interpreter','latex')
%
subplot(5, 3, 15)
plot (positionMat_rot(:,5),'k','Color',[0,0.5,0])
grid on
grid minor
axis tight
ax = gca;
ax.YAxis.Exponent = -2;
ylim([-8E-2 3E-2])
xlim([0 800000])
xlabel ('$\mathrm{Time\,␣Series}$','interpreter','latex')

set(findobj(gcf,'type','axes'),'FontName','Arial','FontSize',20,'FontWeight','
    normal', 'LineWidth', 1);
```

D.4 SEDI Specifications

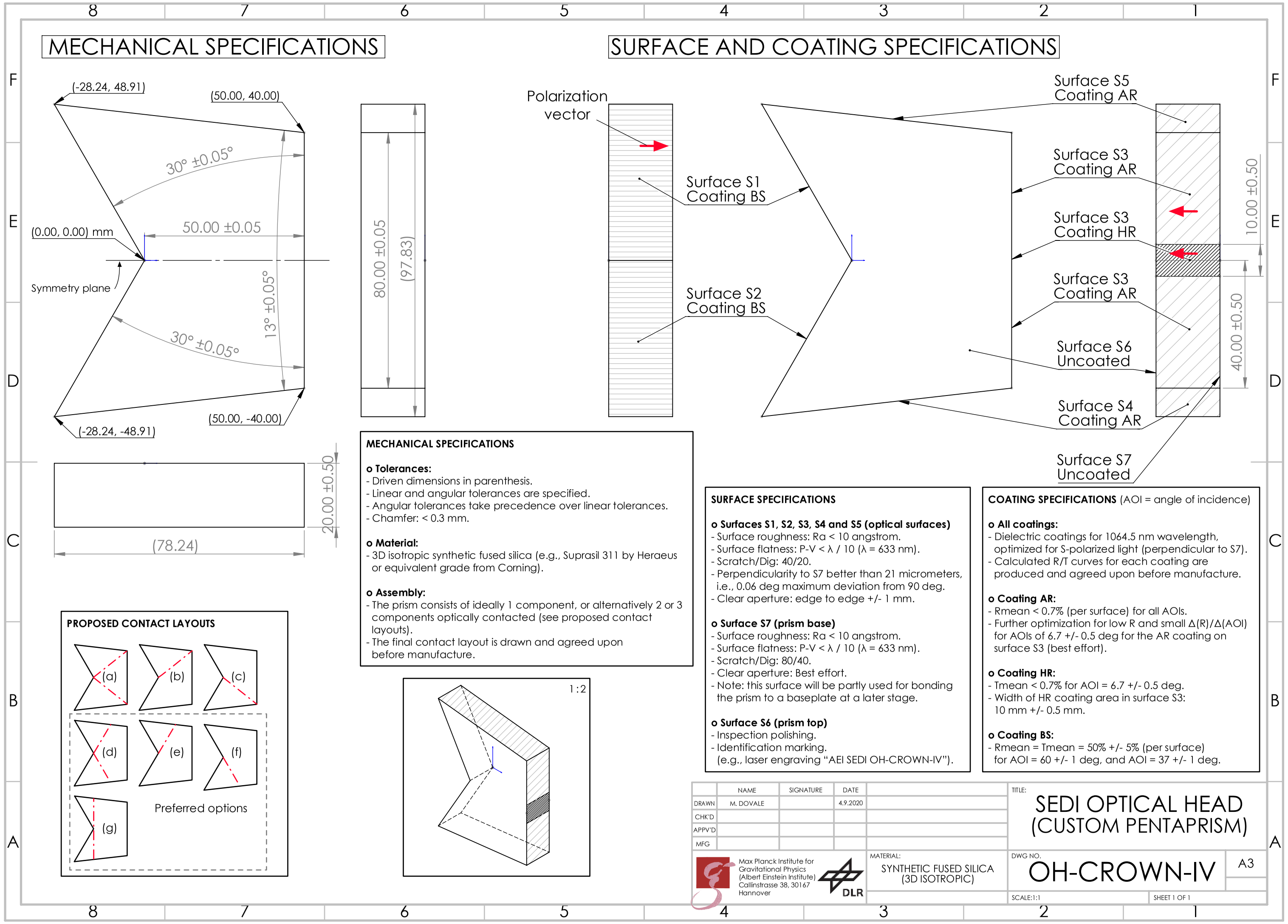

MECHANICAL SPECIFICATIONS

o Tolerances:
- Driven dimensions in parenthesis.
- Linear and angular tolerances are specified.
- Angular tolerances take precedence over linear tolerances.
- Chamfer: < 0.3 mm.

o Material:
- 3D isotropic synthetic fused silica (e.g., Suprasil 311 by Heraeus or equivalent grade from Corning).

o Assembly:
- The prism consists of ideally 1 component, or alternatively 2 or 3 components optically contacted (see proposed contact layouts).
- The final contact layout is drawn and agreed upon before manufacture.

SURFACE SPECIFICATIONS

o Surfaces S1, S2, S3, S4 and S5 (optical surfaces)
- Surface roughness: Ra < 10 angstrom.
- Surface flatness: P-V < λ / 10 (λ = 633 nm).
- Scratch/Dig: 40/20.
- Perpendicularity to S7 better than 21 micrometers, i.e., 0.06 deg maximum deviation from 90 deg.
- Clear aperture: edge to edge +/- 1 mm.

o Surface S7 (prism base)
- Surface roughness: Ra < 10 angstrom.
- Surface flatness: P-V < λ / 10 (λ = 633 nm).
- Scratch/Dig: 80/40.
- Clear aperture: Best effort.
- Note: this surface will be partly used for bonding the prism to a baseplate at a later stage.

o Surface S6 (prism top)
- Inspection polishing.
- Identification marking.
(e.g., laser engraving "AEI SEDI OH-CROWN-IV").

COATING SPECIFICATIONS (AOI = angle of incidence)

o All coatings:
- Dielectric coatings for 1064.5 nm wavelength, optimized for S-polarized light (perpendicular to S7).
- Calculated R/T curves for each coating are produced and agreed upon before manufacture.

o Coating AR:
- Rmean < 0.7% (per surface) for all AOIs.
- Further optimization for low R and small Δ(R)/Δ(AOI) for AOIs of 6.7 +/- 0.5 deg for the AR coating on surface S3 (best effort).

o Coating HR:
- Tmean < 0.7% for AOI = 6.7 +/- 0.5 deg.
- Width of HR coating area in surface S3: 10 mm +/- 0.5 mm.

o Coating BS:
- Rmean = Tmean = 50% +/- 5% (per surface) for AOI = 60 +/- 1 deg, and AOI = 37 +/- 1 deg.

	NAME	SIGNATURE	DATE
DRAWN	M. DOVALE		4.9.2020
CHK'D			
APPV'D			
MFG			

Max Planck Institute for
Gravitational Physics
(Albert Einstein Institute)
Callinstrasse 38, 30167
Hannover

DLR

MATERIAL: SYNTHETIC FUSED SILICA (3D ISOTROPIC)

TITLE: SEDI OPTICAL HEAD (CUSTOM PENTAPRISM)

DWG NO. OH-CROWN-IV

A3

SCALE:1:1

SHEET 1 OF 1

Figure 1: SEDI's optical head design. Credits: M. Dovale.

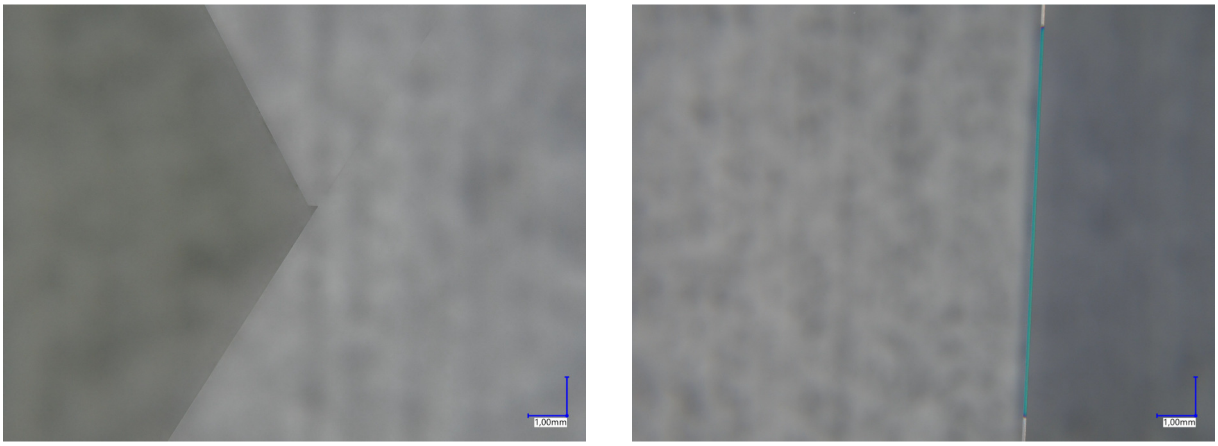

Contact Layout

HR coating

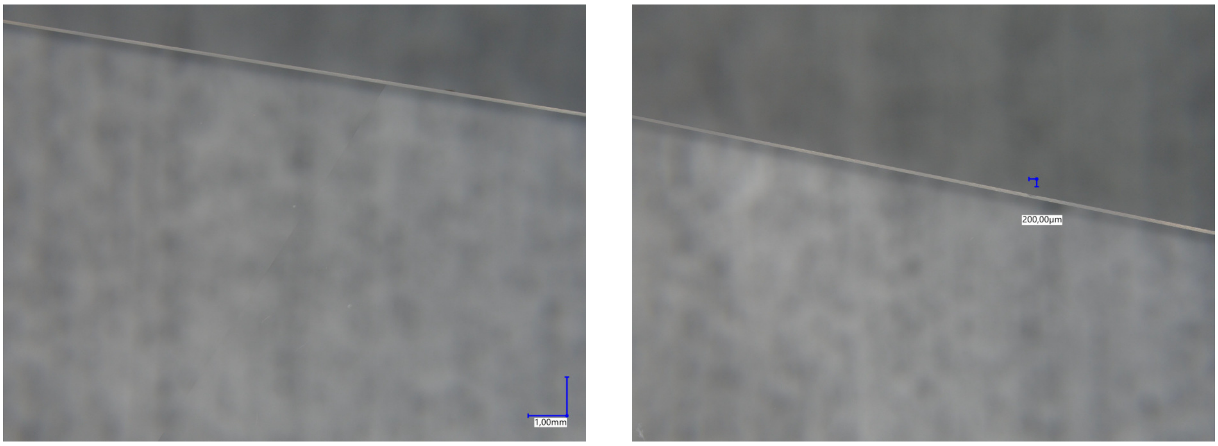

Contact Layout

Micrometer imperfection

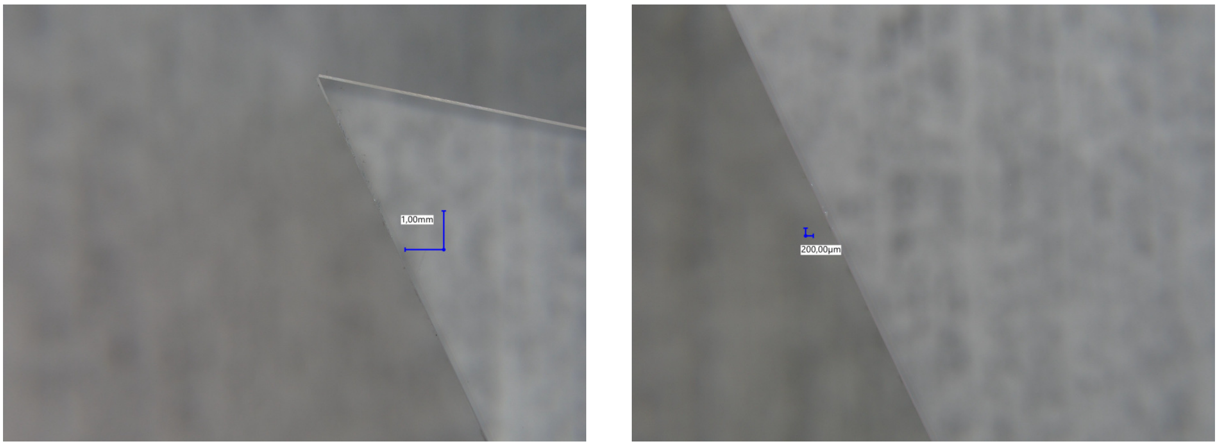

Micrometer imperfection

Micrometer imperfection

Figure 2: SEDI's pictures using the digital microscope VHX-7000. Some imperfections, the HR coating, and the contact layouts between two glass silica pieces can be seen.

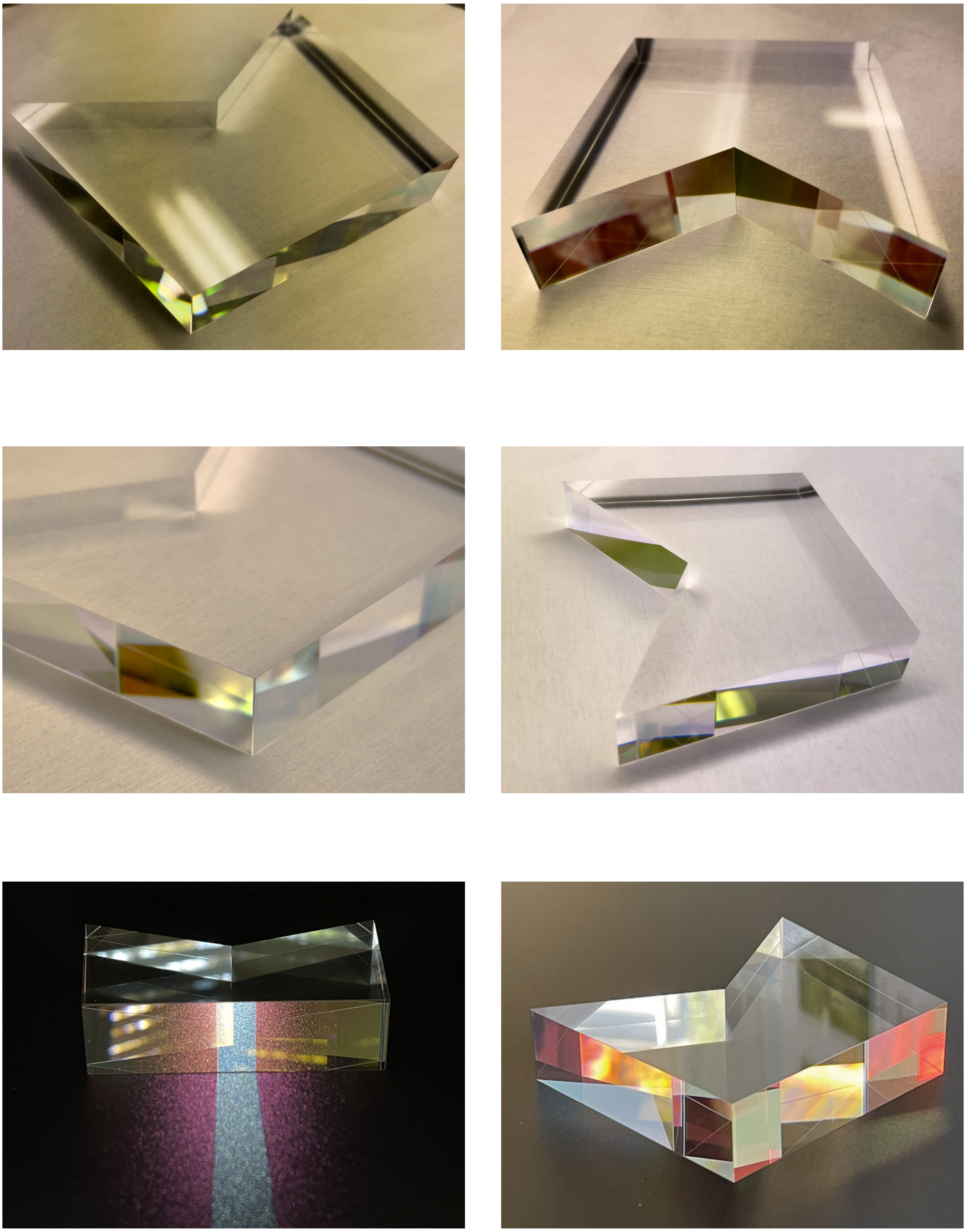

Figure 3: Different SEDI's pictures.

Publication List

1. **V. Huarcaya**, G. Apelbaum, V. Haendchen, Q. Wang, G. Heinzel, and M. Mehmet. ”Five degrees of freedom test mass readout via optical levers”. *Classical and Quantum Gravity*, 37(2):025004, December 2019.
https://doi.org/10.1088/1361-6382/ab5c73

2. Y. Yang, K. Yamamoto, **V. Huarcaya**, C. Vorndamme, D. Penkert, G. Fernandez Barranco, T.S. Schwarze, M. Mehmet, J.J. Esteban Delgado, J. Jia, G. Heinzel, and M. Dovale Alvarez. ”Single Element Dual Interferometer for precision inertial sensing”. *Sensors*, 20(17):4986, September 2020.
https://doi.org/10.3390/s20174986

3. **V. Huarcaya**, M. Dovale Alvarez, D. Penkert, S. Gozzo, P. Martinez Cano, K. Yamamoto, J.J. Esteban Delgado, M. Mehmet, K. Danzmann, and G. Heinzel. ”2×10^{-13} fractional laser-frequency stability with a 7-cm unequal-arm Mach-Zehnder interferometer”. *Physical Review Applied*, **20**, 024078, August 2023.
https://doi.org/10.1103/PhysRevApplied.20.024078

4. **V. Huarcaya**, M. Dovale Alvarez, K. Yamamoto, Y. Yang, S. Gozzo, P. Martinez Cano, M. Mehmet, J.J. Esteban Delgado, J. Jia and G. Heinzel. ”Single-Element Dual-Interferometer for Precision Inertial Sensing: Sub-Picometer Structural Stability and Performance as a Reference for Laser Frequency Stabilization”. *Sensors*, 23(24):9758, December 2023.
https://doi.org/10.3390/s23249758

...Carry me on the waves to the land I've never been,
Carry me on the waves to the lands I've never seen...
Enya, 'Orinoco Flow'